TECHNISCHE UNIVERSITÄT MÜNCHEN

TUM School of Natural Sciences

Local Control and Manipulation of Propagating Spin Waves Studied by Time-Resolved Kerr Microscopy

Christian Riedel

Vollständiger Abdruck der von der TUM School of Natural Sciences der Technischen Universität München zur Erlangung eines Doktors der Naturwissenschaften (Dr. rer. nat.) genehmigten Dissertation.

Vorsitz: Prof. Dr. Martin Zacharias

Prüfer*innen der Dissertation:

1. Prof. Dr. Christian H. Back
2. Prof. Jonathan J. Finley, Ph.D.

Die Dissertation wurde am 13.12.2022 bei der Technischen Universität München eingereicht und durch die TUM School of Natural Sciences am 15.03.2023 angenommen.

Abstract

The work embodied in this thesis investigates various spin wave phenomena, with particular interest paid to understanding the local manipulation and control of spin waves. Time-resolved magnetization dynamics, i.e. spin waves, imaged on the nanosecond time scale, will be achieved by two independent prototype Time-Resolved Magneto Optical Kerr Microscopes (TR-MOKE). The working principles of the unique TR-MOKE setups constructed during the course of this thesis will be explained and demonstrated in detail.

Spin wave propagation through a diffraction grating in a 200 nm thick magnetic insulator is presented for DE spin waves, Magneto-Static Backward Volume (BV) spin waves as well as for Forward Volume (FV) spin waves. Experimental data is supported by micromagnetic simulations. A caustic-like spin wave emission, as well as the hybridization of two Damon-Eshbach (DE) type spin wave modes within the grating region, will be presented. It will be shown that the hybridization leads to an increased attenuation and consequently to a transmission stop-band for spin waves at the grating over a certain magnetic field range.

Moreover, we will investigate the effect on the spin wave propagation behavior of various normal metals (NMs) in proximity to a magnetic insulator. The NM induced non-reciprocity of the dispersion relation of DE-like spin waves will be experimentally demonstrated. By using this effect, we will show how to use the NMs to tune the hybridization gap and in turn, to locally enhance the attenuation of the spin wave. Moreover, we will demonstrate how to use NM structures for optic-like spin wave manipulation.

I

As spin waves can be considered as potential information carriers, pulsed spin wave excitations of various shapes will be presented, i.e., a Gaussian, a chirp, and a sinc pulse. We will analyze the propagation characteristics of these pulse shapes in both, space and time. Furthermore, we will obtain the dispersion relation of DE-like spin waves by analyzing the propagation characteristics of a sinc pulse as well as a modified sinc pulse.

Kurzfassung

In der hier vorgestellten Arbeit konzentrieren wir uns auf die zeitaufgelöste Abbildung von Magnetisierungsdynamiken auf der Nanosekunden-Zeitskala, d.h. Spinwellen. Um dies zu erreichen, werden zwei unabhängige Prototypen zeitaufgelöster magneto-optischer Kerr-Mikroskope (TR-MOKE) konstruiert und ihr spezielles Arbeitsprinzip erklärt und demonstriert.

Wir werden die Spinwellenausbreitung durch ein Beugungsgitter in einem 200 nm dicken YIG-Film unter Verwendung dieser TR-MOKE-Aufbauten untersuchen und unsere Ergebnisse durch mikromagnetische Simulationen unterstützen. Eine kaustikähnliche Spinwellenemission sowie die Hybridisierung zweier Spinwellenmoden vom Damon-Eshbach-Typ innerhalb des Gitterbereichs werden vorgestellt. Es wird gezeigt, dass die Hybridisierung für einen bestimmten Magnetfeldbereich zu einer erhöhten Dämpfung und damit zu einem Transmissionsstoppband für Spinwellen am Gitter führt.

Darüber hinaus werden wir die Auswirkung verschiedener normaler Metalle (NMs) in Kontakt zu einem YIG-Film auf das Ausbreitungsverhalten von Spinwellen untersuchen. Die NM-induzierte nicht-Reziprozität der Dispersionsrelation von DE-ähnlichen Spinwellen wird experimentell demonstriert. Durch die Nutzung dieses Effekts werden wir zeigen, wie die NMs verwendet werden können, um die Hybridisierungslücke zu beeinflussen und wiederum die Dämpfung der Spinwelle lokal zu verstärken. Darüber hinaus werden wir demonstrieren, wie NM-Strukturen für eine optikähnliche Spinwellenmanipulation verwendet werden können.

Da Spinwellen als potenzielle Informationsträger betrachtet werden können, wird

eine gepulste Spinwellenanregung mit verschiedenen Pulsformen vorgestellt, d. h. einem Gauss-, einem Chirp- und einem Sinc-Puls. Wir werden die Ausbreitungscharakteristik dieser Pulsformen sowohl zeitlich als auch räumlich analysieren. Darüber hinaus werden wir die Dispersionsrelation von DE-ähnlichen Spinwellen erhalten, indem wir die Ausbreitungscharakteristik eines Sinc-Pulses sowie eines modifizierten Sinc-Pulses mit Hilfe des TR-MOKE analysieren.

Contents

List of Figures

List of Abbreviations

AWG Arbitrary Waveform Generator

BLS Brillouin Light Scattering

BV Backward Volume

CPW Coplanar Waveguide

DE Damon-Eshbach

FFT Fast Fourier Transformation

FM Ferromagnet

FMR Ferromagnetic Resonance

FV Forward Volume

GS/s Giga Samples per Second

HWP Half Waveplate

KS Kalinikos and Slavin

LL Landau-Lifshitz

LLG Landau-Lifshitz-Gilbert

ML Monolayer

MOKE Magneto Optical Kerr Effect

MPE Magnetic Proximity Effect

NA Numerical Aperture

NM Normal Metal

PEC Perfect Electrical Conductor

PID Proportional Integral Differential

PMA Perpendicular Magnetic Anisotropy

PSSW Perpendicular Standing Spin Wave

TR-STXM Time Resolved Scanning Transmission X-Ray Microscope

SNR Signal to Noise Ratio

SW Spin Wave

TR-MOKE Time Resolved - Magneto Optical Kerr Effect

WP Wollaston Prism

XMCD X-Ray Magnetic Circular Dichroism

YIG Yittrium Iron Garnet

Chapter 1

Introduction

The concept of spin waves was first introduced by Felix Bloch at the beginning of the 1930's [1,2]. Bloch described a spin wave as a low-energy excitation within a ferromagnet where one single spin had its direction reversed with respect to a large number of otherwise co-aligned atomic spins of the crystal lattice. In the decades which followed, the concept of spin waves has continued to be investigated by a large number of physicists including, for example, Holstein and Primakoff [3], Dyson [4], Herring [5], Kittel [6], as well as Griffiths [7].

In the 1990's a new concept, called magnonics, arose within the unusually rich field of spin waves [8,9]. Magnonics refers to the quasi-particle of spin waves, i.e., the magnon, and as a result it should be used to describe quantum dynamic magnetic processes only. However, similar to the research fields of photonics, electronics and phononics, this restriction is not respected as the term magnonics is used to describe a broad spectrum in the field of magnetism that is connected with spin waves. The research field of magnonics belongs to a sub-field of modern solid state physics which is concerned with the detection, as well as the manipulation of propagating spin waves through periodic magnetic media. The fundamental idea of magnonics was introduced within another research field by Léon Brillouin. Brillouin investigated the concept of a band structure of electromagnetic waves, propagating in structures with a periodic modulation of the index of refraction [10]. Such a photonic band structure can lead to stopping bands

and passing bands for electromagnetic waves, depending on the periodicity with respect to the wavelength of the electromagnetic wave. Nowadays, an entire research field is focused on the construction of artificial materials that form so-called photonic crystals in one, two, or three dimensions [11].

A similar concept was also projected for magnetostatic wave propagation in periodic structures, leading to the formation of transmission stop bands at certain spin wave excitation frequencies [12,13]. The magnetic periodicity was manufactured such that it affects global spin wave propagation, across the entire sample. Magnonic crystals in the order of micrometers have been studied to investigate the local manipulation of spin wave propagation [14–17]. Magnonics, among other research fields such as spintronics [18,19], deals with the challenging target to transport, guide and process information with the help of spin and orbital angular momentum [8, 9, 20]. A crucial difference between the concepts of photonics and magnonics is found in the dispersion relation between electromagnetic waves and spin waves, respectively. The dipole-dipole interaction of spin waves lead to an inherently anisotropic behavior of the dispersion relation. As a consequence, that might lead to complications but, on the other hand, also to the ability to externally control anisotropic effects by external magnetic fields.

In recent decades, the wave nature of spin waves has been demonstrated both theoretically and experimentally. The excitation and propagation [21–26], as well as the interference of coherently excited spin waves and diffraction phenomena have already been demonstrated [27–31]. Moreover, the reflection and refraction [32–36], as well as the effect of focusing and self-focusing spin waves [37–42] have been investigated in the framework of magnonics. As a result, a broad variety of concepts for potential magnonic devices have already been developed within this relatively young research field [8,43–51]. Magnonic crystals have been proposed as potential candidates for data processing, as they can be used to control and manipulate the propagation of spin waves [51]. However, a periodicity of the magnetic landscape in the direction of the propagating spin wave is necessary to utilize the effect of magnonic crystals.

In this thesis, we will focus on systems that enable the local control and manipula-

tion of spin wave propagation in a manner similar to magnonic crystals, but without the limitation of the periodicity being restricted to the direction of the spin wave propagation. With this, we demonstrate the possibility of further downsizing potential magnonic devices and contributing to the progression of the rich field of magnonics.

In Chapter two we will give a basic theoretical treatment of the concepts which will be used within this thesis. A mathematical description for dynamic magnetization processes, the manipulation of polarized light, as well as the concept of the Magneto Optical Kerr Effect will be explained.

In the following third Chapter, we will explain how to measure magnetization dynamic processes on the nanosecond time scale by the help of the Time-Resolved Magneto Optical Kerr Microscopes (TR-MOKE). The working principles of the TR-MOKE setups constructed during the course of this thesis will be explained and demonstrated in detail.

Moreover, in Chapter four, we will present the interaction of spin waves with a diffraction grating within in a 200 nm thick magnetic insulator. We will show a caustic-like spin wave emission from the diffraction grating, as well as the hybridization of two Damon-Eshbach (DE) type spin wave modes within the grating region. A transmission stop-band of spin waves at the grating over a certain magnetic field range will be demonstrated which arises from the hybridization of two DE-like spin wave modes.

In the subsequent Chapter five, we will investigate the effect on the spin wave propagation behavior of various normal metals (NMs) in direct contact to a magnetic insulator. We show a NM induced non-reciprocity of the dispersion relation of DE-like spin waves, how to use this effect to tune the hybridization gap, as well as how to use NM structures for optic-like spin wave manipulation.

Finally, in Chapter six, we will demonstrate the propagation characteristic of a Gaussian, a chirp, and a sinc pulse shape within a ferrimagnetic film in both, space and time. Furthermore, we will obtain the dispersion relation of DE-like spin waves by analyzing the propagation characteristic of a sinc pulse as well as a modified sinc pulse.

Chapter 2

Theoretical Background

A basic theoretical treatment of the magnetization and especially the dynamic magnetization will be presented in this chapter to understand the experimental results investigated in this thesis. Spin waves are one of the most fascinating phenomena in the rich field of magnetization dynamics. The simplest dispersion relations of spin waves have already been introduced by Felix Bloch in 1930 [1]. Spin waves can be described by the coherent phase relation between neighboring spins which results in a defined wavelength or wave-vector $\mathbf{k}$. The spin waves considered in the framework of this thesis are closely related to a phenomenon called ferromagnetic resonance (FMR) [7,52,53]. FMR describes the power absorption of electromagnetic waves by a ferromagnetic material.

The most important mathematical expressions for dynamical processes within a ferromagnet and their interpretation will be given in this chapter. We will describe the precessional motion of the magnetization at a given point in space as well as the characteristics of propagating spin waves.

2.1 Free Energy Contributions to the Landau-Lifshitz-Gilbert-Equation

The magnetic field in the case of an anisotropic ferromagnet is an effective magnetic field $\mathbf{H}_{\text{eff}}$ which can contain different magnetic field contributions [54]. Deriving the effective

magnetic field can be realized by considering the change in the free energy density U when changing the magnetization $\mathbf{M}$

$$\mathbf{H}_{\text{eff}} = -\frac{1}{\mu_0}\frac{\partial U}{\partial \mathbf{M}}, \tag{2.1}$$

with μ_0 the vacuum permeability. The contribution to the free energy density and with this to the effective magnetic field strongly depends on the experimental circumstances. We will consider three different energy contributions with regard to the experiments presented in this thesis. The Zeeman energy U_{Zeeman} contributes to the energy density if the sample is placed within an external magnetic field [54]. An external magnetic field can be defined as an external magnetic field at the position of the sample.

$$U_{\text{Zeeman}} = -\mu_0\,\mathbf{M}\cdot\mathbf{H}_{\text{ext}} \tag{2.2}$$

The Zeeman energy term results in a contribution to the effective magnetic field of

$$\mathbf{H}_{\text{Zeeman}} = -\mu_0\mathbf{H}_{\text{ext}}. \tag{2.3}$$

The tendency for the magnetization to align uniformly originates from the exchange interaction between neighboring spins. In a continuum description, this interaction leads to an exchange energy contribution U_{ex} for the free energy density U with the magnetization vector $\mathbf{M} = (M_x, M_y, M_z)$ [54]

$$U_{\text{ex}} = \frac{A}{M_{\text{s}}^2}(\nabla\cdot\mathbf{M})^2, \tag{2.4}$$

where A and M_{s} are material dependent parameters, i.e. the exchange stiffness constant and the saturation magnetization, respectively. The exchange stiffness and the saturation magnetization define a characteristic length scale l_{ex} on which the exchange interaction

between neighboring spins becomes the dominant energy term [55]

$$l_{\mathrm{ex}}^2 = \frac{2 \cdot A}{\mu_0 M_{\mathrm{s}}^2}. \tag{2.5}$$

With this, the exchange energy contribution to $\mathbf{H}_{\mathrm{eff}}$ is given by

$$\mathbf{H}_{\mathrm{ex}} = l_{\mathrm{ex}}^2 \Delta \mathbf{M}. \tag{2.6}$$

For homogeneously magnetized ellipsoids, a demagnetizing tensor $\mathbb{N}$ considers the effect of the sample geometry on the magnetization inside the sample within a mean field approach. A demagnetizing energy U_{demag} can be defined by Eq. (2.7). The name occurs from the fact that this energy leads to a reduced magnetic field within the sample compared to the external magnetic field. Considering an infinitely extended magnetic film, this contribution can be neglected as long as the magnetization is lying in the plane of the film. On the other hand, having constraints in one or more directions, with respect to the magnetization direction, may cause this contribution to become the dominant energy term. Expressions for $\mathbb{N}$ can be found in textbooks for standard geometries [56,57]. In the special case of the infinitely extended thin film, $N_x = N_y = 0$ and $N_z = 1$, with z being the direction of the surface normal.

$$U_{\mathrm{demag}} = -\mathbb{N}\,\mathbf{M} \cdot \mathbf{H}_{\mathrm{demag}} \tag{2.7}$$

The contribution to $\mathbf{H}_{\mathrm{eff}}$ from the demagnetizing energy is found to be

$$\mathbf{H}_{\mathrm{demag}} = -\frac{\mathbb{N}}{\mu_0}\mathbf{M}. \tag{2.8}$$

As a result of the individual magnetic field contributions, the magnetization $\mathbf{M}$ in Eq. (2.12) precesses around the effective magnetic field

$$\mathbf{H}_{\mathrm{eff}} = \mathbf{H}_{\mathrm{Zeeman}} \; + \; \mathbf{H}_{\mathrm{ex}} \; + \; \mathbf{H}_{\mathrm{demag}}. \tag{2.9}$$

Additional energy contributions, such as the magneto-crystalline energy, may occur but are not relevant for this thesis.

2.2 Landau-Lifshitz-Gilbert Equation

For a treatment of dynamic processes within a ferromagnetic material, we have to consider the effect of a magnetic field $\mathbf{H}$ acting on the magnetization $\mathbf{M}$. A description about how the magnetization $\mathbf{M}$ depends on a magnetic field $\mathbf{H}$ can be expressed by the equation of motion of the magnetization, first proposed by Landau and Lifshitz in 1935 [58]

$$\frac{\partial \mathbf{M}}{\partial t} = -\gamma \mu_0 \ (\mathbf{M} \times \mathbf{H}_{\text{eff}}), \tag{2.10}$$

with γ the gyromagnetic ratio, μ_0 the vacuum magnetic permeability, $\mathbf{M}$ the magnetization and $\mathbf{H}_{\text{eff}}$ the effective magnetic field. A macroscopic picture of the magnetization $\mathbf{M}$ can be achieved by using the continuum approach. It considers the sum of magnetic moments $\mathfrak{M}$ over a small, but macroscopic volume ΔV

$$\mathbf{M} = \frac{\sum_{\Delta V} \mathfrak{M}}{\Delta V}. \tag{2.11}$$

It can be seen that the length of the vector $\mathbf{M}$ and with this the absolute value of the magnetization is conserved. Considering $\mathbf{M}$ as a vector with its origin fixed, the trajectory of the other end of the vector will be on the surface of a sphere, surrounding the axis of the effective magnetic field $\mathbf{H}_{\text{eff}}$. Such a trajectory is called precession which is described by the right-hand-side of Eq. (2.10) and illustrated in Fig. 2.1 (a). Eq. (2.10) does not include any dissipative terms which take magnetic losses into account. Landau and Lifshitz originally proposed to add a second double cross-product $\mathbf{M} \times (\mathbf{M} \times \mathbf{H}_{\text{eff}})$ term to the right-hand-side of the equation of motion to account for the dissipation of energy which, however, had to be restricted to small damping. A physically correct term to the undamped Landau-Lifshitz equation was added later by Gilbert which contains a
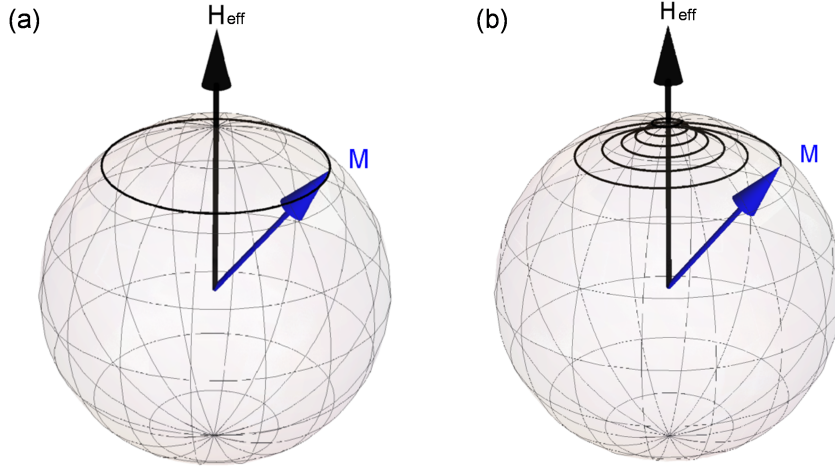
Figure 2.1: (a) Illustration of the undamped Landau-Lifshitz equation in which one end of the magnetization vector **M** keeps precessing on the surface of a sphere. (b) Illustration of the Landau-Lifshitz-Gilbert equation. The magnetization precesses on the surface of a sphere but will come to an equilibrium position, parallel to the magnetic field **H**$_{\text{eff}}$, due to energy dissipation. The length of the vector **M** is conserved.

dimensionless dissipation parameter α and leads to the famous Landau-Lifshitz-Gilbert equation (LLG)

$$\frac{\partial \mathbf{M}}{\partial t} = \underbrace{-\gamma\mu_0 \left(\mathbf{M} \times \mathbf{H}_{\text{eff}}\right)}_{\text{precession}} + \underbrace{\frac{\alpha}{M_{\text{s}}}\left(\mathbf{M} \times \frac{\partial \mathbf{M}}{\partial t}\right)}_{\text{damping}} \qquad (2.12)$$

The first term on the right-hand-side of Eq. (2.12) still describes the precessional motion of the vector **M** with respect to the effective magnetic field **H**$_{\text{eff}}$. A damping term with a dissipation or damping parameter α is presented by the second term on the right-hand-side of the LLG. This second term causes a damped precession of the magnetization **M**, forcing the magnetization to an equilibrium position, parallel to the effective magnetic field, illustrated in Fig. 2.1 (b). The equilibrium direction of the magnetization **M** can

be found by setting the left-hand-side of Eq. 2.10 equal to zero which leads to

$$\mathbf{M} \times \mathbf{H}_{\text{eff}} = 0. \tag{2.13}$$

2.3   Spin Waves

So far, we described the precessional motion of magnetization only in the time regime, but not as a function of space. The lowest energy state of a ferromagnet is achieved by considering neighboring spins, i.e., magnetic moments, to be aligned parallel. A spin wave is a low-energy excitation of a chain of spins that accounts for a precessional motion of every individual spin around the effective magnetic field. Considering the precessing spins to be parallel with respect to the neighboring spins leads to a spin wave with an infinitely long wavelength, i.e., a wave-vector $\mathbf{k}$ equal to zero. This lowest energy spin wave mode is called the FMR mode. Considering a constant phase difference between neighboring spins leads to a finite wavelength and in turn to a non zero wave-vector $\mathbf{k}$ [59]. Such an elementary excitation of a spin system, exhibiting a wave nature, is named a spin wave with its quantum particle called the magnon. Spin waves can be classified by their corresponding dispersion relation.

2.3.1   In-Plane Dispersion Relation

The dispersion relation in the thin film approximation [60] of dipolar exchange spin waves arises from solving the damped, linearized LLG equation, whereas the real part for a tangentially magnetized film is given by [61]

$$\omega^2 = \left(\omega_{\text{H}} + \omega_{\text{M}} l_{\text{ex}}^2 k_n^2 + \omega_{\text{M}} \zeta \sin^2(\phi)\right) \left(\omega_{\text{H}} + \omega_{\text{M}} l_{\text{ex}}^2 k_n^2 + \omega_{\text{M}}(1 - \zeta) - \omega_{\text{ani}}\right), \tag{2.14}$$

with ϕ the angle between the in-plane bias magnetic field and the direction of the wave-vector $\mathbf{k}$. The frequency components are given by

$$\omega_{\mathrm{H}} = \gamma\mu_0 H, \tag{2.15}$$

$$\omega_{\mathrm{M}} = \gamma\mu_0 M_{\mathrm{s}}, \tag{2.16}$$

$$\omega_{\mathrm{ani}} = \gamma\mu_0 H_{\mathrm{ani}}, \tag{2.17}$$

where H_{ani} accounts for an uniaxial anistropy term. ζ arises from the dynamic components of the demagnetizing tensor $\mathbb{N}$ and is given by

$$\zeta = 1 - \frac{1 - \exp(-|kL|)}{|kL|}. \tag{2.18}$$

Here, L accounts for the thickness of the magnetic film. The dispersion relation for a tangentially magnetized film (Eq. (2.14)) exhibits an anisotropic behavior. This anisotropic behavior can lead to Damon-Eshbach spin wave modes (DE, $\mathbf{k} \perp \mathbf{M}$, $\phi = \pm \pi/2$) and Magneto-Static Backward Volume modes (BV, $\mathbf{k}||\mathbf{M}$, $\phi = 0, \pi$) or a mixture of this two modes if the in-plane magnetization has an arbitrary angle between the DE and BV mode. Figure 2.2 presents various iso-frequency lines of the dispersion relation as a function of the angle ϕ. The anisotropic behavior can be seen by the change in $\mathbf{k}$ with respect to the angle ϕ. Furthermore, it can be seen that the anisotropic behavior becomes less prominent for higher $\mathbf{k}$ values as the exchange energy becomes dominant within this region.

The spin wave propagation velocity within a ferromagnetic film is given by the group velocity v_g and arises directly from the dispersion relation by

$$v_{\mathrm{g}} = \frac{\partial \omega}{\partial k} \tag{2.19}$$

which represents the slope of the dispersion relation. As a result of Eq. (2.19), the group
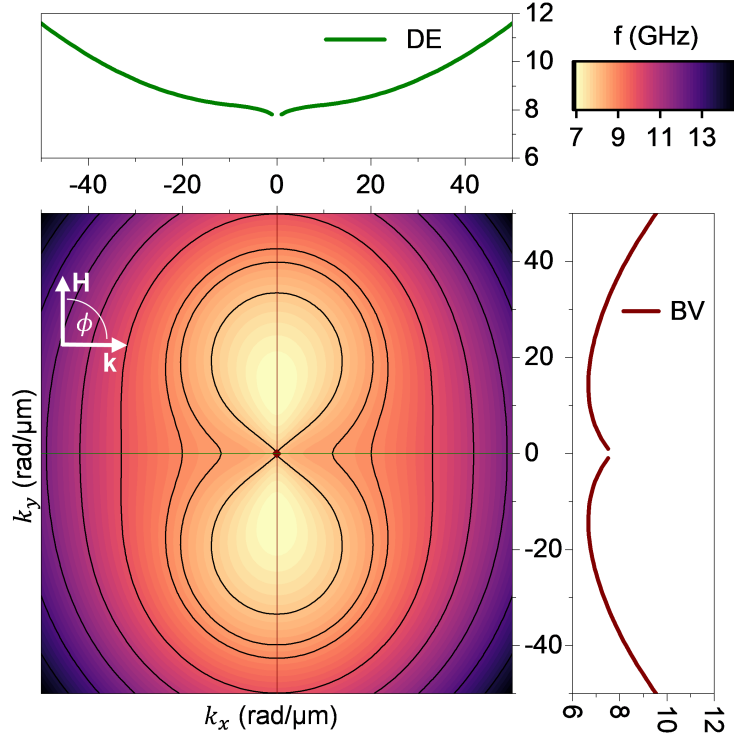
Figure 2.2: Calculated iso-frequency lines of the dispersion relation for arbitrary angles ϕ between the bias magnetic field **H** and the wave-vector **k**. The high symmetry directions for DE ($\phi = \pm\pi/2$) and BV ($\phi = 0, \pi$) are shown above and on the right hand side of the iso-frequency plot, respectively. The parameter for the calculation where L = 200 nm, $\mu_0 H$ = 200 mT, $M_{\rm s}$ = 140 kA/m and $l_{\rm ex}^2 = 3 \cdot 10^{-16}$ m^2 (typical parameters for Yittrium Iron Garnet).

velocity of DE and BV spin waves arises to

$$v_{\rm g,DE} = \frac{\gamma^2 \mu_0^2 M_{\rm s}^2 L}{4\omega}(1 - \zeta) \qquad (2.20)$$

$$v_{\rm g,BV} = -\frac{\gamma^2 \mu_0^2 M_{\rm s} L}{4\omega} H \qquad (2.21)$$

A negative group velocity is obtained for BV spin waves. Consequently, the direction of the wave-vector **k** and the direction of the group velocity are aligned anti-parallel with respect to each other. On the other hand, the wave-vector **k** for DE spin waves is aligned

parallel to the direction of the group velocity. A characteristic damping time τ arises from the imaginary part of the dispersion relation which leads to an attenuation length

$$L_{\text{att}} = \frac{v_{\text{g}}}{\text{Im}(\omega)} = \tau v_g. \tag{2.22}$$

Neglecting exchange contributions in the dispersion relation leads to an attenuation length for DE spin waves of

$$L_{\text{att}}^{\text{DE}} = \frac{v_{\text{g,DE}}}{\alpha \gamma \mu_0 (H + \frac{M_{\text{s}}}{2})}, \tag{2.23}$$

and for BV spin waves of

$$L_{\text{att}}^{\text{BV}} = \frac{v_{\text{g,BV}}}{\alpha \gamma \mu_0 (H + \frac{M_{\text{s}}}{2} - M_{\text{s}}(1 - \zeta))}, \tag{2.24}$$

in which α accounts for the dimensionless damping parameter.

2.3.2 Out-of-Plane Dispersion Relation

The dispersion relation of spin waves propagating within the plane of a thin film becomes isotropic when the magnetization points out of the plane:

$$\omega^2 = \left(\omega_{\text{H}} + \omega_{\text{M}} l_{\text{ex}}^2 k^2\right) \left(\omega_{\text{H}} + \omega_{\text{M}} l_{\text{ex}}^2 k^2 + \omega_{\text{M}} \zeta\right). \tag{2.25}$$

This geometry is named the Forward Volume (FV)-geometry. As the magnetization points normal to the sample surface, the magnetic field H results into $H = H_{ext} - M_{\text{s}}$. As a consequence, in the absence of additional perpendicular anisotropy terms, the external magnetic field has to overcome the saturation magnetization to obtain any propagating spin waves in the FV-geometry. The group velocity is given by

$$v_{\text{g,FV}} = \frac{\gamma^2 \mu_0^2 M_{\text{s}} L}{4\omega} (H_{\text{ext}} - M_{\text{s}}). \tag{2.26}$$
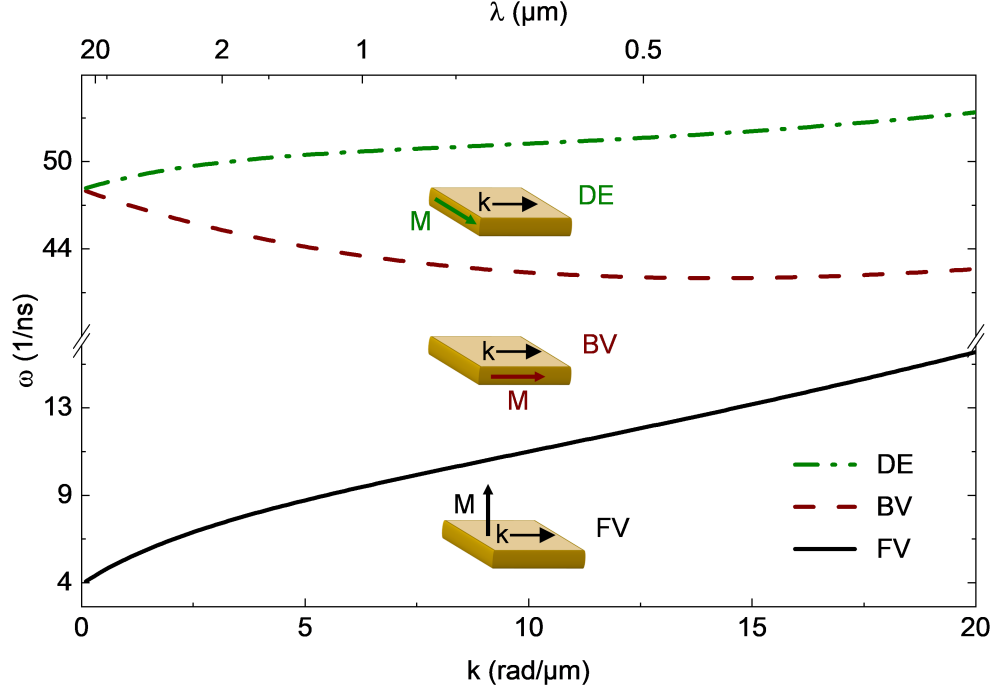
Figure 2.3: Calculated dispersion relation for Damon-Eshbach, Backward Volume and Forward Volume spin waves. The parameter for the L = 200 nm thick YIG film were $\mu_0 H = 200$ mT, $M_\mathrm{s} = 140$ kA/m and $l_\mathrm{ex}^2 = 3 \cdot 10^{-16}$ m^2

As a result, the characteristic attenuation length is given by

$$L_\mathrm{att}^\mathrm{FV} = \frac{v_\mathrm{g,FV}}{\alpha \gamma \mu_0 (\frac{M_\mathrm{s}}{2} \zeta + (H_\mathrm{ext} - M_\mathrm{s}))}. \tag{2.27}$$

The calculated dispersion relation for the above presented geometries (DE, BV, and FV) of a 200 nm thick Yittrium Iron Garnet (YIG) film are presented in Figure 2.3.

2.4 Additional Damping Contributions

The damping characteristics of propagating spin waves are one of the main interests in the field of magnonics. In general, damping arises from various effects, depending on the type of material investigated (e.g. metallic magnets vs. insulating magnets, 3d transition metals vs. 4f rare earth metals etc.). In insulators, for example, magnon-phonon

scattering [6, 62–64] and magnon-magnon scattering [65–67] can lead to an additional damping contribution. Two additional "extrinsic" damping contributions will be investigated in the framework of this thesis. Eddy-current and spin-pumping-induced damping will be considered for a spin wave damping contribution induced by a normal metal in proximity to a thin magnetic insulator YIG. Moreover, we will present that a strong spin wave attenuation arises from the hybridization of two DE spin wave modes.

2.4.1 Eddy-Current-Induced Damping

Eddy-currents are well known phenomena not only in physics but also in industrial applications [68]. They account for the dissipation of energy, induced by a varying magnetic field that penetrates a conductive material. Eddy-currents can be described with the help of the Maxwell-Faraday equation (Eq. (2.28)). It describes that a time-varying magnetic field $\frac{\partial \mathbf{B}}{\partial t}$ always accompanies the curl of an electric field $\nabla \times \mathbf{E}$

$$\nabla \times \mathbf{E} = -\frac{\partial \mathbf{B}}{\partial t}. \tag{2.28}$$

The eddy-current itself, on the other hand, induces a magnetic field opposite to the initial magnetic field, considering Lenz's law. As a consequence, eddy-currents, induced by the time varying magnetic dipolar stray-field generated by a spin wave, induces a magnetic field that is opposite to that of the spin wave. This counter-induction will act as an additional damping factor on a propagating spin wave.

Including the spin wave induced eddy-currents into the LLG-equation of motion leads to an additional damping term α_{ed} [69]

$$\alpha_{\mathrm{ed}} = \frac{\gamma \mu_0^2 M_{\mathrm{s}} \ g^2(k) \ L \ h}{4\rho} \frac{(1+\eta)^2}{1+\eta^2}, \tag{2.29}$$

$$g(k) = \frac{\left(1 - e^{-kh}\right)\left(1 - e^{-kL}\right)}{k^2 th}. \tag{2.30}$$

Here, L accounts for the thickness of the ferromagnetic layer, and h and ρ for the thick-

ness of the normal metal layer and its electrical resistivity, respectively. The ellipticity of the spin wave's precession amplitude induced by the dipolar fields is given by the factor η. The function $g(k)$ is obtained by averaging the magnetic dipolar stray-field over the thickness of the ferromagnetic layer and the eddy-current stray-fields over the thickness of the NM-layer.

2.4.2   Spin-Pumping-Induced Damping

The spin-pumping effect has been found as a method to inject a pure spin current from a ferromagnet into an adjacent normal metal [70–73]. The spin angular momentum of the spin wave is thereby transferred to the normal metal's itinerant electron system [74]. Interestingly, since we describe the transport of angular momentum carried by a spin wave, the magnetic system can be insulating or metallic. A normal metal, which is assumed to have a rapid spin relaxation and does not allow any back-flow of the spin current to the ferromagnetic material, is called a perfect spin-sink. The interfacial spin-pumping induces an additional torque term τ_{sp} to the LLG [Eq. (2.31)], that accounts for an additional damping term α_{sp}. Note that this additional damping terms has the same functional form as the Gilbert damping term and is therefor often called "Gilbert-like" damping. For a deeper understanding of the effect of spin pumping in FM/NM bilayers we refer the reader to [72].

$$\frac{\partial \mathbf{M}}{\partial t} = -\gamma \mu_0 \left(\mathbf{M} \times \mathbf{H}_{\mathrm{eff}} \right) + \frac{\alpha}{M_{\mathrm{s}}} \left(\mathbf{M} \times \frac{\partial \mathbf{M}}{\partial t} \right) + \tau_{\mathrm{sp}} \qquad (2.31)$$

$$\tau_{\mathrm{sp}} = \frac{\alpha_{\mathrm{sp}}}{M_{\mathrm{s}}} \left(\mathbf{M} \times \frac{\partial \mathbf{M}}{\partial t} \right) \qquad (2.32)$$

The spin-pumping effect, and in turn the additional damping parameter α_{sp}, depends not only on the material combination but also on the interface quality concerning the FM/NM [75]. A quantitative parameter describing spin-pumping, considering a perfect spin-sink, is the spin-mixing-conductance $g^{\uparrow\downarrow}$. A more sophisticated parameter is the effective-spin-mixing-conductance $g_{\mathrm{eff}}^{\uparrow\downarrow}$, which takes a partial back-flow from the NM

to the FM into account. Consequently, the additional damping contribution can be expressed by

$$\alpha_{\mathrm{sp}} = \frac{g\mu_B}{4\pi M_{\mathrm{s}}} g_{\mathrm{eff}}^{\uparrow\downarrow} \frac{1}{L} \qquad (2.33)$$

with g the Landé g-factor, μ_B the Bohr magneton, M_{s} the saturation magnetization and L the thickness of the magnetic layer. The back-flow of the spin depends on the spin-sink material parameter and is considered within the effective spin-mixing-conductance [72]

$$g_{\mathrm{eff}}^{\uparrow\downarrow} \approx g^{\uparrow\downarrow} \left(1 + \frac{1}{4\sqrt{\frac{\epsilon}{3}}} \tanh\left(\frac{h}{\lambda_{\mathrm{sd}}}\right) \right)^{-1}. \qquad (2.34)$$

Here, h is the NM-layer thickness, λ_{sd} is the spin diffusion length in the NM, and $\epsilon = \frac{\tau_{\mathrm{M}}}{\tau_{sf}}$ accounts for the ratio of the momentum and spin-flip scattering time, respectively.

2.4.3 Hybridization-Induced Damping

Taking the thickness of a ferromagnetic film into account can lead to the appearance of perpendicular standing spin waves (PSSW). PSSWs are spin waves that are confined within the thickness of the magnetic film. As a consequence, their mode profile across the film thickness, and in turn the wavelength, is quantized and characterized by its mode number n. The wavelength λ_{PSSW} is obtained by

$$\lambda_{PSSW} = \frac{2L}{n}, \qquad (2.35)$$

with $n = 0, 1, 2, ...$ and L the thickness of the magnetic film. Considering PSSWs will also affect the dispersion of spin waves. As a consequence, Eq. (2.14) becomes non-valid concerning in-plane magnetized films. Considering the zeroth order perturbation theory of Kalinikos and Slavin (KS-theory), for totally unpinned surface spins, results in the dispersion relation described by Eq. (2.36) [61]. The angle ϕ describes the angle between

the wave-vector $\mathbf{k}$ and the effective magnetic field H_{eff} ($\pm\frac{\pi}{2}$ for DE and $0, \pi$ for BV).

$$\omega_n^2 = \left(\omega_{\text{H}} + \omega_{\text{M}} l_{\text{ex}}^2 k_n^2\right)\left(\omega_{\text{H}} + \omega_{\text{M}} l_{\text{ex}}^2 k_n^2 + \omega_{\text{M}} F_{nn}\right) \tag{2.36}$$

$$F_{nn} = P_{nn} + \left(1 - P_{nn}(1 + \cos^2\phi) + \omega_{\text{M}}\frac{P_{nn}(1 - P_{nn})\sin^2\phi}{(\omega_{\text{H}} + \omega_{\text{M}} l_{\text{ex}}^2 k_n^2)}\right) \tag{2.37}$$

$$P_{nn} = \frac{k_x^2}{(k_x^2 + k_z^2)^2} - \frac{k_x^4}{k_x^4 k_z^4} F_n \left[(1 + \delta_{0n})(1 + \delta_{0n})\right]^{-1} \tag{2.38}$$

$$F_n = \frac{2}{k_x L}\left[1 - (-1)^n \exp(-k_x L)\right] \tag{2.39}$$

Figure 2.4 (a) presents the dispersion of the n = 0 and n = 1 DE and BV spin waves. A frequency degeneracy of the n = 0 and n = 1 mode is observed for DE spin waves but not for BV spin wave modes. That frequency degeneracy, i.e., mode crossing, may result in an avoided crossing if the modes interact with each other, i.e., if they are hybridized. The calculation of the anti-crossing can be realized by various methods. Using a higher order perturbation theory of the KS-theory will result in a suitable solution of the dispersion but requires a considerable computational effort [61]. Alternatively, the dynamic matrix method can be used which is based on the linearization of the LLG and transforming it into an eigenvalue problem [76]. TETRAX is an open-source Python script that is based on that method. It can be used for solving the LLG by using a finite-element micromagnetic code [77,78]. Figure 2.4 (b) presents the DE dispersion in the vicinity of the frequency degeneracy for the DE n = 0 and n = 1 mode, calculated by TETRAX. The coupling between these two modes results in an anti-crossing, with the width of the anti-crossing gap defining the strength of the coupling. The slope of the dispersion decreases and approaches zero in the vicinity of the hybridization. Decreasing the slope of the dispersion results in a reduced group velocity [cf. Eq. (2.19)] and in turn to a shorter attenuation length of the spin wave [cf. Eq. (2.22)].
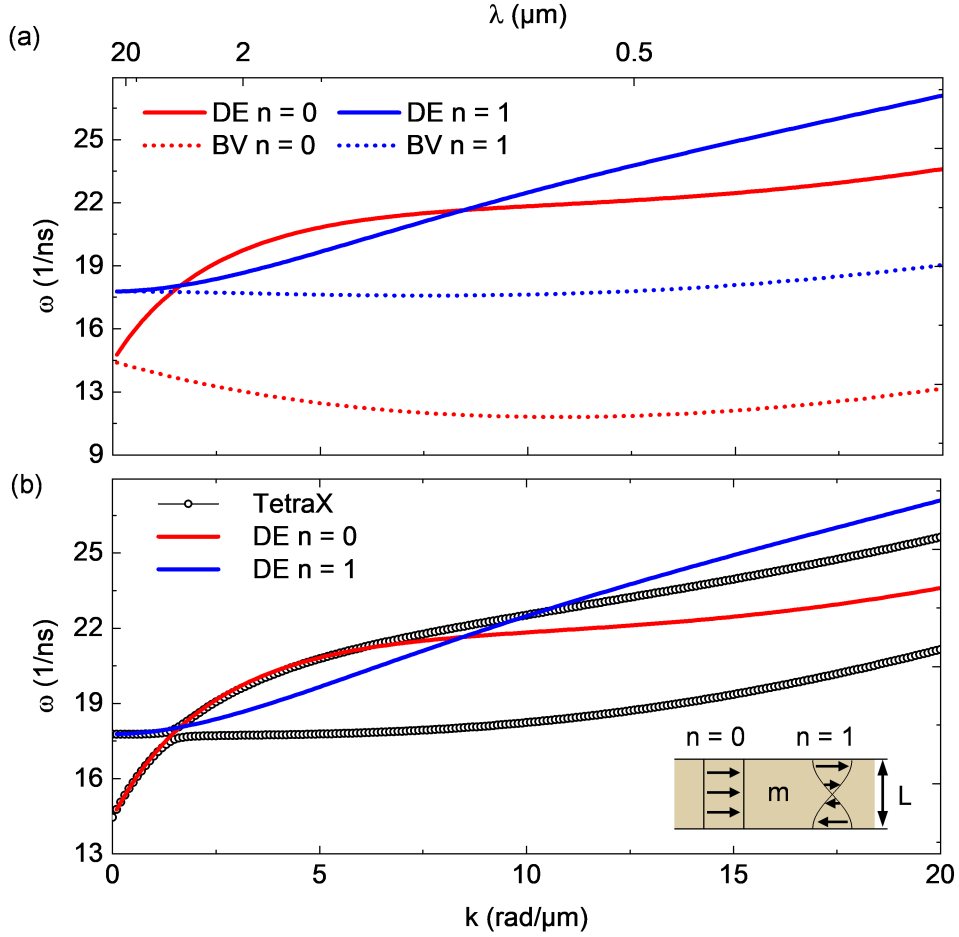
Figure 2.4: (a) Calculated dispersion relation using the zeroth-order perturbation theory by Kalinikos and Slavin (KS) for the n = 0 and the n = 1 DE and BV spin wave modes. (b) Comparison of KS and TETRAX. The latter demonstrates the anti-crossing of the n = 0 and the n = 1 DE mode in the vicinity of the hybridization.

2.5   Surface-Wave Non-Reciprocity

Considering the dispersion of magnetostatic surface waves, propagating parallel to the surface and normally to the magnetization (DE-geometry), demonstrates that the angular frequency ω does not depend on the direction of the magnetization $\mathbf{M}$ [54]

$$\omega^2 = \left(\omega_{\mathrm{H}} + \frac{\omega_{\mathrm{M}}}{2}\right)^2 - \left(\frac{\omega_{\mathrm{M}}}{2}\right)^2 \exp(-2kL). \tag{2.40}$$

The angular frequency lies in the range $\omega_{\perp} \leq \omega \leq \omega_{\mathrm{H}} + \frac{\omega_{\mathrm{M}}}{2}$ with $\omega_{\perp} = \omega(k = 0) = \sqrt{\omega_{\mathrm{H}}(\omega_{\mathrm{H}} + \omega_{\mathrm{M}})}$, shown in Figure 2.5 (a). Adjoining an electrical conductor to the magnetic material can break this reciprocity [79–81]. In 1970, Seshadri first investigated that the wave-number as well as the group velocity of magnetostatic surface waves becomes non-reciprocal if a ferrite slab is in proximity to a metal plate [79]. By considering a perfect electrical conductor (PEC) placed against one side of the ferrite slab, he found that the dispersion relation for a magnetostatic surface wave becomes Eq. (2.41). In contrast to the dispersion without any conductor, the dispersion now includes the parameter $s = \pm 1$, which accounts for the positive or negative propagation direction.

$$\exp(-2kL) = \left(1 + 2\frac{\omega_{\mathrm{H}}}{\omega_{\mathrm{M}}} + 2s\frac{\omega}{\omega_{\mathrm{M}}}\right)\frac{\omega_{\mathrm{H}} + \omega_{\mathrm{M}} - s\omega}{\omega_{\mathrm{H}} + \omega_{\mathrm{M}} + s\omega} \tag{2.41}$$

Figure 2.5 (b) presents the dispersion for both s-values. The positive s-value accounts for spin waves propagating at the top surface which is in proximity to the PEC, whereas the negative s-value describes the propagation at the opposite surface, without any conducting material. It can be seen that the dispersion is shifted to higher frequencies for magnetostatic surface waves that propagate at the surface with the PEC on top ($s = 1$), i.e., the reciprocity for DE spin wave modes is broken and the frequency lies in the range $\omega_{\perp} \leq \omega \leq \omega_{\mathrm{H}} + \omega_{\mathrm{M}}$ for $s = 1$.
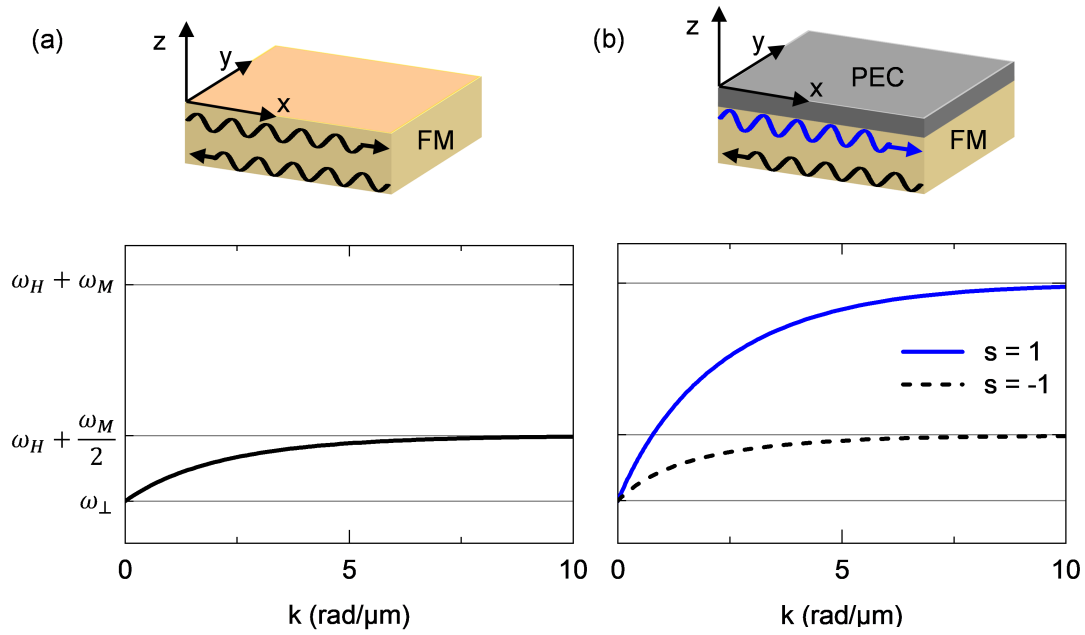
Figure 2.5: Calculated dispersion of magnetostatic surface waves of a ferromagnet (FM) in vacuum (a) and in proximity to a perfect electrical conductor (PEC) (b). The presence of the PEC breaks the reciprocity of the surface waves and shifts the dispersion to higher frequencies of spin waves propagating at the top surface, with respect to spin waves propagating at the lower surface.

2.6 Jones Formalism

In 1861, James Clerk Maxwell published a set of equations which describe the relationship between magnetism and electricity [82]. With the help of modern vector notation, this set of equations can be written as [83]:

$$\nabla \cdot \mathbf{E} = \frac{1}{\epsilon_0} \rho \tag{2.42}$$

$$\nabla \cdot \mathbf{B} = 0 \tag{2.43}$$

$$\nabla \times \mathbf{E} = -\frac{\partial \mathbf{B}}{\partial t} \tag{2.44}$$

$$\nabla \times \mathbf{B} = \mu_0 \epsilon_0 \frac{\partial \mathbf{E}}{\partial t} + \mu_0 \mathbf{J} \tag{2.45}$$

where $\mathbf{E}$, $\mathbf{B}$, ρ and $\mathbf{J}$ represent the electric field, the magnetic field, the electric charge density and the current density, respectively. A non trivial solution for the Maxwell equations can be written as:

$$\mathbf{E}(\mathbf{r}, t) = \mathbf{E}_0 \cdot e^{i(\mathbf{k} \cdot \mathbf{r} - \omega t)} \tag{2.46}$$

$$\mathbf{B}(\mathbf{r}, t) = \mathbf{B}_0 \cdot e^{i(\mathbf{k} \cdot \mathbf{r} - \omega t)} \tag{2.47}$$

with the complex amplitudes $\mathbf{E}_0$ and $\mathbf{B}_0$, the wave-vector $\mathbf{k}$, the direction of propagation $\mathbf{r}$, the angular frequency of the electromagnetic wave ω and the time t. Considering the complex amplitude in Eq. (2.46) and the direction of propagation to be in the z-direction, the wave equation becomes Eq. (2.48), whereas $\mathbf{E}_0$ can be written as a superposition of the electric field oscillating in the x- and y-direction.

$$\mathbf{E}(z, t) = (E_x \hat{\mathbf{x}} + E_y \hat{\mathbf{y}}) e^{i(\mathbf{k}z - \omega t)} \tag{2.48}$$

There is a large amount of optical elements which can be used to manipulate the propagation of light. In 1941, R. Clark Jones introduced a two-dimensional matrix algebra which describes the effect of optical elements on polarized light [84]. The Jones vector can be written as

$$\begin{bmatrix} A \\ Be^{i\delta} \end{bmatrix} \tag{2.49}$$

with

$$A \equiv \frac{|E_x|}{\sqrt{|E_x|^2 + |E_y|^2}} \tag{2.50}$$

$$B \equiv \frac{|E_y|}{\sqrt{|E_x|^2 + |E_y|^2}} \tag{2.51}$$

$$\delta \equiv \Phi_y - \Phi_x. \tag{2.52}$$

The Jones vector can be used to describe the polarization state of any plane electromagnetic wave. Furthermore, a 2 x 2 matrix $\mathbf{J}_N$ can be defined which can express any optical element which interacts with an electromagnetic wave. A system of several optical elements can be represented with such Jones matrices $\mathbf{J}_{\text{system}}$ [cf. Eq. (2.53)]. A linear polarizer, wave plates (WP) and the reflection from or the transmission through an interface are just a few examples for optical elements which can be described by the Jones formalism.

$$\mathbf{J}_{\text{system}} \equiv \mathbf{J}_N \mathbf{J}_{N-1}...\mathbf{J}_2 \mathbf{J}_1 \tag{2.53}$$

$$\begin{bmatrix} A' \\ B' \end{bmatrix} = \mathbf{J}_{\text{system}} \begin{bmatrix} A \\ Be^{i\delta} \end{bmatrix} \tag{2.54}$$

Note that A and B are real, dimensionless, and non-negative numbers. They always satisfy the equation $A^2 + B^2 = 1$. The vector on the right-hand side of Eq. (2.54)

represents the electric field components for light interacting with a system of optical elements, described by the Jones matrix $\mathbf{J}_{\text{system}}$. The resulting polarization state of the electromagnetic wave is given by the left-hand side of Eq. (2.54). An application of this formalism will be demonstrated in Section 5.3.

2.7 Magneto-Optical-Effects

To measure the state of the magnetization of a ferro- or ferri-magnetic material, we will take advantage of the Magneto Optical Kerr Effect (MOKE). The MOKE was first discovered in 1877 by John Kerr: "When plane-polarized light is reflected perpendicularly from the polar surface of an iron electromagnet, the plane of polarization is turned through a small angle in a direction contrary to the nominal direction of the magnetizing current." [85]

The optical response of a material can be described either by the optical susceptibility $\boldsymbol{\chi}$ [Eq. (2.55)] or by the permittivity tensor $\boldsymbol{\epsilon} = \epsilon_0 \epsilon_r$. The permittivity tensor correlates the driving electric field $\mathbf{E}$ to the dielectric displacement $\mathbf{D}$ [Eq. (2.57)]. Both are related to each other by Eq. (2.56). In a non-absorbing, nonmagnetic crystal with cubic symmetry, $\boldsymbol{\epsilon}$ becomes real and symmetric, i.e. $\epsilon_{ij} = \epsilon_{ji}^*$. As a consequence, the off-diagonal elements become zero.

$$\mathbf{P} = \epsilon_0 \chi(\omega)\mathbf{E}(\omega) \tag{2.55}$$

$$\boldsymbol{\epsilon} = \epsilon_0(1 + \boldsymbol{\chi}) \tag{2.56}$$

$$\mathbf{D} = \boldsymbol{\epsilon}(\omega)\mathbf{E} \tag{2.57}$$

On the other hand, if the magnetization $\mathbf{M}$ of a material is nonzero, but, for example, in the z-direction of the crystal, the symmetry changes and the permittivity tensor becomes Eq. (2.58) [57]. The index of refraction $\mathcal{N} = \sqrt{\epsilon_r}$ as well as the magneto-optic parameter Q have real and imaginary parts, which define the magneto-optic properties

of a material.

$$\epsilon(\mathbf{M}, \omega) = \epsilon_0 \epsilon_r \begin{bmatrix} 1 & iQ & 0 \\ -iQ & 1 & 0 \\ 0 & 0 & 1 \end{bmatrix} \tag{2.58}$$

$$\mathcal{N} = \sqrt{\epsilon_r} = n - i\kappa \tag{2.59}$$

$$Q = q' - iq'' \tag{2.60}$$

As a consequence, the permittivity tensor becomes a function of the magnetization $\mathbf{M}$. Eq. (2.58) indicates that the magnetization $\mathbf{M}$ induces an optical anisotropy to magnetic materials. Magnetic dichroism, and with this Faraday or Kerr rotation, occurs from the non-zero off-diagonal elements of the permittivity tensor [57]. A change in the direction of the polarization occurs due to the magnetic dichroism if we consider linearly polarized light as a superposition of right-handed σ^+ and left-handed σ^- polarized light. σ^+ and σ^- polarized light propagates with a different velocity through the magnetic crystal, which results in a phase shift between them. The phase shift depends on the magnetization of the sample, the material, as well as on the optical pathway through the crystal. The rotation of the polarization, as a result of this phase shift, is called the Faraday-rotation

$$\theta_F \propto V \cdot B \cdot l \tag{2.61}$$

with V the Verdet constant, a material constant that depends on the wavelength and defines the strength of the polarization rotation, B is the effective magnetic field inside the crystal, and l is the length of the optical path inside the crystal. The Faraday rotation strongly depends on the wavelength of the probing light and is given in degree per unit length. Table 2.1 shows exemplary the Faraday rotation of ferromagnetic metals using a wavelength of 830 nm ($E_{\mathrm{photon}} = 1.5$ eV). A value of the Faraday rotation of

Table 2.1: Faraday and Kerr rotation of ferromagnetic metals at 830 nm [57].

	θ_F (° μm^{-1})	θ_K (°)
Fe	35	-0,53
Co	36	-0,36
Ni	10	-0,09
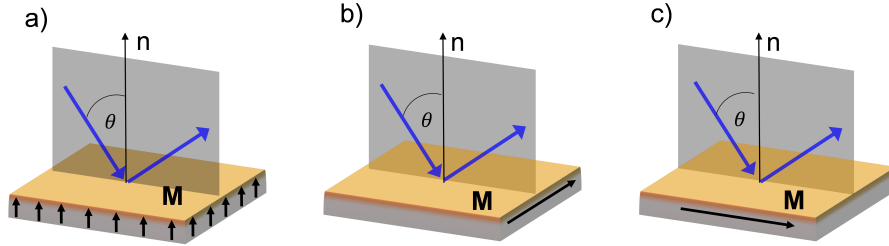
Figure 2.6: Polar- (a), transverse- (b) and longitudinal- (c) MOKE configuration. The grey shaded area indicates the plane of incidence of the linearly polarized light, indicated by the blue arrows.

the ferrimagnetic insulator YIG, using light with a wavelength of $\lambda = 1.06\,\mu$m, reads $28\,°\,\mathrm{mm}^{-1}$ [57]. The MOKE is closely related to the Faraday-Effect whereas reflection on a magnetic material is considered instead of transmission through it. As a consequence, the MOKE is independent of the length or thickness of the ferromagnetic material but can be considered as a surface sensitive probe technique. The Kerr rotation also depends on the wavelength of the probing light. Using light with a wavelength of $\lambda = 830\,\mathrm{nm}$ leads to a Kerr rotation of ferromagnetic metals presented in Table 2.1 [57].

There are three high symmetry configurations for MOKE, schematically shown in Figure 2.6. They can be distinguished by the direction of the magnetization with respect to the plane of incidence of the linearly polarized light. The out-of-plane magnetization can be probed by the polar MOKE, which gives the largest polarization rotation for light with a normal incidence ($\theta = 0°$), see Fig. 2.6 (a). Measuring the in-plane component of the magnetization can be realized with the help of the longitudinal or the transversal MOKE, depending on the magnetization direction with respect to the plane of incidence of the linearly polarized light, see Fig. 2.6 (b) and (c). Only the wave-vector contribution

of the polarized light pointing in the direction of the magnetization will contribute to a polarization rotation. As a consequence, the larger the angle of incidence θ, the larger the effect of the longitudinal and transversal MOKE. Using a standard objective lens with a numerical aperture (NA) of 0.7, for example, leads to a maximum angle of incidence of $\theta \approx 45°$. The NA describes the angle over which the objective lens can collect or emit light and is described by

$$NA = n \cdot \sin(\theta) \tag{2.62}$$

where n is the index of refraction of the medium which surrounds the optical element (n = 1 for air). As the angle of incidence θ can not approach 90°, the polar MOKE can be considered as the MOKE that leads to the largest polarization rotation concerning the three MOKE configurations.

Chapter 3

Experimental Techniques

Imaging the magnetization of ferro- and ferrimagnetic materials can be realized with the help of the Magneto Optical Kerr Effect (MOKE). Today, Magneto Optical Kerr Microscopes are a standard used in the laboratory to image static magnetization [86–91]. However, if we want to image dynamic magnetization processes, which are typically in the range of 10^{-9} s or faster, static imaging with a camera and a continuous wide light source is no longer sufficient. There are a few techniques up to now which have been used to overcome the static limitations for imaging dynamic magnetization processes. Brillouin Light Scattering (BLS) [92–94], Time-Resolved Scanning Transmission X-ray Microscopy (TR-STXM) [95–98] and Time-Resolved MOKE (TR-MOKE) [31, 99–102] are common techniques used to image magnetization dynamics with spatial and time resolution in the GHz to THz range. The BLS technique acquires data in the frequency domain whereas the TR-STXM as well as the TR-MOKE technique are measuring in the time domain. To observe the spatial landscape of a magnetization distribution it is necessary to scan the sample along two dimensions. A standard solution for this is to mount the sample on a piezo-driven scanning-stage. The sample is then scanned underneath a focused laser or X-ray beam which is used to measure the state of the magnetization at any point in space within a two-dimensional plane by the BLS, TR-STXM or TR-MOKE methods.

The BLS technique exploits the inelastic scattering of photons from magnons, i.e.,

the associated quantum particle of spin waves, to measure the magnetization dynamics of a sample. After the interaction, the inelastic shift in frequency of the scattered photon is the very same as the magnon frequency, i.e. the frequency of the spin wave. The frequency shift can be analysed by an interferometric measurement principle. Describing this technique in detail is beyond the scope of this thesis and can be found elsewhere [92]. The main advantage of the BLS technique for the study of magnetization dynamics is the possibility to measure not only coherently excited magnetization dynamics but also incoherent dynamics, such as thermal spin waves.

The TR-STXM method takes advantage of the X-ray magnetic circular dichroism (XMCD) effect, which accounts for the difference in absorption for left- and right-handed circularly polarized X-rays, depending on the orientation of the magnetization [103]. It basically uses the same effect as the MOKE but in the X-ray regime instead of the visible light (VIS) regime. The X-ray pulses are usually provided by a synchrotron radiation source which makes this technique a rather complex and expensive measurement approach, compared to a table-top system such as BLS. The main advantages of the TR-STXM method are its high spatial resolution as well as its element selectivity. As the spatial resolution of optical systems (e.g., visible and X-ray radiation) is related to the wavelength of the light-source, X-rays can be used to image structures or wavelengths down to about 20 nanometer (nm), whereas BLS and TR-MOKE are limited to a spatial resolution of about 200 nm.

In this thesis, the main measurement technique used is the TR-MOKE technique which will be described in detail in Section 3.1. Moreover, to facilitate the experimental measurements outlined in this thesis, two independent TR-MOKE setups were first constructed from the ground up.

The first setup uses a piezo-slip-stick-positioner to control the sample position. The special feature of this setup is that the piezo-stage, as well as the objective lens, are placed inside a custom-made cryostat allowing measurements of the magnetization dynamics down to about 10 K. The second TR-MOKE setup is a prototype system, designed to operate at room temperature but with an added functionality to allow scanning

measurements similar to that already used in scanning fluorescence microscopy [104,105]. To the best of our knowledge, such a scanning system with the capability to measure polarization sensitive quantities like the MOKE had not been demonstrated prior to this thesis.

3.1   TR-MOKE

Figure 3.1 demonstrates a schematic of the TR-MOKE setup and measurement principle. The TR-MOKE technique is based on the stroboscopic measurement principle, allowing only coherent and reproducible phenomena to be probed. To measure coherent excited spin waves in the nanosecond (GHz) time (frequency) regime, an event which is faster than the nanosecond scale is necessary. For our experimental setup, femtosecond laser pulses (fs-pulses) with a repetition rate of 80 MHz are provided by a Mira-laser system. The fs-pulses are synchronized to a rf-generator which is used to coherently excite the spin waves via coplanar waveguides (CPW). The synchronization is realized by a Rubidium-driven atomic clock which provides a high precision 10 MHz sinusoidal output. This sinusoidal output is used as the clock for the repetition rate of the laser (multiplied by a factor of 8 resulting in 80 MHz) and for the rf-generator. The repetition rate of the fs-pulses is controlled by stabilizing the cavity length of the laser. This is realized by a proportional, integral and differential (PID) controlled piezo-electric-actuator in combination with a linear-motor-actuator, inside the laser cavity. Both actuators control the position of an individual mirror and with this the precise length of the laser cavity. Initially the laser cavity did not include this additional control parameter, and as a result it was upgraded with a custom-made system. For the stroboscopic measurements, the spin wave excitation frequency has to be a multiple integer of the 80 MHz repetition rate to ensure that every laser pulse hits the spin wave with the very same phase at the sample surface. This limitation can be overcome with the so-called under-sampling or super-Nyquist technique which has been detailed elsewhere [106].

The magnetization dynamics, i.e. spin waves, are excited by a rf-current, driven
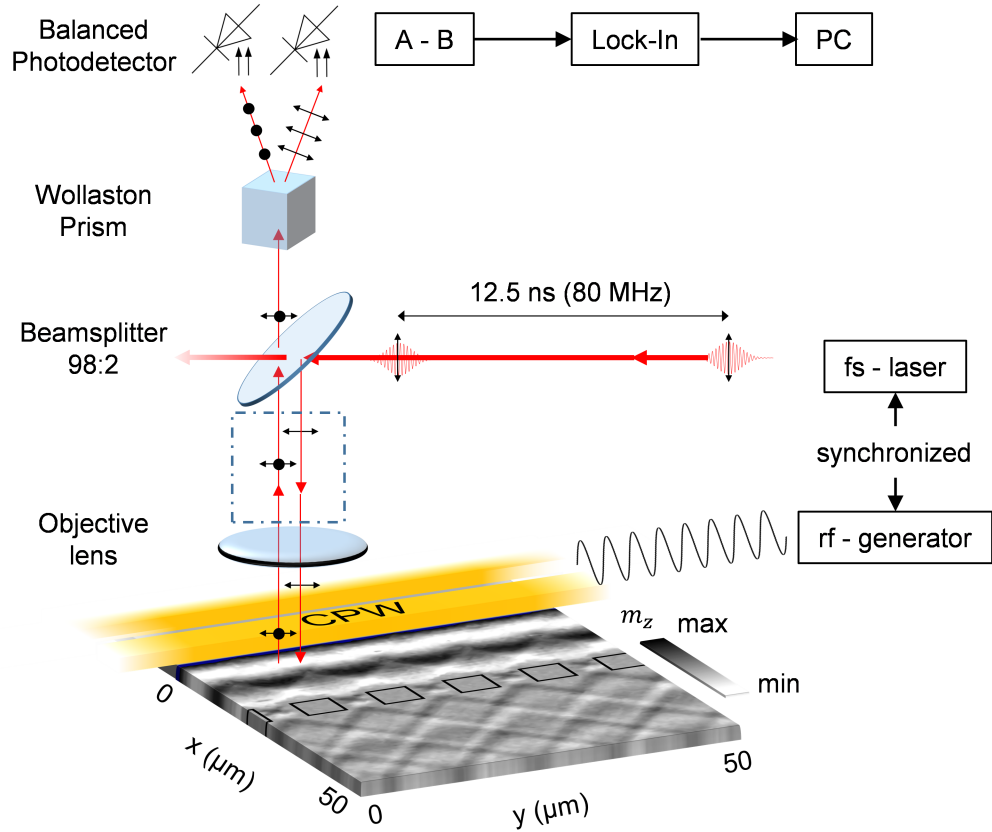
Figure 3.1: Schematic overview of a standard TR-MOKE setup. Femtosecond laser pulses are used for stroboscopic measurement of coherently excited spin waves. A galvo-galvo system is used for scanning the laser pulses across the sample surface (placed at the position marked by the dashed rectangle). Alternatively, the sample can be moved via a xyz piezo scanning stage to scan the sample surface with respect to the laser focus. Both systems are used in the present work.

through a coplanar waveguide (CPW) by the rf-generator. The CPW's used in this thesis are made out of 100 nm Au with a 5 nm Cr or Ti buffer layer, deposited directly on top of a ferro- or ferrimagnetic film by photo-lithographic processing. A pellicle beamsplitter is used to guide the fs-pulses to the objective lens. The transmission (T) or reflection (R) ratio of the fs-pulses from the pellicle beamsplitter is polarization dependent. Using this property, the polarization for the incoming fs-pulses is set to a p-polarized state to achieve a T:R ratio of 98:2 for the pellicle. As a result, only 2% of the incoming fs-pulse intensity is guided to the objective lens and later onto the sample surface. The remaining 98% of the laser-pulse intensity is wasted and blocked from further propagation. Nevertheless, as the average laser power provided by the Mira-laser is about 250 mW, which is high enough so that even the 2% of the initial laser power can be sufficient to heat the sample or to even thermally destroy it.

Upon reflection at the magnetized sample surface, the polarization plane of the fs-pulses is turned by a small portion (MOKE). This small portion is directly proportional to the z-component of the magnetization at the sample surface as we are taking advantage of the polar-MOKE effect. The reflected fs-pulses propagate backwards through the objective lens to the pellicle beamsplitter. At this stage, 98% of the fs-pulse intensity will propagate through the pellicle whereas only 2% gets reflected back towards the laser source. An optical diode is placed in front of the laser to avoid instabilities inside the laser cavity, caused by the back reflected laser pulses. The advantage for the 98:2 ratio is that the detector-path which measures the Kerr-rotation and with this the z-component of the magnetization, is placed in the direction of the laser propagation (see also Fig. 3.1). Only 2% of the laser light, which now contains the MOKE signal, is wasted whereas 98% is guided to the detector.

A Wollaston prism placed in front of the photodetector splits the incoming light into two paths which have a perpendicular orientation of the polarization with respect to each other. The two beams are focused onto the photodetector which contains two independent photodiodes (A and B). A differential signal of the photo-diodes (A-B) is provided by the photodetector which is directly proportional to the rotation of the

polarization and with this to the MOKE signal. The differential signal is connected to a lock-in detector to enhance the signal-to-noise ratio (SNR). The modulation, which is necessary for the lock-in technique, is applied to the rf-current. A multiplication of the rf-current by a rectangular-shaped current in the kHz range causes a phase shift of 180° to the rf-current and the spin wave amplitude at a given point in time and space. This modulates the differential signal (A - B) with the same frequency in the kHz range which can be demodulated by a lock-in amplifier.

The z-component of the magnetization is observed using the method described above for every individual point in time and space. To record a two-dimensional image of the magnetization dynamics, it is necessary to move the sample with respect to the laser-focus position. As previously mentioned, this can be done by a computer controlled xyz piezo-stage. Alternatively to the piezo-stage, a galvo-galvo mirror system can be incorporated into the system to setup the prototype scanning TR-MOKE system. The galvo-galvo scanning system is well-known from scanning optical microscopes such as those used in confocal-fluorescence microscopy, however, to the best of our knowledge has not been shown to work for magneto-optical experiments up to now. The system can be included to the TR-MOKE setup at the position marked by the blue dashed rectangle in Fig. 3.1.

3.2   Galvo-Galvo Scanning System

Figure 3.2 demonstrates the working principle of a galvo-galvo scanning system. The overall aim is to scan a laser-focus across the sample surface while ensuring the laser is always directed perpendicular to the sample surface. This protocol ensures that the incoming laser path is identical to the back reflected laser path. This is necessary to ensure that the laser position at the photodetector diodes is stable. Otherwise, the laser position at the photo-diodes would move together with the laser on the sample surface which would cause an uncertainty, or even a loss, of the signal if the laser is no longer incident upon the photodetector diodes. The galvo-galvo scanning system consists of two

main optical groups. The first optical group contains two mirrors mounted on individual current-controlled galvanometers. Those galvanometers control the rotation angle of the two mirrors and with this the scan direction of the laser across the sample surface for M1 (M2) in the x (y)-direction. The deflected laser pulses undergo a second deflection by a scan-lens system which consists of two individual lens groups, including the scan lens (SL) and the so-called tube lens (TL). The scan lens system resembles a Kepler-like telescope which focuses the deflected beam into the focal plane of the scan- and tube-lens. The scan- and the tube-lens are mounted in a way that their focal planes coincide with each other, like for a Kepler-telescope. The scan lens system ensures that the angle of incidence to the objective lens is such that the focused laser on the sample surface is always perpendicular to the sample surface. Once the focused laser, or laser pulses, hits the sample surface perpendicular to itself, the back reflected beam-path will be the very same as the incoming path. This ensures a stable position of the laser at the photo-diodes sensitive areas. Changing the optical path length due to the galvo-galvo scanning mechanism will also lead to a time delay between fs-pulses at different scanning positions. The difference of the optical path for the fs-pulses is in the cm range and as a result in the ps time regime, i.e., about $33\,\mathrm{ps\,cm}^{-1}$. The time regime of the magnetization dynamics, investigated in this thesis, is in the ns-range. As a consequence, the time difference in the ps range is negligible for this thesis but should be considered for experiments within the THz dynamics.

An open question concerning the galvo-galvo scanning system is if all the additional optical components, compared to a system controlled only by a xyz piezo-stage, disturbs the polarization state of the laser and as a consequence the polarization-sensitive MOKE signal. Stress induced polarization, coming from optical components which are mounted with too much strain, for example, could affect the polarization state of the laser and with this the MOKE signal.
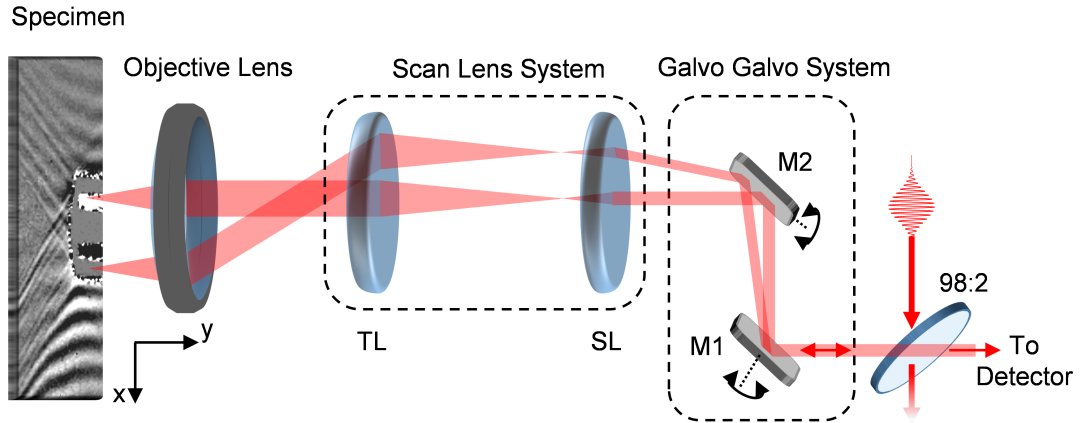
Figure 3.2: Schematic overview of a Galvo-Galvo scanning system, used in one of the TR-MOKE setups. Two independent mirror galvanometers (M1 and M2) are used to deflect the incoming laser pulses in two dimensions. A scan lens system focusses the deflected beam into the focal plane of the scan-lens (SL) and tube lens (TL), forming a Kepler-like telescope. The scan lens system ensures an angle of incidence to the objective lens such as the focused beam is always perpendicular to the sample surface. This ensures that the incoming beam path is identical to the reflected beam path.

3.3 Proof-of-Principle Measurements

Fig. 3.3 (a) demonstrates one of the first measurements observed with the prototype galvo-galvo TR-MOKE system. It shows a topographic image scan of a sample which was previously characterized during earlier experiments [36]. The sample consists of a 60 nm (30 nm) Py layer in the left upper (lower) area. The black contrast represents a Si/SiO_2 substrate whereas the CPW consists of 200 nm Au. The scan range is given in volts (V) as this is the control unit for the position of each galvo-mirror. The actual scan distance depends on the magnification of the objective lens which is used for the experiment. An objective lens with a lower magnification gives a bigger scan distance per galvo-mirror angle or control voltage. A 25×0.6 objective lens was used to scan the image shown in Fig. 3.3 (a). There seems to be neither astigmatism nor distortion for the presented scanning range.

There are two advantages of the galvo-galvo-system, compared to a piezo-scanning

system, identified so far. The possible scanning range in the x- and y-direction can be adjusted by simply changing the objective lens, whereas the possible scanning range is fixed for a standard piezo-stage to about 100 µm to 200 µm. The second advantage is that the achievable scanning range is far beyond that of a standard piezo-stage. A little cumbersome point is that the voltage-to-length ratio of the galvo-galvo system needs to be calibrated prior to measurement using a calibration sample. However, this can in principle be done with any sample exhibiting well-defined dimensions in the x- and y-directions.

To measure magneto-optical contrast, we will consider the polar-Kerr effect. A first measurement of magnetic contrast is shown in Fig. 3.3 (b). A film of 7 ML Co, which shows a perpendicular magnetic anisotropy (PMA), was used for this first test. The measurement demonstrates a clear change in contrast for the different orientations of the sample magnetization, indicated by the varying grey-scale values. The image was manipulated by image processing to subtract a background using a rolling ball subtraction. Even after the image processing there are some remaining artifacts in the image, suggesting that the image processing could be further improved. However, comparing this image obtained by the galvo-galvo-scanning system with an image observed at the same area by a static MOKE-microscope, shown in Fig. 3.3 (c), demonstrates that the galvo-galvo system can be used for polarization sensitive experiments. The SNR for measuring static phenomena, like the static magnetization presented in Fig. 3.3 (b), is usually less compared to dynamic measurements.

The same sample as shown in Fig. 3.3 (a) was used to first demonstrate the measurement for propagating dynamic magnetization, i.e. spin waves. The fs-pulses where scanned by the galvo-galvo-system across the CPW, indicated with the red dashed line in Fig. 3.3 (a). A rf-current of 8 GHz was sent through the CPW and a bias magnetic field of about 56 mT was applied along the direction of the CPW. Damon-Eshbach (DE) like spin waves are excited in this geometry, which are surface spin waves. A surface spin wave has the characteristic to have a larger amplitude at the top or bottom surface of a plane magnetic film, depending on the direction of the magnetization or the site of the
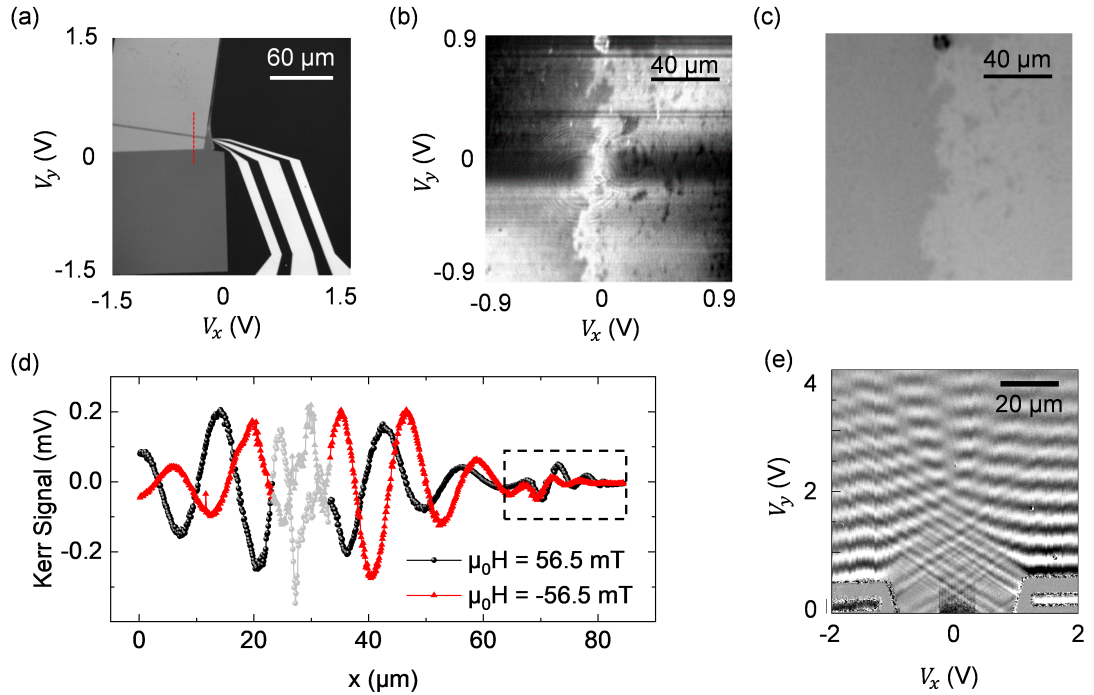
Figure 3.3: Demonstration of the functionality of the galvo-galvo TR-MOKE system. (a) A topographic image of a Py sample surface, recorded by scanning a laser across the sample surface, using the galvo mirrors. The gray scale indicates the intensity of the back reflected laser light. (b) Polar scanning MOKE measurement of magnetic domains from a material exhibiting PMA. The contrast corresponds to opposite directions of the magnetization perpendicular to the sample surface. (c) Wide-field MOKE microscope image for the same sample area presented in (b). (d) Spatially resolved TR-MOKE measurement of propagating DE-like spin waves, measured at the position marked with the red dashed line in (a). (e) Two-dimensional TR-MOKE measurement of propagating spin waves, excited by two separate CPW's at a rf-frequency of 4.96 GHz and a bias magnetic field of 107 mT.

CPW [107, 108]. Fig. 3.3 (d) shows the differential signal (A - B) of the balanced photodetector as a function of the laser position on the sample surface. The control voltage for the galvo-galvo system has been calibrated for this measurement which is why we can plot the x-dimension in µm (and not in V). The black (red) data-points represent the measurement for a positive (negative) bias magnetic field direction pointing along the CPW. It is observable that the spin wave amplitude for the positive bias magnetic field direction (black curve) is larger on the negative x-direction (left hand site of the CPW), whereas the amplitude for the negative bias magnetic field direction is larger on the positive x-direction (right hand site of the CPW). The larger amplitude indicates the surface-wave character which has a higher amplitude at the top surface of the Py film. The black dashed rectangle in Fig. 3.3 (d) marks the area where the thickness of the Py steps from 60 µm to 30 µm. As already shown in previous work [36], the amplitude for the spin waves which has a higher amplitude at the lower surface of the Py (black curve) is enhanced after the thickness step, compared to the spin wave with a higher amplitude at the upper surface. The reflection coefficient for the spin waves is bigger for the upper spin wave (red curve) than for the lower spin wave (black curve), leading to the observed change in amplitude. To gain a higher spatial resolution, another objective lens was used for this measurement. We decided for a 63×0.7 from Leica with an adjustable cover glass correction. The cover glass correction was chosen to allow the possibility to include a cryostat to the setup for which we would have to focus through a 0.5 mm thick glass-window.

Fig. 3.3 (e) demonstrates a two-dimensional measurement for propagating DE-like spin waves in a 200 nm Yittrium Iron Garnet (YIG) film. The spin waves where excited by two separate CPW's connected to two separate rf-generators. The rf-frequency was set to 4.96 GHz for both rf-generators and a bias magnetic field of 107 mT was applied. The left CPW was connected to a HP8672A rf-generator, whereas the right CPW was connected to a Rhode and Schwarz SMA100B rf-generator. The spin wave emission characteristic from the end of the CPW is observed, as well as the interference pattern of two separately excited coherent spin waves. The end of the CPW seems to emit

caustic-like spin wave beams which interact with the propagating spin waves excited by their respective CPW. Further descriptions about similar phenomena will be given in the following sections.

Overall, Fig. 3.3 demonstrates the possibility to realize polarization sensitive measurements with a galvo-galvo-scanning TR-MOKE setup. Imaging static magnetization as well as dynamic magnetization was demonstrated for different magnetic samples. It has to be mentioned that only the polar-Kerr effect can be observed by this technique, as the direction of the incident laser must always be perpendicular to the sample surface. The possible scanning range can easily be adapted to the experiment by simply changing the objective lens. As the sample does not have to be moved to observe the two-dimensional image, the rf-cables attached to the sample holder can be securely mounted as well. Moving such rf-cables, or other physical connections to the sample, might otherwise affect the measurements SNR.

Attaching this system to a sample mounted in a cryostat for low temperature measurements, or combining it with a nitrogen-vacancy-center microscope, are just two possibilities for further development or improvement of such a galvo-galvo scanning system.

Chapter 4

Spin Wave Diffraction Phenomena

Parts of this Chapter have been summarized in Advanced Physics Research, "Hybridization-Induced Spin-Wave Transmission Stop Band within a 1D Diffraction Grating" [109].

The manipulation and control of spin waves is at the heart of the field of magnonics which has become a topic of increasing interest in recent years [8, 9, 43–45, 45–50, 110]. Understanding the manipulation of propagating spin waves is necessary for the fabrication of potential magnonic devices. Magnonic wave-guides [22, 111, 112], periodic structures [113, 114] as well as externally controlled anisotropy [112] have been used to control the propagation direction as well as the band gap of spin waves in ferro- or ferrimagnetic materials. To achieve these kinds of effects, one takes advantage of the wave nature of spin waves, which not only allows one to use wave variables such as wavelength, amplitude, and propagation direction as control parameters, but also allows one to enter a caustic realm, where it is possible to control the propagation direction of spin wave beams [22, 111, 115]. The caustic-like regime is easily accessible for in-plane magnetized magnetic thin films due to the anisotropic behavior of the dispersion relation for dipolar-dominated spin waves [111]. This anisotropy leads to DE ($\mathbf{k} \perp \mathbf{M}$) spin wave modes and Magneto-Static Backward Volume (BV) spin wave modes ($\mathbf{k} \| \mathbf{M}$) or a mixture of the two

modes, if the in-plane magnetisation has an arbitrary angle with respect to the two symmetry directions (cf. Section 2.3.1) [116]. It was already demonstrated that the direction of propagation of spin wave beams from a magnetic-stripe wave-guide into an extended film can be controlled by varying the external magnetic field [22, 112]. Furthermore, it was shown experimentally and theoretically that manipulating the propagation of spin waves can be achieved by patterning magnetic films [113, 117–119].

In this Chapter, we demonstrate the conversion of a plane spin wave into caustic-like beams in a 200 nm thick patterned Yittrium Iron Garnet (YIG) film, where the pattern consists of square shaped anti-dots forming a spin wave diffraction grating. This grating can diffract spin waves just after propagating through it, if the wavelength of the spin wave is smaller than the anti-dot size. On the other hand, if the spin wave wavelength is larger than the anti-dot size, the diffraction grating itself can act as a point-like spin wave source to emit caustic-like spin wave beams.

A spin wave propagation stop band through the grating is achieved by locally changing the effective magnetic field between the square shaped anti-dots. We experimentally observe the propagating spin waves using Time-Resolved Magneto Optical Kerr Microscopy (TR-MOKE), described in Section 3.1. The influence of the diffraction grating on the effective magnetic field, as well as on propagating spin waves, is investigated by micromagnetic simulations [120]. Furthermore, the dispersion relation for the DE and BV spin wave modes were calculated not only by the theory of Kalinikos and Slavin [61] but also by using the free Python based script TetraX. TetraX uses the propagating-wave dynamic-matrix approach in the framework of finite elements, as described elsewhere [77, 78].

Furthermore, we will present that the transmission stop band occurs due to the hybridization of two DE spin wave modes which leads to a reduced group velocity and with this to a shorter attenuation length (L_{att}), cf. Eq. (2.22). There was no hybridization and with this no transmission stop band observable for BV-like spin waves in our experiments. An anisotropic diffraction behavior for Forward Volume (FV)-like spin waves will be presented in the final part of this chapter.
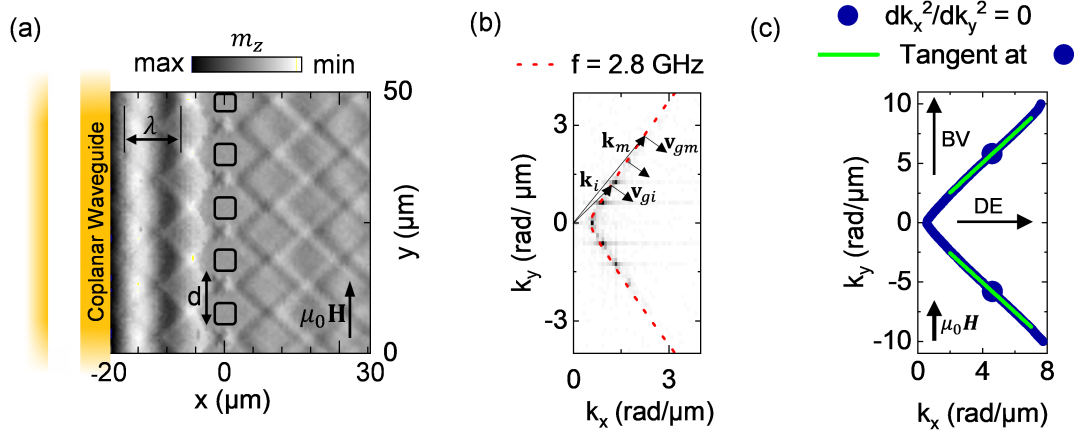
Figure 4.1: (a) TR-MOKE measurement of a plane spin wave propagating to a diffraction grating. The diffraction grating has lattice constant of $d = 10$ µm, indicated by the black squares. A bias magnetic field of 41 mT was applied along the y-axis at a rf-frequency of 2.8 GHz. Caustic-like spin wave beams are emitted from a point-like source at the diffraction grating in both, the positive and negative x-directions. (b) The two-dimensional FFT of the region behind the diffraction grating represents the emitted wave-vectors in both, x- and y-direction. The normal to the iso-frequency line (dashed red line) gives the group velocity for every corresponding wave-vector. (c) Calculated iso-frequency curve to demonstrate real caustic points (blue dots) with the corresponding tangent at these points (green solid lines).

4.1   Spin Wave Diffraction by Anti-Dot Gratings

Figure 4.1 (a) displays a sketch of the experimental arrangement, where the gray-scale corresponds to the z-component of the dynamic magnetization measured by TR-MOKE. Femtosecond laser pulses with a center-wavelength of 800 nm and a repetition rate of 80 MHz where phase locked to the frequency of the rf-current to achieve an image of the dynamic magnetization at a fixed rf-phase, as already described in detail in Section 3.1. Plane dipole-dominated spin waves are excited within a 200 nm thick YIG film by a rf-current which is driven through a CPW deposited on top of the YIG film, and schematically represented on the left-hand side of Fig. 4.1 (a). The CPW was patterned by photo-lithography and consisted of 5 nm Cr and 100 nm Au. The ground and the signal lines have a width of 5 µm and 10 µm, respectively. The distance between the signal and ground lines was 5 µm. Three different diffraction gratings were produced

by photo-lithography and Ar etching, corresponding to lattice constants of $d = 10$ µm, 20 µm and 30 µm. In each case, the antidot width was fixed to $d/2$. A bias magnetic field of $\mu_0\mathbf{H} = 41$ mT was applied along the y-direction (DE geometry) and the frequency of the rf-current was fixed to 2.8 GHz. The plane spin wave propagates through the lattice of square shaped antidots, indicated by the black squares in Fig. 4.1 (a).

For this condition, we observe a spin wave beam emission from the diffraction grating not only in the positive x-direction, but also in the negative x-direction, back towards the CPW. This can be seen by the diamond-shaped spin wave pattern which interferes with the plane spin wave on the left-hand side of the diffraction grating. The regions between any two neighboring antidots acts as a point-like spin wave source as the spin wave wavelength λ is greater than $d/2$. This area is a source of spherical wavelets due to Huygens principle. We do not observe a spherical wavelet but a rather beam-like shaped spin wave emission from the area between the anti-dots. This is due to the anisotropic behavior in the dispersion relation for dipolar-dominated spin waves in an in-plane magnetized thin film. The k-vector distribution in the x- (k_x) and y-direction (k_y) are extracted from the right-hand side of the diffraction grating by a two dimensional fast Fourier transformation (2D-FFT), as shown in Fig. 4.1 (b). A calculated dispersion iso-frequency curve (red dashed line) is shown overlaid on the 2D-FFT data. Every vector which connects the origin of the coordinate system with any point on the iso-frequency curve, represents a specific wave-vector $\mathbf{k}$. The direction of the group velocity $\mathbf{v}_\mathrm{g}$ for a specific wave-vector $\mathbf{k}$ is given by the normal to the iso-frequency curve at this point. A caustic beam is formed if different wave-vectors $\mathbf{k}$ have the same direction of the group velocity $\mathbf{v}_\mathrm{g}$, i.e. in regions where the iso-frequency curve has a linear-like slope, resulting in a divergence in the power flow [121]. A so-called caustic point occurs when $dk_x^2/dk_y^2 = 0$ [Fig. 4.1 (c)], which is beyond the $\mathbf{k}$-range which we present in Fig. 4.1 (b). Nevertheless, the slope of the iso-frequency curve in the $\mathbf{k}$-range which we observe is close to linear which means that there are enough wave-vectors $\mathbf{k}$ with a similar direction of the group velocity $\mathbf{v}_\mathrm{g}$ to form spin wave beams. As a result, we will refer to these spin wave beams as caustic-like spin waves.
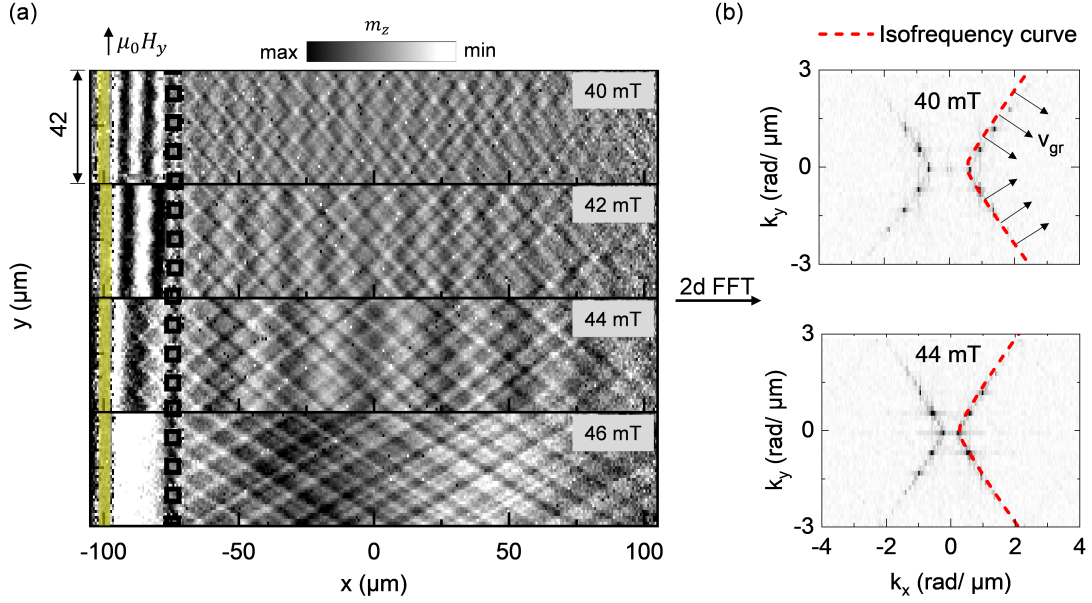
Figure 4.2: (a) TR-MOKE measurement of a plane spin wave propagating through a diffraction grating for different bias magnetic field values at a fixed rf-frequency of 2.8 GHz. (b) 2D-FFT data of the region on the right-hand side of the diffraction grating for two exemplary bias magnetic field values of 40 mT and 44 mT. Red dashed lines present the calculated iso-frequency lines. The wave-vector distribution in the x-direction (k_x) can be controlled by varying the bias magnetic field strength while k_y remains constant. This allows to control the direction of caustic-like spin wave beams by simply changing the bias magnetic field strength.

The absolute value of **k** and in-turn the wavelength λ can be tuned by varying the strength of the external magnetic field at a given rf-frequency. Figure 4.2 (a) demonstrates the effect of different bias magnetic fields on the caustic-like interference pattern. Increasing the bias magnetic field increases the wavelength (decreases the wave-vector) of the incoming plane spin waves on the left-hand side of the diffraction grating. The wave-vector distribution for the complex interference pattern on the right-hand side of the diffraction grating is affected by the wavelength of the plane spin wave as well. Fig. 4.2 (b) demonstrates again 2D-FFT data for the right-hand side of the diffraction grating for exemplary bias magnetic fields of 40 mT and 44 mT. Decreasing the wave-vector k_x for the incoming plane spin wave entails a decreasing k_x distribution for the

interference pattern on the right-hand side of the diffraction grating as well. The wave-vector distribution in the y-direction (k_y), on the other hand, is given by the dimensions of the diffraction grating in the y-direction and stays constant under varying external magnetic fields. This leads to the possibility to control the direction of the caustic-like spin wave beams simply by changing the strength of the bias magnetic field. Furthermore, the right-hand side of the diffraction grating in Fig. 4.2 (a) does not only show a complex diffraction pattern of caustic-like spin waves but contains the wavelength of the initial plane spin wave superimposed with the diffraction pattern. Dipolar dominated spin waves show a characteristic long range interaction. This allows the dipolar moments on the left-hand side of the diffraction grating to couple to the dipolar moments on the right-hand side of the diffraction grating and with this to conserve the initial wavelength of the plane spin wave.

4.2 Spin Wave Transmission Stop Band

Figure 4.3 (a) - (d) present the effect of the diffraction grating with $d = 10$ µm on a plane spin wave for different external magnetic field values. The spin wave transmission through the diffraction grating is highly suppressed for a certain magnetic field range. This can be seen in Fig. 4.3 (b) and (c) in which the spin wave amplitude on the right-hand side of the grating is close to or even zero. Furthermore, it can be seen that the formation of a caustic-like spin wave beam becomes less prominent for wavelengths shorter than $d/2$.

To gain further insight into the propagation of the spin waves between the antidots, we additionally measured the propagation through a diffraction grating with $d = 30$ µm. Fig. 4.3 (f) - (i) present the effect of an area between two antidots for similar external magnetic field values than in Fig. 4.3 (a) - (d). For several external magnetic field values, a waist-like shape of the spin wave propagation is observed between neighboring antidots. At $\mu_0\mathbf{H} = 33.0$ mT a strong attenuation of the spin wave occurs between the antidots resulting in a suppression of the spin wave transmission, shown in Fig. 4.3 (g).
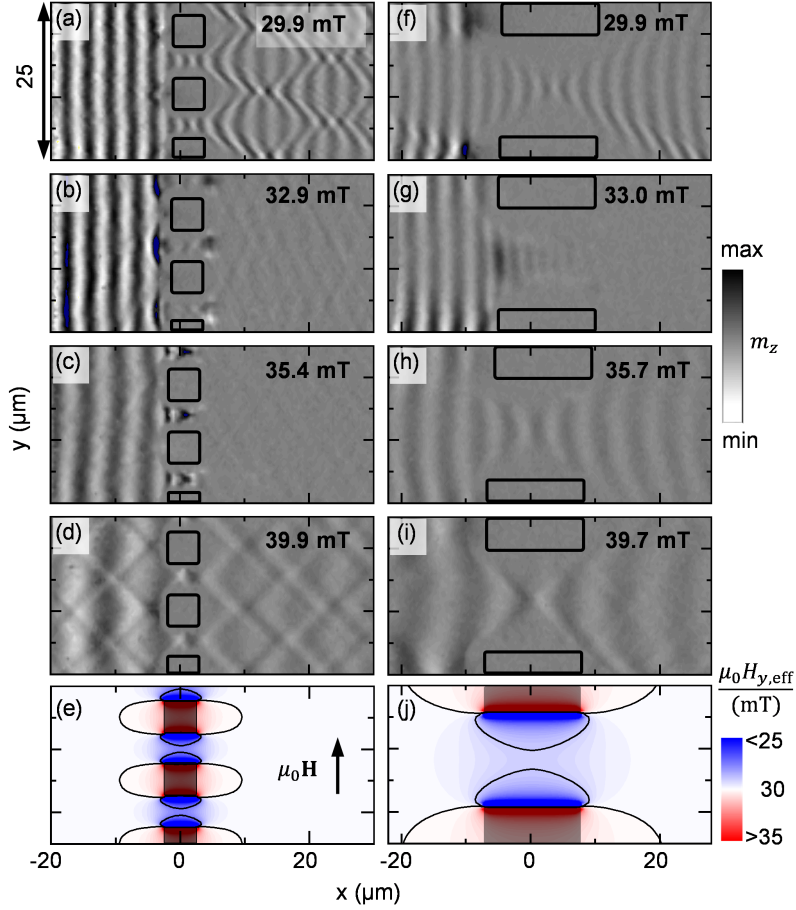
Figure 4.3: Two-dimensional TR-MOKE images for different external magnetic field values. (a) - (d) [(f) - (i)] demonstrate the effect of a diffraction grating with $d = 10$ µm [$d = 30$ µm] on a plane spin wave which is excited at the left-hand side of the diffraction grating. The spin wave propagation through the grating depends on both, the external magnetic field and the lattice constant of the diffraction grating. Micromagnetic simulations for the effective magnetic field are presented in (e) and (j) for the $d = 10$ µm and $d = 30$ µm grating, respectively.

The effective magnetic field for the $d = 10$ µm and $d = 30$ µm gratings were simulated for an external magnetic field of $\mu_0 \mathbf{H} = 30$ mT by micromagnetic simulations [120], presented in Fig. 4.3 (e), (j). The effective magnetic field between the antidots is clearly reduced due to magnetic surface charges at the edges of the antidots. Comparing the iso-field lines in Fig. 4.3 (e) and (j) (black solid lines) between the antidots, we can see that they have a similar waist-like shape compared to the spin waves between the antidots, measured by TR-MOKE.

In addition to the micromagnetic simulations for the effective magnetic field, we simulated spin wave propagation through a $d = 10$ µm diffraction grating [Figure 4.4 (a) - (c)]. Comparing the simulation [Fig. 4.4 (a) - (c)] with the experimentally observed data [Fig. 4.4 (d) - (f)] shows that they are in good agreement with each other only for the regime where we do not observe the propagation stop for spin waves. We did not observe a suppressed spin wave propagation through the diffraction grating by micromagnetic simulations, [Fig. 4.4 (b)]. A 1 µm wide strip line antenna was used to excite the spin waves in the simulation (indicated by the yellow line in Fig. 4.4 (a) - (c), whereas we used a CPW for the real experiment (ground line indicated by the yellow line in Fig. 4.4 (d) - (f). Another difference between simulation and experiment was the limitation for the discretization in the thickness direction of the YIG film. Due to limited computing power, we had to limit the number of cells in the thickness direction to four. As a consequence, perpendicular standing spin waves, for example, will not be considered due to this limitation which might explain the difference between the simulations and our experimental results. The dispersion relation of two or more spin wave modes can theoretically cross each other [61, 101, 122, 123]. A coupling between these spin wave modes may lead to a hybridization (depending on the symmetry) and consequently to an anti-crossing in the dispersion relation [101, 124, 125]. As a result, the slope of the dispersion in the vicinity of the anticrossing approaches zero and in turn the group velocity as well, cf. Eq. (2.19). The gap of the anti-crossing thereby defines the coupling strength between the spin wave modes.

Figure 4.5 presents the calculated dispersion relation for both DE and BV spin waves.
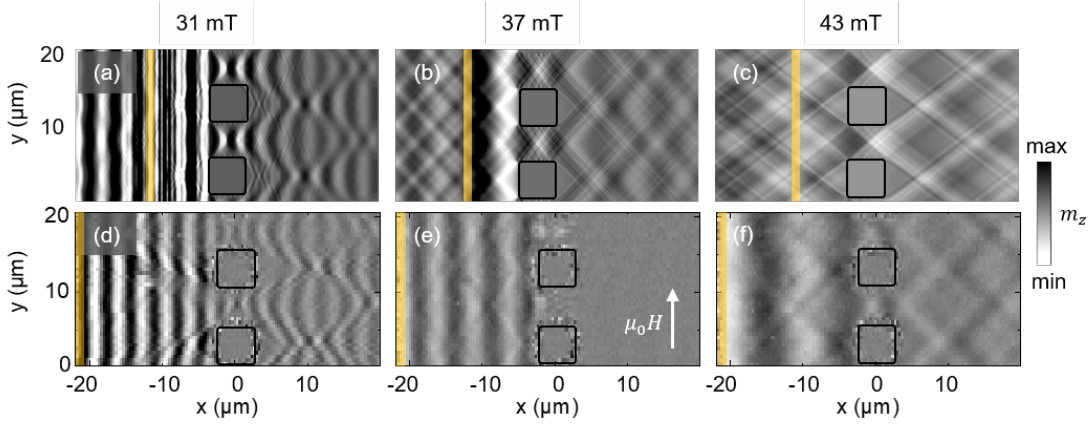
Figure 4.4: (a) - (c) present micromagnetic simulations of propagating spin waves through a diffraction grating with $d = 10$ µm using MuMax3 software. A 1 µm strip line antenna, indicated by the yellow lines, was used as a excitation source for the spin waves. There is no transmission stop observable for different external magnetic field values in the DE geometry for the simulation. The experimental TR-MOKE measurements, on the other hand, demonstrate the existence of such a stop band, presented in (d) - (f). The spin waves were excited by a CPW where the right ground line is indicated by the yellow lines.

The dispersion relations were calculated for $\mu_0 \mathbf{H} = 31$ mT, where the 200 nm thickness of the YIG film and with this perpendicular standing spin waves (PSSW) were accounted for. PSSW's are spin waves which are confined within the thickness of the magnetic film, as depicted in the top panel of Fig. 4.5 (a). Fig. 4.5 (a) presents the dispersion relation using the zeroth order perturbation theory from Kalinikos and Slavin for $n = 0$ and $n = 1$ DE (solid lines) and BV (dashed lines) modes [61]. A first theoretical mode crossing for the $n = 0$ and $n = 1$ DE spin wave modes can be observed at 2.8 GHz and a wave-vector value of about 1.4 rad µm^{-1}, whereas there is no crossing for BV modes. Using the TetraX script allows us to consider the coupling between the PSSW as well, which can be seen by the anti-crossing of the DE-like spin wave modes in Fig. 4.5 (b). As already mentioned, this anti-crossing results from a hybridization of these two modes and leads to an attenuation length within the coupling regime due to the flattening of the dispersion relation in the anti-crossing regime (cf. Section 2.4.3). Comparing the analytical dispersion relation from Kalinikos and Slavin [solid colored lines in (b)] with
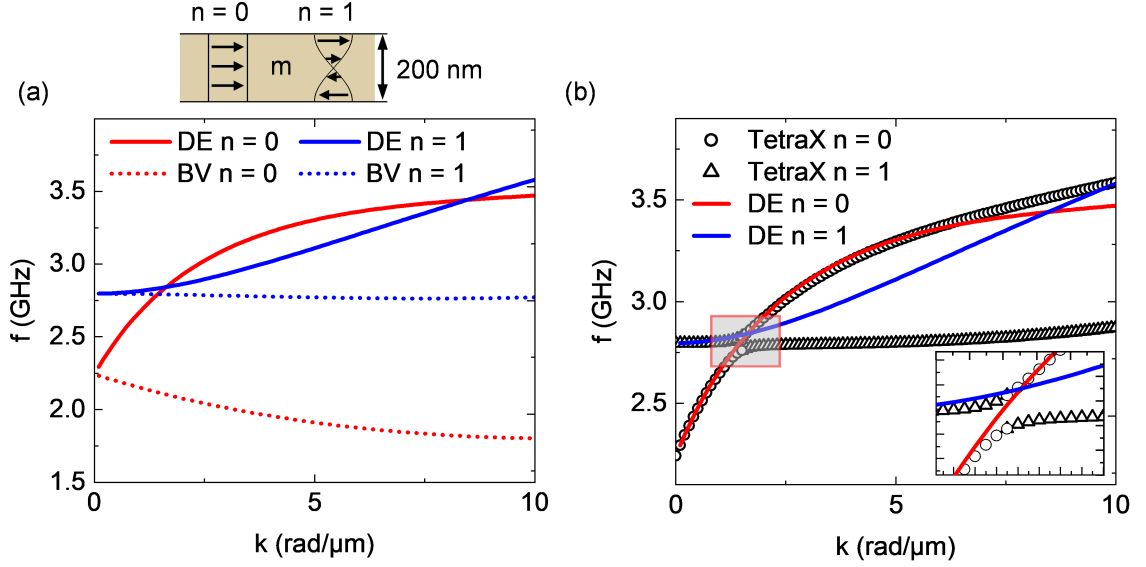
Figure 4.5: (a) Calculated spin wave dispersion relation for Damon-Eshbach (DE) and Backward Volume (BV) geometry accounting for the thickness of the YIG film using zeroth-order perturbation theory from Kalinikos and Slavin (KS) [116]. A crossing of the PSSW $n = 0$ and $n = 1$ DE modes is observed at a frequency of 2.8 GHz and a k-value of about 1.4 rad μm^{-1} whereas there is no crossing for the BV spin wave modes. The $n = 0$ and $n = 1$ PSSW modes are depicted in the top panel of (a). (b) Calculated dispersion relation for DE spin waves using the TetraX script in comparison with the KS dispersion. It can be seen that the KS theory does not give the suitable solution for the 200 nm thick YIG film. Inset shows a zoom in to the hybridization area for the DE $n = 0$ and $n = 1$ mode. An external magnetic field of 31 mT was considered for all dispersions.

the numerical dispersion relation observed by TetraX [black spheres in (b)] demonstrates that the KS theory does not give a suitable solution for the dispersion for a 200 nm thick YIG film. The inset in Fig. 4.5 (b) shows a zoom into the hybridization area for the $n = 0$ and $n = 1$ mode for illustrating the anti-crossing.

4.3 Hybridization Induced Spin Wave Attenuation

To observe a potential hybridization for the two DE spin wave modes, we measured the spin wave propagation in the x-direction as a function of the external magnetic field

in the plane YIG film, far away from any diffraction grating. As shown in Fig. 4.6 (a) there is an external magnetic field range around 31 mT in which the spin wave propagation is highly damped. We obtained the absolute value of the wave-vector **k** from these measurements by fitting a sinusoidal function to the propagating spin waves in the x-direction for every applied external magnetic field value. With this, we extracted the spin wave wavelength λ for the respective magnetic field value and calculated the absolute value of the wave-vector by the relation $|\mathbf{k}| = \frac{2\pi}{\lambda}$. These **k**-values are indicated by the black spheres shown in Fig. 4.6 (b). Comparing this experimental data with the calculated dispersion relation for the $n = 0$ and $n = 1$ DE mode in Fig. 4.6 (b) shows that the experimentally observed avoided crossing, measured by TR-MOKE, is in good agreement with the dispersion relation calculated with TetraX, shown by the red spheres in Fig. 4.6 (b). This is a strong indicator that the high attenuation around 31 mT [Fig. 4.6 (a)] occurs from the coupling and hybridization of the two DE spin wave modes. It furthermore confirms, that the spin wave transmission stop band at the diffraction grating occurs as a result of the reduced effective field between the anti-dots. This shifts the dispersion relation to the hybridization area for a corresponding external magnetic field range and with this to a high attenuation regime.

4.4 Diffraction of BV and FV spin waves

Figure 4.7 (a) - (c) demonstrate the effect of a diffraction grating with a lattice constant of $d = 30$ µm on a plane spin wave, excited in the BV-geometry. Like for the DE-like excited spin waves, there is a complex diffraction pattern on the right-hand side of the diffraction grating. The diffraction pattern is dominated by caustic-like spin wave beams as the spin wave wavelength approaches a value on the order of $d/2$, see Fig. 4.7 (a), (b). Not only can a diffraction pattern on the right-hand side of the diffraction grating be observed, but also standing spin waves in the y-direction, between the anti-dots. The area between the anti-dots therefore acts as a wave-guide which confines the spin wave in the y-direction. This confinement leads to the formation of standing spin waves between
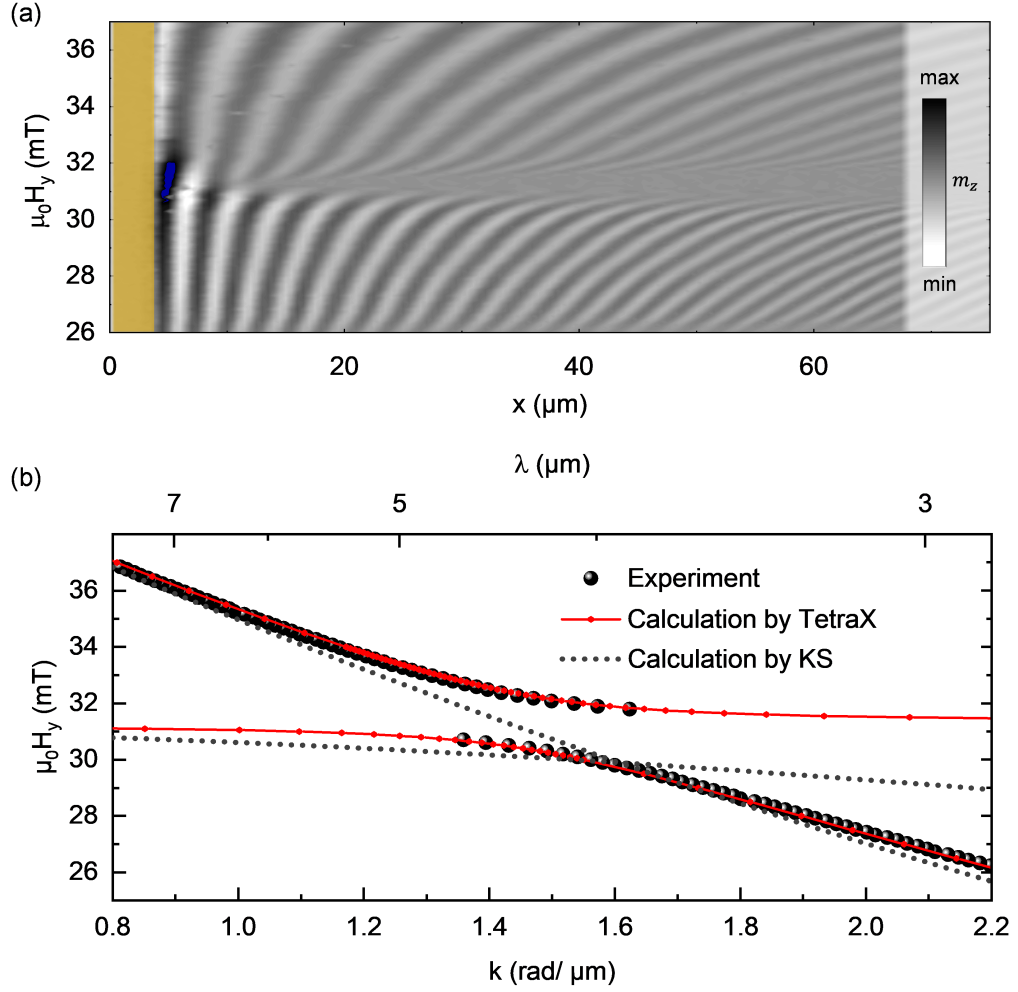
Figure 4.6: (a) Spin wave propagation as a function of the external magnetic field. An area with high attenuation is observed around 31 mT. (b) Black spheres show the extracted k-values from TR-MOKE measurements presented in (a). The dispersion relation calculated using TetraX (red symbol-line) is in good agreement with the experimental data, whereas the calculation using the zeroth order perturbation theory from Kalinikos and Slavin (KS) does not give the proper solution in the vicinity of the hybridization.

the anti-dots, as already presented for magnetic wave-guides in a previous work [101]. There was no transmission stop band observable for BV spin waves in our experiments. Measuring the spin wave propagation as a function of the external magnetic field, far away from any diffraction grating, shows that there is no magnetic field range which

shows an enhanced attenuation, see Fig. 4.7 (d). This is also consistent with the theory as we do not see any mode crossing in the dispersion relation for the $n = 0$ and $n = 1$ BV modes [Fig. 4.5 (a)]. Furthermore, the effective magnetic field between the anti-dots is barely reduced as the external magnetic field points perpendicular to the diffraction grating for the BV geometry, presented in Fig. 4.7 (e).
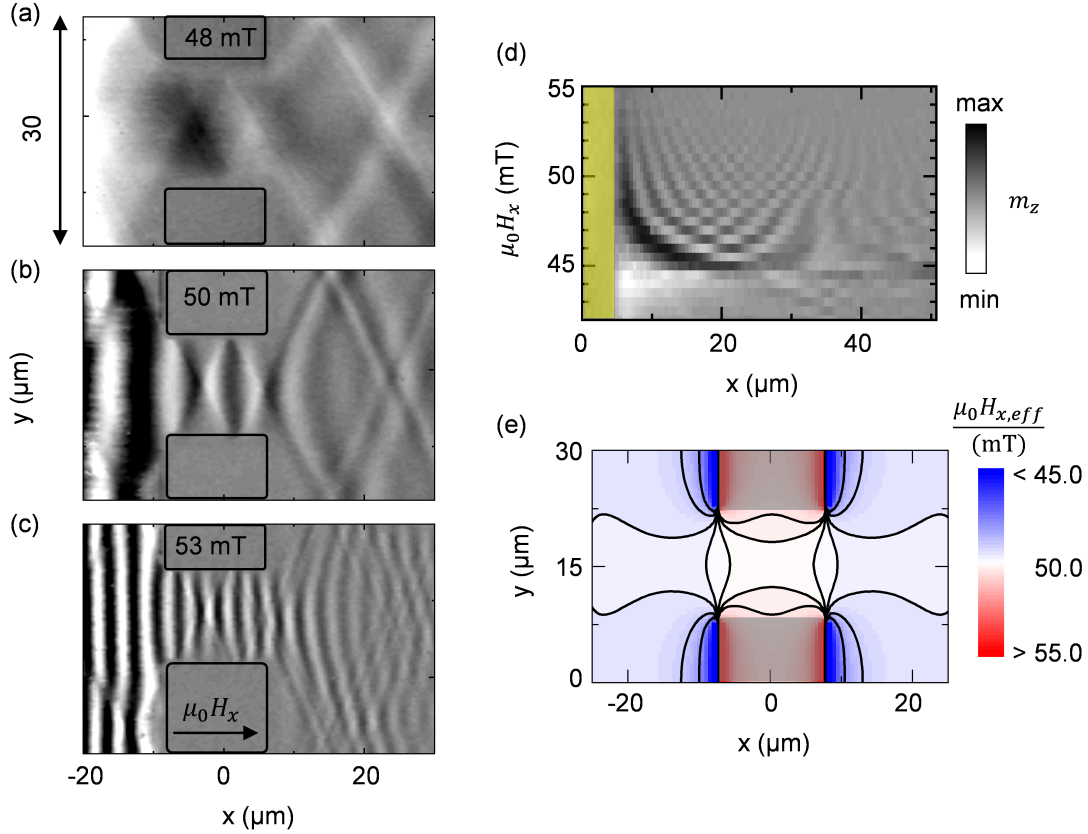
Figure 4.7: Two-dimensional TR-MOKE images for different external magnetic field values at a given rf-frequency of 2.8 GHz. (a) - (c) demonstrate the effect of a diffraction grating with $d = 30$ µm (indicated by the black squares) on a plane BV wave which is excited at the left-hand side ($x < 0$) of the diffraction grating. (d) Spin wave propagation as a function of the external magnetic field. There is no high attenuation area for BV observable. Micromagnetic simulations for the effective magnetic field are presented in (e).

To overcome the anisotropic dispersion for spin waves, we performed spin wave exci-
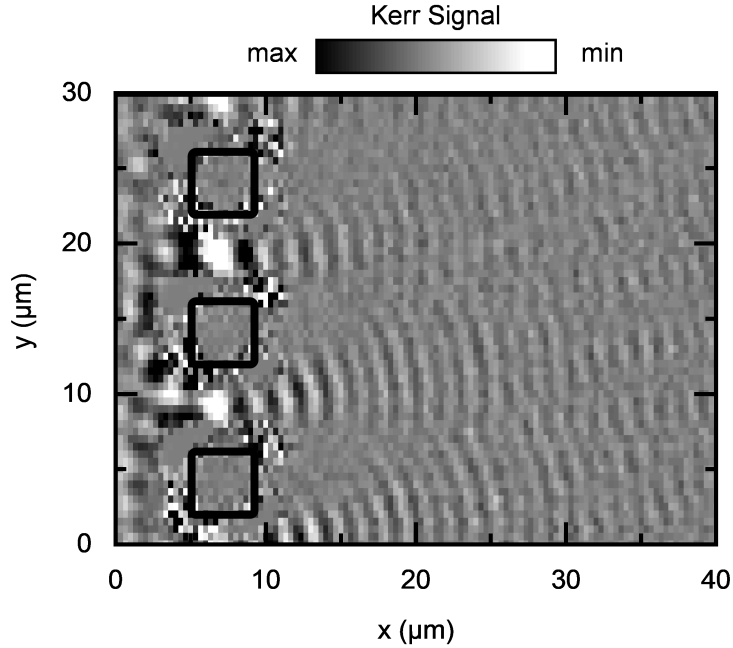
Figure 4.8: Two-dimensional TR-MOKE image of FV-like spin wave diffraction pattern at an external magnetic field of 286 mT pointing along the z-direction at a rf-frequency of 4.0 GHz. A spherical diffraction pattern is observed due to the isotropic spin wave behavior of FV-like spin waves.

tation in the FV-geometry by applying the external magnetic field along the z-direction (out of the sample plane). Figure 4.8 presents a two dimensional TR-MOKE measurement for a FV-like spin wave propagating through a diffraction grating with a lattice constant of $d = 10$ µm. We observe a clear difference, concerning the diffraction pattern, between the in-plane (DE and BV) and out-of-plane (FV) geometries. A spherical wave emission on the right-hand side of the diffraction grating can be seen which strongly indicates the isotropic propagation behavior of the FV-like spin waves. The SNR of the FV-like measurements is much smaller compared to the measurements for DE and BV-like spin waves, as polar MOKE can, in general, be considered to be stronger compared to the longitudinal or transversal MOKE symmetries [126] (cf. Section 2.7). Furthermore, the FV-like spin waves seem to be strongly reflected at the diffraction grating, which can be seen by the strong spin wave intensity on the left-hand side of the diffraction grating

in Fig. 4.8.

In conclusion, we demonstrated the behavior for plane dipolar-dominated spin waves propagating through a spin wave diffraction grating. The regions between the anti-dots act like point-like spin wave sources if the wavelength of the spin wave becomes equal to or larger than half the lattice constant d. This can be seen by the emission of caustic-like spin wave beams in both the positive and negative x-directions. Diffraction effects are only observable on the right-hand side of the diffraction grating for spin waves with a wavelength smaller than half the lattice constant d. In addition to the diffraction phenomena, we observed a spin wave transmission stop band through the grating for a certain external magnetic field range. This was shown for two different lattice constants ($d = 10$ µm and $d = 30$ µm) whereas the magnetic field range for the stop bands was slightly different for the two gratings. Hybridization of two DE spin wave modes, in combination with the reduced effective magnetic field between the anti-dots were found to lead to this effect. We demonstrated that the hybridization of two spin wave modes can lead to an enhanced attenuation, and by locally changing the effective magnetic field even to a stop-band condition for propagating spin waves. Furthermore, we compared the calculated dispersion relation using the free Python package TetraX as well as micromagnetic simulations of the effective magnetic field with our experimental data and found that they are in a good agreement with each other. We also demonstrated the limitation for the zeroth-order perturbation theory from Kalinikos and Slavin. Comparing this thin-film approximation with the experimentally observed data shows that they do not coincide with each other as we are not in the thin-film limit. Caustic like spin wave beams have been observed due to the anisotropic dispersion relation for DE and BV spin wave modes. FV-like spin waves have been excited to overcome the anisotropic behavior for propagating spin waves. We demonstrated that the diffraction pattern for FV-like spin waves shows a spherical wavelet behind the diffraction grating due to the isotropic propagation behavior. That demonstrates once again that the diffraction grating can act as a point like spin wave source.

Chapter 5

Spin Wave Interaction with Normal Metals (NM)

The interaction of propagating spin waves with normal metals (NM) in proximity to ferro- or ferrimagnetic materials has become a topic of high interest, ever since it was realized that magnonic devices could be used for a variety of information processing and storage applications [9]. Low-damping materials, such as Py, CoFeB and the magnetic insulator YIG, are potential materials for enabling such magnonic devices. A metallic contact, e.g. made from Platinum (Pt), attached to the magnetic layer will be necessary to send, as well as to read out, the "bits" of information carried by the spin waves. For this, an in-depth knowledge and understanding of the interaction and manipulation of spin waves with and through NMs in proximity to magnetic layers is of current and important interest.

The interaction of spin waves through ferrite slabs in proximity to NMs was already first investigated more than 50 years ago [127–129]. Within the last decades, with the rise in the demand to find low-energy alternatives to pure electronics, the interest in the interaction of spin waves with metallized magnetic films expanded rapidly, aided by the variety of modern characterization methods, as well as high quality thin film YIG, currently available [69, 73, 114, 130–143].

In 1970, Seshadri first revealed that the wave-number as well as the group velocity of DE-like spin waves becomes non-reciprocal in a ferrite slab coated with a NM [129]. About 45 years later, a theory to describe the non-reciprocal dispersion of spin waves propagating in the DE geometry within a thin ferromagnetic film, covered with a finite conductive metal, was presented [134]. The thickness of the NM, in this theoretical work, was considered to be much larger than the skin-depth δ_s (Eq. (5.1)) of the NM

$$\delta_\text{s} = \sqrt{\frac{1}{\pi f \mu_0 \sigma}} = \sqrt{\frac{\rho}{\pi f \mu_0}}, \qquad (5.1)$$

with f the frequency in GHz, $\mu_0 = 1.256 \cdot 10^{-6}$ N A^{-2} the vacuum permeability and σ or ρ the conductivity or resistivity of the NM, respectively. On the other hand, Kanazwa et al., demonstrated the effect on the dispersion of DE spin waves with only 100 nm thick Cu stripes on top of a 110 µm thick YIG film [136]. Moreover, they demonstrated a suppression of the spin wave transmission intensity due to the presence of the Cu stripes. As a result, the use of periodic metallic structures placed on top of a magnetic insulator, became promising architectures for manipulating the direction of propagation as well as the amplitude of spin waves, which has since been demonstrated in various works [135,137,141,144]. Different NMs on top of a YIG film have been used to enhance the damping of the spin wave to suppress back reflection from the edges of the YIG film [138,141]. Furthermore, it was presented that absorption for FV spin waves, even for thin Au layers in the range of 1 nm - 100 nm, on top of a d = 18.4 µm thick YIG film, was influenced by strong hybridization of two spin wave modes [138]. Spin-pumping induced damping α_sp [Eq. (5.2)] was also considered but neglected for this work, as the YIG film was rather thick and the contribution of $\alpha_\text{sp} = 6.87 \cdot 10^{-7}$ was much smaller than the intrinsic damping, which is in the order of 10^{-4} [130].

$$\alpha_\text{sp} = \frac{g \mu_B}{4 \pi M_\text{s}} g_{\uparrow\downarrow} \frac{1}{d_{YIG}} \qquad (5.2)$$

A spin mixing conductance of $g_{\uparrow\downarrow} = 1.2 \cdot 10^{14}$ cm^{-2} and a saturation magnetization of $M_\text{s} = 140$ kA/m was used for this calculation [130], where g and μ_B are the Landé

factor and the Bohr magneton, respectively. A systematic investigation of the spin mixing conductance of various metals can be found in Ref. [75]. Härtinger et al., on the other hand, demonstrated that a NM layer does not necessarily act as a perfect spin sink insofar that one has to consider an effective spin mixing conductance $g_{\text{eff}}^{\uparrow\downarrow}$ (cf. Eq. (2.34) [145]). The effective spin mixing conductance takes into account a partial back-flow of the spin current, which leads to a reduced spin mixing conductance. However, the $g_{\text{eff}}^{\uparrow\downarrow}$ for a YIG/Au interface was found to be $g_{\text{eff}}^{\uparrow\downarrow} = 6 \cdot 10^{14}$ cm^{-1} which is a higher value compared to the spin mixing conductance (not the effective) [130]. The difference for this was explained by Härtinger et al. to be due to the in situ growth of the metallic layers on the YIG, compared to the ex situ fabrication of the metallic layers reported in Ref. [130]. Furthermore, Härtinger et al., observed an effective spin mixing conductance at the YIG/Pt interface of $g_{\text{eff}}^{\uparrow\downarrow} = 9.7 \cdot 10^{14}$ cm^{-1} which leads to a higher damping contribution for Pt compared to Au, concerning Eq. (5.2).

Direct imaging of the damping of spin waves underneath metals has been demonstrated using NV-center microscopy [69]. In that work, the authors argued that the enhanced damping due to the NM on top of a 235 nm YIG film was caused by the formation of eddy-currents, rather than by the effect of spin-pumping.

Overall, it was shown that the propagation of spin waves in proximity to NMs can be affected by a variety of effects like spin-pumping, eddy current-induced damping, and NM induced non-reciprocity of DE-like spin waves. However, up until now, it has not been revealed how single metallic structures, with thicknesses much smaller than the skin depth of the NM, placed in proximity to magnetic insulators can be used to manipulate the direction, phase, as well as the amplitude of propagating spin waves.

In this chapter, we investigate the propagation behavior of DE-like spin waves in proximity to a variety of NMs (e.g. Au, Cu, Pt, Ti and Cr) as a function of the NM thickness. In each case, we restrict the NM thickness to less than the skin-depth of the NM. We demonstrate an enhanced damping behavior of spin waves propagating underneath a NM with a thickness of about half the thickness of the YIG film. A non-reciprocal dispersion relation for YIG, induced by NMs on the order of a tenth of the

YIG thickness, is presented by direct imaging propagating spin waves through the NM using TR-MOKE. The coupling strengths within a hybridization regime for two DE-like spin wave modes are enhanced by the NM, which will be presented for the NMs Au, Pt and Cu. Furthermore, by taking advantage of the manipulation of the dispersion by a NM, we demonstrate an optic-like spin wave manipulation not only for the amplitude and phase of the spin wave, but also for the direction of a spin wave diffraction-like pattern.

5.1   Bi-Layer NM-Induced Spin Wave Damping

Figure 5.1 demonstrates the effect of rectangular-shaped structures prepared from 5 nm Cr/ 100 nm Au in proximity to a 200 nm underlayer YIG film. The NM bilayer structures where deposited by photo-lithography and subsequent electron beam evaporation of the NMs. Argon etching for cleaning the YIG surface after the developing process in the course of the photo-lithography was done for 30 s before depositing the Cr/ Au on top. The NM rectangles were designed with different widths in the y-direction (20, 40, 60 µm) but with a fixed length in the x-direction (10 µm).

The attenuation of the spin wave arising from the interaction with the NM for different bias magnetic field values can be seen in Fig. 5.1 (a) - (e). Changing the bias magnetic field, and in turn, the spin wave wavelength seems to influence the spin wave damping underneath the metal. Analyzing the spin wave amplitude before and after the first Au stripe for the data presented in Fig. 5.1 (a) - (d) indicates that the damping effect induced by the NM stripes decreases with increasing spin wave wavelength. Not only the spin wave amplitude but also the phase of the spin wave seems to be affected by the metallic structure. Fig. 5.1 (f) represents an exemplary line plot along the x-direction at a given y-position, indicated by the green dashed line in Fig. 5.1 (b). The black dashed rectangle in Fig. 5.1 (f) marks the area behind the first metal stripe (x > 40 µm). Comparing the damped sinusoidal fit for this area (red solid line) with the extrapolated fit function (black solid line) from the area before the first NM
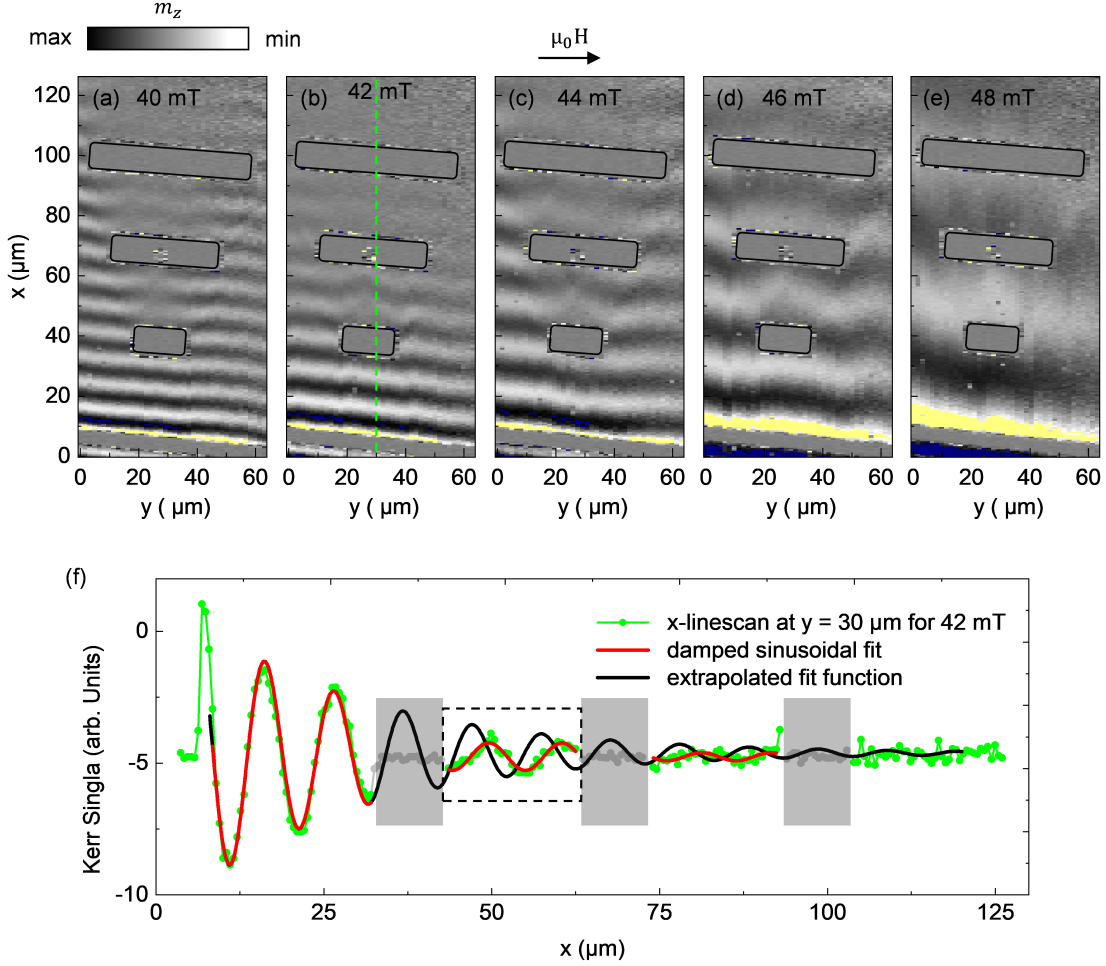
Figure 5.1: Two-dimensional TR-MOKE images for different external magnetic field values at a given rf frequency of 2.8 GHz. (a) to (e) demonstrate the effect of 5 nm Cr/ 100 nm Au rectangles (indicated by the black rectangles), deposited on top of the 200 nm YIG film. The DE-like spin waves get not only attenuated while propagating underneath the metal layers but seem to undergo a phase shift as well. (f) demonstrates exemplary an extracted x-line at y = 30 μm from (b). The phase shift as well as the enhanced damping is demonstrated by comparing the second damped sinusoidal fit line with the extrapolated fit function in the area indicated by the black dashed rectangle in (f). The NM rectangles are indicated by the grey areas in (f).

stripe (x < 30 µm), we find an attenuation effect induced by the NM on the spin wave. Moreover, a phase shift of the transmitted spin wave, with respect to the initial wave, is observed when comparing the relative phase between the fit functions.

It was already claimed that strong spin wave damping in metallized magnetic insulators can be caused by eddy-currents, induced by the spin waves oscillating magnetic stray field underneath the NM [69]. Eddy-current-induced damping can be described by an effective magnetic damping $\alpha = \alpha_{\mathrm{G}} + \alpha_{\mathrm{ed}}$, where α_{G} is the well-known intrinsic Gilbert damping parameter and α_{ed} the contribution by the eddy-current-induced damping. For NM layers with a thickness much smaller than the skin-depth of the metal, the eddy-current-induced damping is given by Eq. (5.3) [69]

$$\alpha_{\mathrm{ed}} = \gamma \cdot \mu_0^2 \cdot g(k)^2 \cdot M_{\mathrm{s}} \cdot h \cdot t \cdot \frac{1}{\rho} \cdot \frac{(1+\eta)^2}{4(1+\eta^2)}, \tag{5.3}$$

where γ is the gyromagnetic ratio, M_{s} is the saturation magnetization, t the metal film thickness, h the YIG film thickness, ρ the resistance of the metal, and η describes the ellipticity of the spin wave amplitude. $g(k) = (1 - e^{-kt})(1 - e^{-kh})/(k^2 th)$ accounts for the averaging of the eddy-current and stray-fields over the thickness of the YIG-film and the NM. To investigate the effect of the eddy current-induced damping, we first measured the sheet resistance for a 20 nm thick Au on top of a 200 nm thick YIG film. We performed the resistance measurements using a four-point measurement principle on four different Au structures. A resistance of $\rho = (3.9 \pm 0.2) \cdot 10^{-8}$ Ω m was observed which is comparable to the literature value of $\rho = 2.4 \cdot 10^{-8}$ Ω m. Figure 5.2 presents the calculated eddy-current induced damping α_{ed} as a function of the spin wave wavelength or wave-vector, for different metal thicknesses t, using a M_{s} of 140 kA/m. It can be seen that the damping decreases with increasing wave-vector **k** or decreasing wavelength λ, respectively. However, the experimentally observed behavior of the spin wave damping, presented in Fig. 5.1, does not coincide with the calculated eddy-current induced damping shown in Fig. 5.2.

Eddy currents may not only be induced by the oscillating magnetic stray field of the

spin waves but also by the rf-electromagnetic field, coming from the CPW. NMs can be used for shielding electromagnetic waves. As a consequence, the metallic layers on top of the YIG film may also interact with the rf-electromagnetic field, emitted by the CPW. Such an rf-field can induce eddy-currents in the NM only if the metal thickness is close to, or larger than the skin depth of the metal. Otherwise, the metal will be transparent for the rf-field.

To ensure that we can assume the thickness of the metallic layers to be much thinner than the skin depth δ_s for various NMs, we calculated the skin depth as a function of the frequency using Eq. (5.1). The results of the calculations are presented in Figure 5.3. A thickness of 105 nm, which was the metal thickness used for the experiment shown in Fig. 5.1, is indicated by the horizontal black dashed line. We use literature values for the resistance to calculate the skin depth for different NMs [colored solid lines in Fig.5.3]. The different NMs will be investigated in the following sections. The red dashed line presents the skin depth for the measured resistivity of a 20 nm Au on top of the 200 nm YIG film. It can be seen that the thickness of the metallic layers, investigated in this work, is far below the calculated skin depth for the various NMs. As a consequence, we assume that the mechanism for the enhanced damping can not only be influenced by eddy-currents but has to have a different or an additional origin.

The spin-pumping-induced damping of a 200 nm thick YIG film in proximity to a Au layer, calculated using Eq. (5.2) with the effective spin mixing conductance observed from [145] ($g_\text{eff}^{\uparrow\downarrow} = 6 \cdot 10^{14}$ cm^{-1}), results in an additional damping contribution of $\alpha_\text{sp} = 3.16 \cdot 10^{-4}$, which is on the order of magnitude for the intrinsic damping of thin YIG ($7 \cdot 10^{-4}$) [145] and may account for the enhanced attenuation, observed in Fig. 5.1.

To further investigate the effect of the NM on the propagating spin waves within the YIG film, we performed additional experiments. As shown in Fig. 5.1, the spin wave amplitude can not be observed directly through the 105 nm thick NM stripes by the TR-MOKE measurement. To observe propagating spin waves through the NM layer, we fabricated thinner NM structures of various thicknesses. Furthermore, to investigate the effect of different NMs on the spin wave propagation, we fabricated structures not
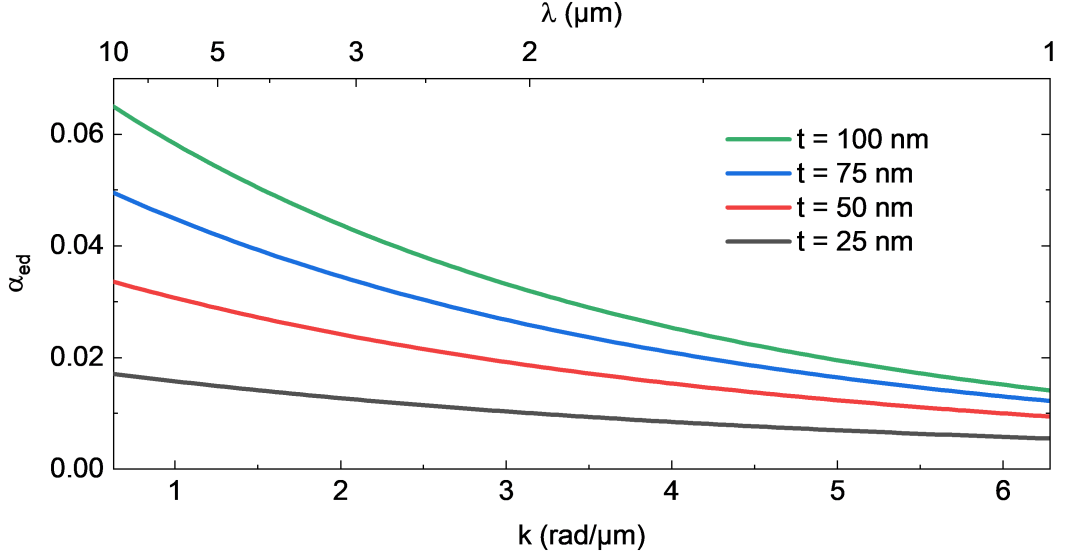
Figure 5.2: Calculated eddy-current induced damping in a 200 nm YIG film with $M_s = 140$ kA/m for different thicknesses t of the metallic layer, using Eq. (5.3). The influence on the damping induced by eddy-currents decreases with an increasing wave-vector **k**. A larger NM thickness, on the other hand, enhances the eddy-current induced damping.

only made of Au but also made of Cu and Pt. Pt was chosen to examine the effect of spin-pumping and the magnetic proximity effect (MPE) on the damping behavior [73, 132, 145–147].

5.2 NM-Induced Spin Wave Manipulation

The previous section presented a damping effect, as well as a phase shift, of spin waves propagating in metallized YIG. However, the attenuation of a spin wave can be caused by various other effects. Reflection, as well as absorption are two further possibilities. To investigate if the additional damping is induced by the transition from pure YIG to YIG/NM (reflection), or if the effect scales with the length of the NM and is therefore induced by absorption, we fabricated NM structures with different dimensions in the direction of the spin wave propagation.

Figure 5.4 (a) presents the effect of 5 nm Ti/ 50 nm Au with various x-dimensions
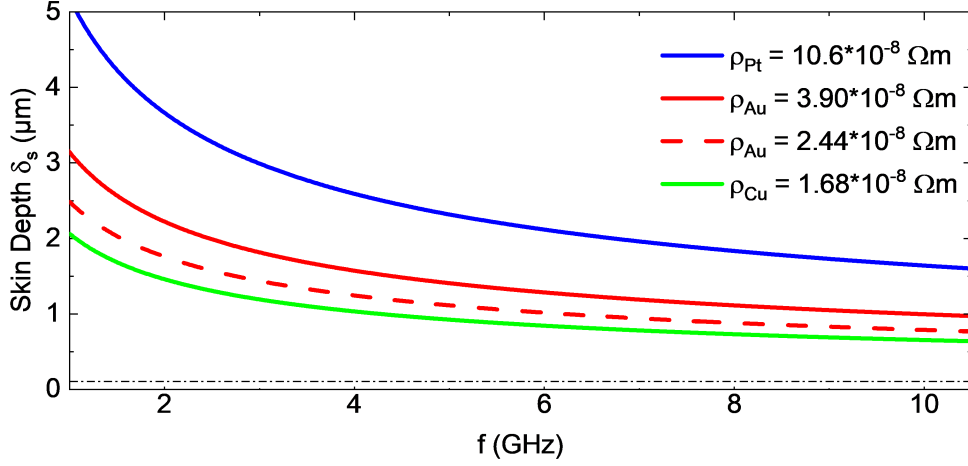
Figure 5.3: Calculated skin depth δ_s as a function of frequency for NMs investigated in this work. The thickness for the metallic layers used in our experiments are far below the skin depth for normal metals. The red dashed line indicates the skin depth for the experimentally obtained resistivity for a 20 nm Au layer on top of the 200 nm thick YIG film. Other resistivity values are taken from literature.

on a DE-like spin wave, propagating underneath the NM. The buffer layer was changed from Cr to Ti to reduce the potential effect of spin-pumping into the buffer layer [87]. The length of the metallic structures (x-dimension) was chosen to be 10 µm, 20 µm, and 30 µm. Again, Ar etching before depositing the NM on top of the YIG was applied for 30 seconds. Fig. 5.4 (a) demonstrates that there is indeed an area behind the metallic structures where the spin wave amplitude is attenuated, and this attenuation also appears to depend on the length of the NM. Furthermore, the area of dampened amplitude, or attenuation seems not to point in the propagation direction of the spin waves (direction of the **k**-vector). A possible reason for that might be that the bias magnetic field of 38 mT was slightly misaligned with respect to the y-axis, and as a consequence to the DE-like excitation. Comparing the attenuation of the 105 nm thick, 10 µm long metal stripe shown in Fig. 5.1 demonstrates the higher impact on the attenuation with respect to the 55 nm thick, 10 µm long stripe, shown in Fig. 5.4 (a). A phase shift of the spin waves can be seen especially for the 20 µm and 30 µm long metal structures which can, such as for any other wave phenomena, cause interference effects. Such interference

effects can cause constructive but also destructive interference, where the latter would lead to a further reduced spin wave amplitude.

Even thinner metallic structures are presented in Fig. 5.4 (b). Metallic rectangles of 20 nm Au, 20 nm Au/ 10 nm Pt, and 10 nm Pt have been deposited on top of the 200 nm YIG film again by photo-lithography. There was a 5 nm Ti buffer layer underneath all the NM structures. Ar etching was done for 30 seconds to clean the surface of the YIG film before depositing the metallic layers. For these structures, the film thickness of the metallic layers is thin enough to observe the spin wave even through the metal by TR-MOKE measurement. The 20 nm Au structure [left structure in Fig. 5.4 (b)] shows a rather small effect on the spin wave damping but seems to have a phase shift just for the metallized area. The phase shift becomes less prominent for the 20 nm Au/ 10 nm Pt, as well as for the 10 nm Pt structures. None of these structures exhibit a strong enhancement of spin wave damping. As already mentioned, spin-pumping from the YIG into the NM was assumed to contribute to an effective damping. The 10 nm thickness of the Pt layer should be enough to demonstrate an effect of spin-pumping as Sun et al. demonstrated a saturation in the damping enhancement for YIG, covered with Pt layers thicker than 3 nm [132]. The experimentally obtained spin mixing conductance for a 10 nm Pt layer on top of a 4.5 µm YIG film was estimated to be $g_{(YIG/Pt)}^{\uparrow\downarrow} = 1.3 \cdot 10^{14} \text{cm}^{-1}$ [133]. Inserting this parameter in Eq. (5.2) leads to a damping contribution, induced by spin-pumping, of $\alpha_{\text{sp}} = 6.92 \cdot 10^{-5}$. On the other hand, an effective spin mixing conductance of $g_{\text{eff}}^{\uparrow\downarrow} = 9.7 \cdot 10^{14} \text{ cm}^{-1}$ was observed for the interface between 25 nm YIG/ 7 nm Pt [145]. Considering this parameter in Eq. (5.2) leads to a damping contribution of $\alpha_{\text{sp}} = 5.11 \cdot 10^{-4}$, which is in the same order of magnitude as the intrinsic damping for pure YIG. As a result, we should observe an effect on the spin wave damping if the damping is caused by spin-pumping.

As there is no apparent attenuation for the spin wave propagating underneath the Pt area observable, we assume that the effect of spin-pumping on the damping is negligible for our experiments. Eddy-current induced damping can not be excluded completely as we do see a damping effect concerning the thickness of the NM which coincides with Eq.
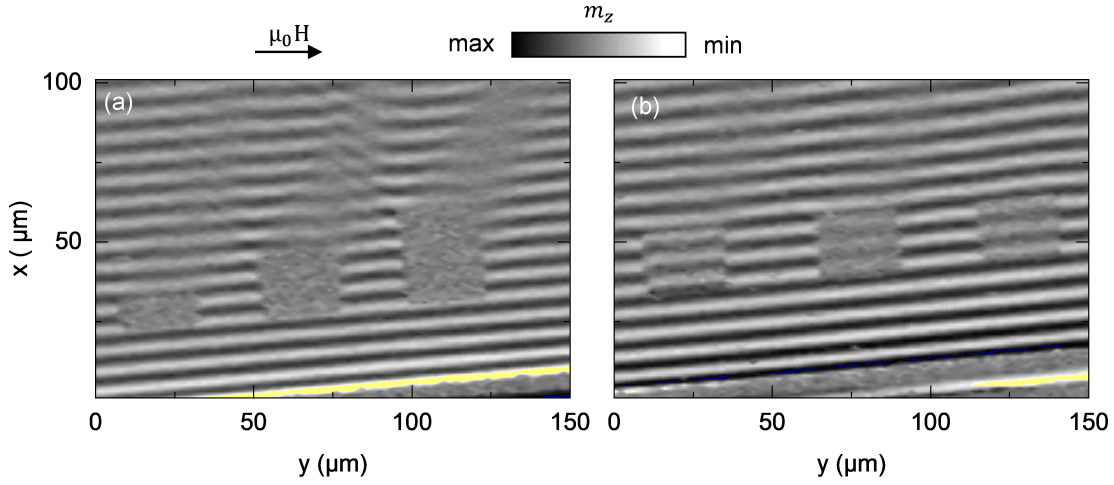
Figure 5.4: Two-dimensional TR-MOKE images for (a) (50 nm Au layer) on top of a 200 nm thick YIG film. The metallic rectangles with different length in x-direction (10 μm, 20 μm, 30 μm from left to right) demonstrate a stronger spin wave attenuation with increasing length. (b) Spin wave propagation underneath (20 nm Au), (20 nm Au/ 10 nm Pt) and a (10 nm Pt) rectangles. Spin waves can be observed even through the NM structures. All NM structures have a 5 nm Ti buffer-layer between the YIG and the Au. The rf-excitation frequency was 2.8 GHz at a fixed external magnetic field of 38 mT.

(5.3). However, it seems to become negligible for thin NM layers in the order of tens of nanometers, as can be seen in Fig. 5.4 (b).

One of the open questions is if we can measure propagating spin waves directly through the 20 nm Au and 10 nm Pt layers, presented in Fig. 5.4 (b), or if we observe an induced magnetic response inside the NM. Considering the Beer-Lambert law [Eq. (5.4)] to obtain the penetration depth δ_p of the fs-pulses into the NMs, we find that the length after which the fs-pulse intensity I_0 is reduced by a factor of 1/e within the NM is in the order of 10 nm, cf. Eq. (5.5).

$$I = I_0 \exp(-4\pi\kappa L/\lambda_0) = I_0 \exp(\alpha_\mathrm{a}L) \tag{5.4}$$

$$\delta_\mathrm{p} = \frac{\lambda_0}{4\pi\kappa} = \frac{1}{\alpha_\mathrm{a}} \tag{5.5}$$

67

Here, κ accounts for the extinction coefficient, $\lambda_0 = 800$ nm for the vacuum wavelength, and α_a for the absorption coefficient. Using literature values for the extinction coefficient, we find a penetration depth δ_p of about 13 nm for Au [148] and about 8 nm for Pt [149]. As a consequence, the penetration depth obtained by the Beer-Lambert law is below the NM thickness. Moreover, we have to consider double the thickness of the NM as the fs-pulses have to propagate twice through the NM due to the reflection at the FM/ NM interface.

To investigate the induced magnetic response, we deposit a 5 nm SiO_2 layer between the YIG and the NM structures which should prevent any spin currents from entering the NM layers. Figure 5.5 shows a two-dimensional TR-MOKE measurement for three different NM layers. A 50 nm thick Au layer (5 nm Ti underneath) is shown on the left-hand side of the figure. Spin waves can not be detected through the 50 nm Au film by the TR-MOKE measurement. However, an area with a lower intensity is observed behind this layer which indicates again that the effect that we are observing is not related to spin-pumping. A 20 nm Au film (5 nm Ti underneath) is shown in the middle structure in Fig. 5.5. A similar phase shift underneath the NM, as already presented in Fig. 5.4 (b), can be obtained for this structure. The 10 nm Pt film (5 nm Ti underneath) shown on the right-hand side of Fig. 5.5 has again a similar behavior as observed before. The phase shift obtained underneath the 10 nm Pt layer is less prominent compared to the 20 nm Au structure. As the spin wave behavior with and without a SiO_2 layer between the YIG and the NM structures is similar, this leads to the assumption that we observe the spin wave through the NM films and not within the NM. On the other hand, concerning the calculated penetration depth obtained from the Beer-Lambert law, gives rise to the assumption that we may observe the magnetic stray field inside the NM, induced by the propagating spin waves. This effect should lead to a non-reciprocity for surface spin waves [79] which will be investigated in the next Section.
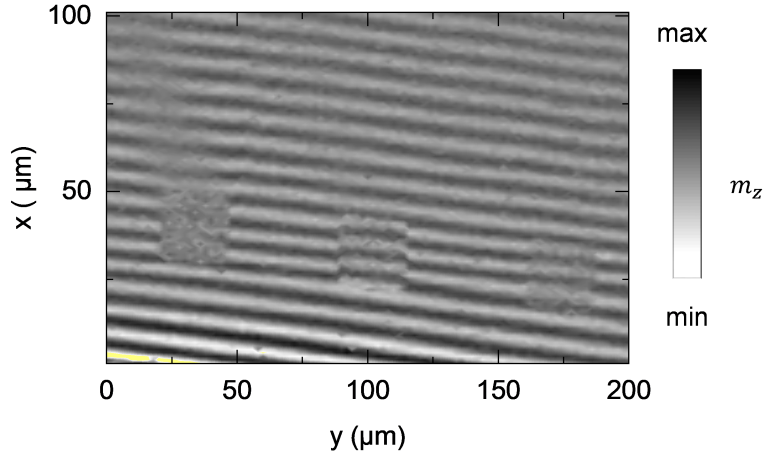
Figure 5.5: Two-dimensional TR-MOKE image for different NM structures with a 5 nm SiO_2 layer between the YIG film and the NM structures. The NM structures consist of 50 nm Au, 20 nm Au and 10 nm Pt from left to right. All structures had a 5 nm Ti buffer layer underneath. The 50 nm Au layer is again too thick to observe the spin wave trough it but an attenuation can be seen behind the structure. We observe a stronger phase shift underneath the 20 nm Au layer compared to the 10 nm Pt film.

5.3 Single-Layer NM-Induced Spin Wave Phase Shift

To investigate the effect of the buffer layer on the spin wave propagation, we fabricated a second series of samples which did not have a 5 nm Ti buffer layer between the YIG film and the NM structures. The second series of samples that will be investigated in this section comprises of 20 nm Au, 10 nm Pt and 20 nm Cu which were deposited using the same electron beam evaporation process as for the first series of samples with buffer layers. Furthermore, we designed larger structures to be able to optimize the data analysis for the phase shift and the effect on the dispersion of the spin waves, propagating underneath the NM.

Figures 5.6 (a) - (c) present the 2-dimensional TR-MOKE measurements of spin waves propagating underneath (50 x 50) µm metal structures of Au, Pt and Cu, respectively. A phase shift is observable for all three structures, where the magnitude of the phase shift seems to be different for each of the three NMs. To quantify the phase shift, we extracted x-line plots at specific y-positions passing through the NM structures

(coloured dashed lines in Figs. 5.6 (a)-(c)), in addition to reference x-line plots extracted from areas adjacent to the NM structures (black dashed lines in Figs. 5.6 (a)-(c)). To minimize phase differences caused by slight misalignments of the sample, both the measurement and reference x-line plots were chosen in close proximity to each other. The extracted line-plots are presented in Fig. 5.6 (d). The black solid lines in (d) correspond to the black dashed reference lines in Figs. 5.6 (a) - (c) which indicate an area without any NM on top of the YIG film. The colored symbol-solid lines in Fig. 5.6 (d) represent the line-plots for the NM areas indicated by the corresponding colored dashed lines in Figs. 5.6 (a) - (c). The phase, as well as the amplitude of the spin waves, seems to match the respective waves before and right after the NM areas. However, the phase observed at the NM areas is different for the three different NMs. The phase shift was determined by sinusoidal fitting the same x-range for each pair of corresponding waves. It was observed that the phase shift is most dominant for Cu.

There are areas behind the NM structures in Figs. 5.6 (a) - (c) which exhibit reduced spin wave amplitudes after passing underneath the NM. Furthermore, phase shifts can be observed between areas with and without reduced spin wave amplitudes. The most significant region for this effect can be seen in Fig. 5.6 (a) behind the right upper corner (around x = 80 µm, y = 70 µm) which shows an abrupt change in phase within the y-direction. From this observations, it seems that a decreased spin wave intensity is always accompanied by a phase shift of the spin wave, caused by the NM structures.

Based on the experimentally observed data, we argue that the change in intensity behind the thin NM layers are caused by destructive interference of spin waves affected by the NM with spin waves that are not, or less, affected by the NM.

There are still open questions about the formation of the phase shift and why the phase shift, observed in the NM areas, seems to have a certain jump at both boundaries between the metallized and non-metallized regions in the x-direction. TR-MOKE is an optical measurement principle, which is based on the change of the polarization direction of light reflected at the sample surface. Consequently, we have to distinguish between polarization manipulation of the light caused by reflection on a metallic surface, and the
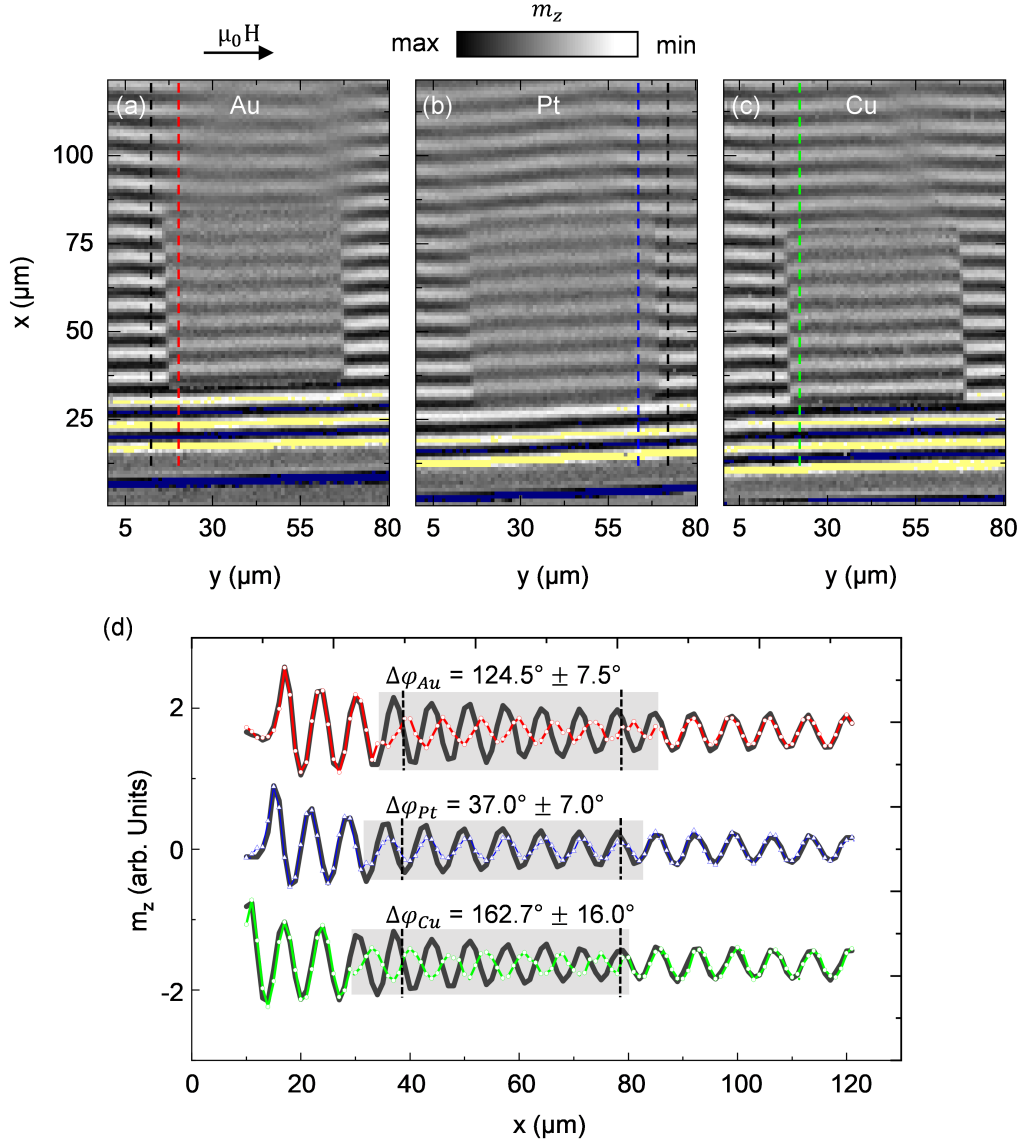
Figure 5.6: Two-dimensional TR-MOKE images of DE-like spin waves excited at 2.8 GHz at a bias magnetic field of 38 mT. The spin waves propagating underneath (a) 20 nm Au, (b) 10 nm Pt and (c) 20 nm Cu squares on top of a 200 nm YIG film. A phase shift is observed for spin waves propagating in the metallized YIG with respect to spin waves propagating in pure YIG. The phase shift for the different NMs at specific y-positions, indicated by the dashed lines in (a) - (c), are presented in (d). The phase shift was determined by sinusoidal fitting of the corresponding waves between the positions, indicated by the black dashed lines in (d). The region of the NM is indicated by the grey areas in (d). The fit is not shown to allow the clarity of the experimental data.

change of polarization caused by the MOKE. Changing the direction of the polarization can be equivalent to a change of the phase in the spin wave signal, which is the effect we are observing for the spin waves propagating in proximity to the NMs.

Figure 5.7 presents the effect of the polarization rotation on the differential photo-detector signal (A-B) (cf. Chapter 3.1). The signal was recorded without any AC filter elements in the electrical detector path. Furthermore, there was also no lock-in technique used to observe this data. A lambda half-waveplate (HWP), mounted in front of the Wollaston prism (WP), was rotated 360° by hand. By using the Jones formalism (cf. Section 2.6) we find that the angle of the polarization rotation θ, caused by the HWP, is twice the angle of the rotation of the HWP ϕ ($\phi = 2\theta$).

$$\mathbf{J}_{\text{system}} = \mathbf{J}_{\text{WP}}\mathbf{J}_{\text{HWP}} = \begin{bmatrix} \cos^2\vartheta & \sin\vartheta\cos\vartheta \\ \sin\vartheta\cos\vartheta & \sin^2\vartheta \end{bmatrix} \begin{bmatrix} \cos 2\phi & \sin 2\phi \\ \sin 2\phi & -\cos 2\phi \end{bmatrix} \tag{5.6}$$

$$= \begin{bmatrix} \cos 2\phi & \sin 2\phi \\ 0 & 0 \end{bmatrix} \tag{5.7}$$

Note that ϑ is measured with respect to the horizontal-axis and indicates the transmission axis for one polarization component of the WP. If we mount the WP in such a way that $\vartheta = 0$, $\mathbf{J}_{\text{system}}$ simplifies to Eq. 5.7. The fast axis of the HWP with respect to the horizontal-axis is indicated by ϕ. For horizontally polarized light ($E_x = 1$, $E_y = 0$), the amplitude of the electric field E_x after passing through the HWP and the WP is therefore given by

$$\begin{bmatrix} \cos 2\phi \\ 0 \end{bmatrix} = \begin{bmatrix} \cos 2\phi & \sin 2\phi \\ 0 & 0 \end{bmatrix} \begin{bmatrix} 1 \\ 0 \end{bmatrix}. \tag{5.8}$$

As a consequence, we observe a rotation of $\theta = 720°$ of the polarization direction by rotating the HWP by $\phi = 360°$.

The corresponding Jones matrix concerning the reflection from a surface is given by

$$\begin{bmatrix} -r_{\mathrm{p}} & 0 \\ 0 & r_{\mathrm{s}} \end{bmatrix} \tag{5.9}$$

where r_{p} and r_{s} are the Fresnel coefficients for p- and s-polarized light, respectively. The Fresnel coefficients are identical for normal incidence. As a consequence of this, we do not expect any polarization rotation, caused by the normal reflection from a surface.

Fig. 5.7(a) and (b) show the photo-detector signal taken from an area of pure YIG only, and from an area of metallized YIG with 20 nm Au deposited on top, respectively. The difference in amplitude for the photo-detector signal demonstrates the different reflection indices for YIG and Au. Besides the different amplitude, the differential signal shows the same behavior for both regions, as expected. By balancing the photo-detector, and with this aligning the differential signal (A-B) to zero for the area of pure YIG, we were able to obtain the change in polarization while scanning the laser across the NM areas of Au, Pt and Cu. Fig. 5.7 (c) shows the differential photo-detector signal as a function of the laser position. There is indeed a change in the polarization caused by the reflection of the laser on the NM surfaces. Imperfections on the normal incidence to the sample, and as a consequence unequal Fresnel coefficients in Eq. (5.9), are supposed to induce a rotation. However, the change in the direction of polarization, caused by the reflection, was calculated to be less than 1° which could not account for the phase shift observed for the spin waves propagating underneath the NM, presented in Fig. 5.6. Moreover, this polarization rotation is a static rotation which is suppressed by including AC filter elements in the photo-detectors electrical path, as well as by using a lock-in technique.

As a consequence, we assume that the spin wave phase shift observed at the metallized areas can not be an artifact caused by the reflection of the laser on the metallic surface. The actual reason for the observed phase shift is still under debate but could be additionally investigated by NV-center microscopy to further exclude optical artifacts. Modulating the susceptibility of the NM by the propagating spin wave could be one
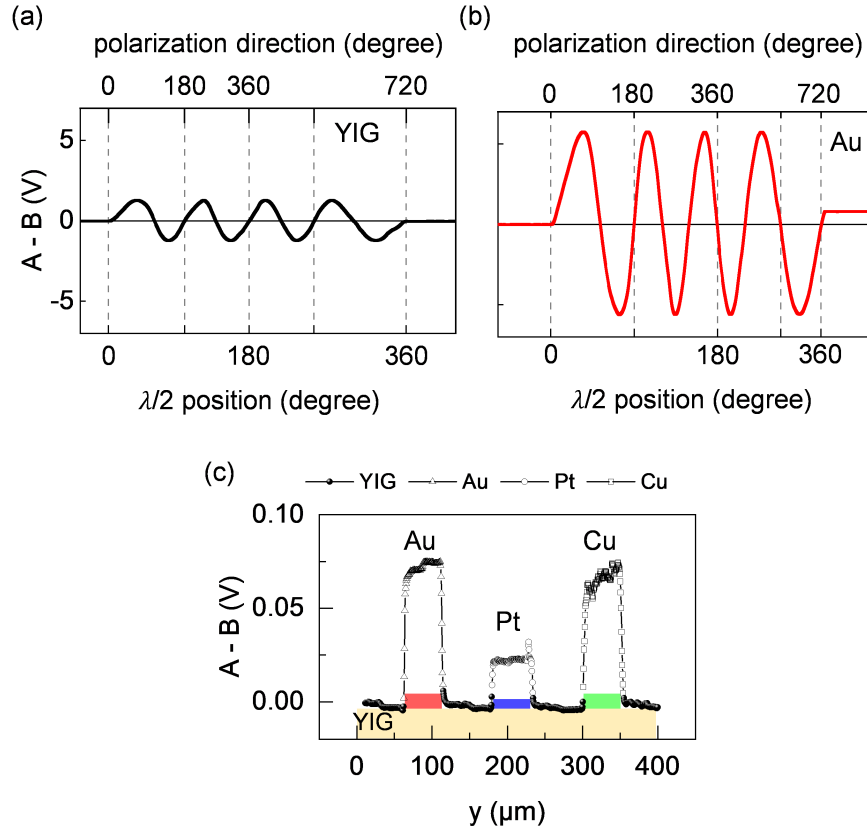
Figure 5.7: Static differential signal of the photo-detector as a function of the angle of the half wave-plate in front of a Wollaston-prism. The laser-focus was located at (a) pure YIG and (b) 20 nm Au on top of YIG. The wave-plate was rotated by hand which is the reason for the deviation from a perfect sinusoidal behavior. A polarization shift by 180° could not be recognized by the detector but a shift of 90°, as the slope at the balanced position (A - B = 0) is the inverse with respect to 0°. (c) demonstrates the static change in the differential signal while scanning across the metallized YIG. The differential signal corresponds to a change of the polarization of about 0.7° while scanning across the Au and Cu regions and of about 0.2° for scanning across the Pt region.

ansatz for the observed phase shift underneath the NM.

5.4 NM-Induced Non-Reciprocity of DE Spin Waves

For a deeper analysis of the effect of the metallized YIG on the propagating spin waves, we measured the dispersion relation for the spin waves propagating underneath the NM

squares, shown in Fig. 5.8. We performed measurements at both sides of the CPW as the DE-like spin waves propagate at opposite surfaces concerning the side of the CPW.

As the NM layers should induce an effect only on the upper surface of the YIG film, we assume non-reciprocity for the DE-like spin waves [79]. Moreover, the pinning condition for PSSW's will be changed at the upper surface and, as a result, this should affect the hybridization for $n = 0$ and $n = 1$ DE spin wave modes, as demonstrated in Section 4. Figure 5.8 shows the spin wave propagation in the x-direction on both sides of the CPW as a function of the bias magnetic field. The spin waves have been excited in DE-like geometry at a given rf-frequency of 3.2 GHz. Fig. 5.8 (a) shows the experimental data for an area with pure YIG. A hybridization gap starting at around 45 mT is observed for both sides of the CPW. Performing the same measurements for the areas of metallized YIG with Au, Pt or Cu deposited on top, respectively, in Figs. 5.8 (b) - (d) demonstrates an extended hybridization area that starts clearly before 45 mT. We extracted the spin wave wavelength for the areas indicated with the colored rectangles by sinusoidal fitting every line scan in the x-direction. The colored rectangles in Figs. 5.8 (b) - (d) indicate the NM regions. By analyzing the DE-like spin waves with a higher amplitude at the top surface of the YIG layer (left-hand side of the CPW), we observe a significant difference in the dispersion relation. Figure 5.9 (a) presents the extracted **k**-values from the sinusoidal fits as a function of the bias magnetic field for the NMs as well as for pure YIG. It can be seen that the hybridization gap becomes more prominent for the metallized YIG compared to pure YIG. Interestingly, it seems that the dispersion is shifted down to lower magnetic field values only for the lower branch of the hybridization of the $n = 0$ and $n = 1$ DE spin waves. An increase of the anti-crossing gap by about 1 mT is observed for the metallized YIG. Moreover, there is a difference in the k-value, and in turn in the wavelength, of spin waves propagating in pure YIG compared to spin waves propagating in metallized YIG. We argue that this causes a phase shift for the spin waves propagating underneath a NM with respect to the phase of adjacent spin waves propagating through pure YIG. As a result, this phase shift can lead to destructive interference effects, due to the long-range dipole-dipole interaction,
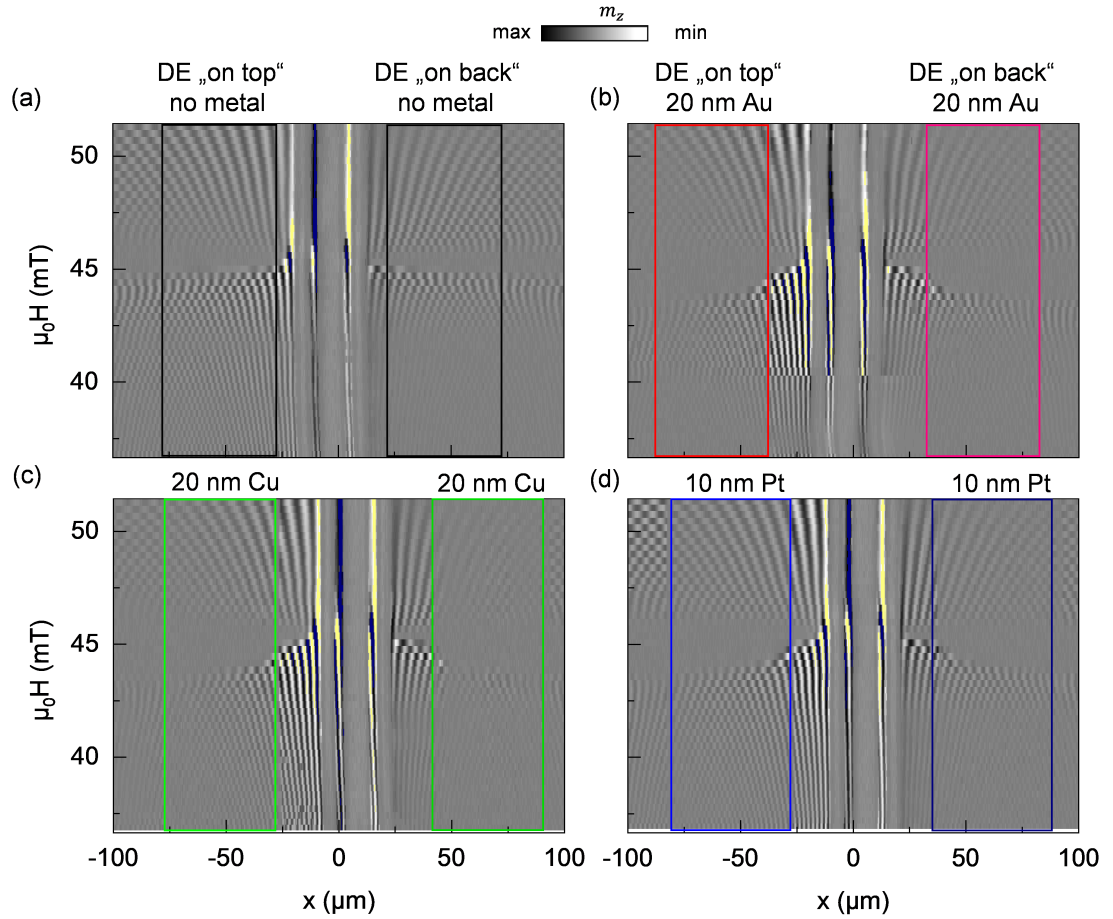
Figure 5.8: DE-like spin wave propagation on both sides of a CPW as a function of the external magnetic field at a given rf-frequency of 3.2 GHz. The spin wave transmission stop band for pure YIG (a) is smaller compared to the metallized YIG (b) - (c). The colored rectangles indicate the areas for which the wavelength, and in turn the wavevector **k**, were extracted (Fig. 5.9).

which results in a decreased spin wave amplitude.

Fig. 5.9 (b) demonstrates the wave-vector extracted from the area to the right-hand side of the CPW, shown in Fig. 5.8. As already predicted in 1970 [79], we observe non-reciprocity of DE spin waves propagating in the negative x-direction (left-hand side of the CPW) compared to DE spin waves propagating in the positive x-direction (right-hand side of the CPW), cf. Eq. (2.41). The surface-wave character of DE-like spin waves causes this effect. It can be seen that the non-reciprocity gets less dominant for smaller **k**-values, or larger wavelengths, as the surface character of DE-like spin waves scales exponentially with the wavelength [150]. Fig. 5.9 (c) presents exemplary the non-reciprocity of metallized YIG with NM Pt. There is a clear shift between the spin waves propagating in opposite directions, i.e. at the lower and upper surfaces. A DE $n = 1$ mode, which shows a standing mode profile within the film thickness (PSSW), leads to hybridization within the region of theoretical mode crossing (see also Fig. 4.5). It can be seen in Fig. 5.9 (b) and (c) that the non-reciprocity does not hold in the vicinity of the hybridization as the pinning condition for the $n = 1$ PSSW gets affected by the NM of spin waves propagating in both, positive and negative x-directions.

Considering a NM induced uniaxial perpendicular magnetic anisotropy $H_\perp$ (uniaxial PMA) in the dispersion relation, described by Eq. (2.14), may also lead to a non-reciprocity of magnetostatic surface waves. The uniaxial PMA can be described by

$$H_{\text{ani}} = H_\perp = \frac{2k_u^\perp}{\mu_0 M_{\text{s}}^2} M_z \mathbf{e}_z \tag{5.10}$$

Calculation of the dispersion by including the uniaxial PMA leads to an anisotropy field of $H_{\text{ani}} < 0.5\,\text{mT}$ for the non-reciprocal dispersion of Pt/YIG, presented in Fig. 5.9 (c). Measuring such a small field contribution might be challenging with other techniques like, for example, FMR. As a consequence, we haven't performed additional experiments to further investigate the influence of the uniaxial PMA on the dispersion relation.
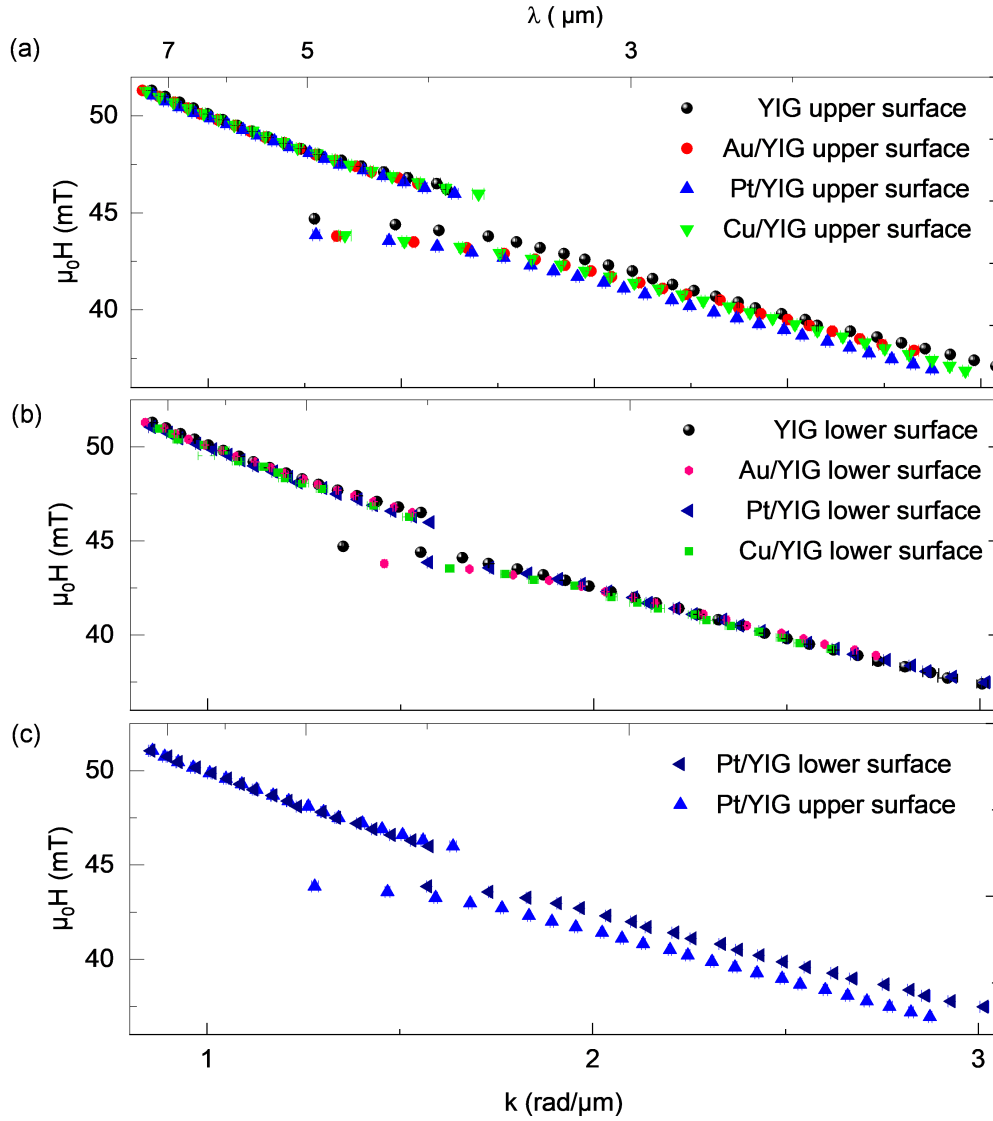
Figure 5.9: Extracted wave-vectors from the areas indicated in Fig. 5.8. (a) for DE-like spin waves propagating at the upper surface, (b) lower surface and (c) an exemplary comparison between upper and lower surface for Pt. The NM induced non-reciprocity is observed by the shift in the dispersion relation between the spin waves propagating at the upper (a) and lower (b) surfaces.

5.5 Optic-Like Spin Wave Manipulation

Observing the non-reciprocity of DE-like spin waves indicates that the metal-induced phase shift is not just an artifact resulting from the optical TR-MOKE measurement. As a consequence, we should be able to use this phenomenon to control a phase-front distortion of the spin wave. For this, NM structures which allow in a change in the effective metallized length as a function of the y-direction, perpendicular to the wave-vector of the spin wave, were fabricated, i. e. metallic triangles. Figure 5.10 demonstrates the effect of three triangular-shaped NMs, fabricated from 20 nm Au, 10 nm Pt and 20 nm Cu. The observed phase-shift underneath the NM is similar to the one observed and analyzed in Fig. 5.6. However, the effect on the wave-front seems to be rather different for the three different NMs. The wavefront for the spin wave passing the NM areas with Cu and Pt becomes a convex shape behind the triangles. This can be understood as spin waves propagating underneath the middle area of the triangle, also called the perpendicular bisector, have a longer interaction with the NM in the x-direction compared to spin waves propagating at the edges of the triangles. As we have already shown in Fig. 5.4 (a), the length of the metallized area affects the phase shift of the spin waves, and as a result the phase shift resulting from a triangular-shaped NM will vary across the y-direction of the NM. The convex shape of the phase fronts behind the Cu and Pt triangles resemble somewhat of a Fresnel-diffraction pattern of a single slit in optics experiments [151]. On the other hand, the 20 nm Au triangle shows not only a convex wavefront behind the triangle but also a concave shape before it is transformed into a convex shape. A similar manipulation of the wavefront is well known in optics for the formation of an image point, or the Fraunhofer-diffraction pattern, of the aperture of an optical lens [151]. In addition to the phase front difference, we observe caustic-like emissions from the tip of the Cu and Pt triangles.

As a result, we have demonstrated an optic-like manipulation of spin waves by locally changing the dispersion relation of DE-like spin waves by using simple single metallic structures. Figure 5.11 demonstrates the ability to control the direction of the spin wave
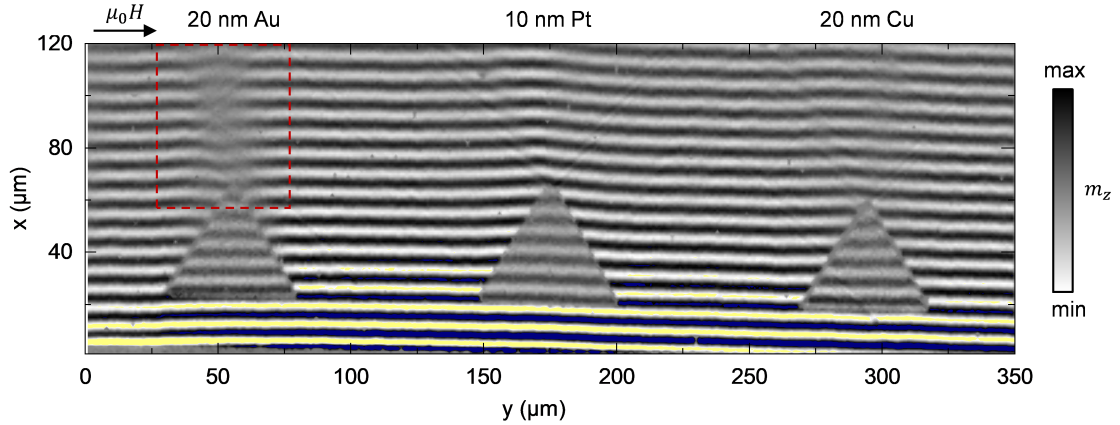
Figure 5.10: Demonstration of optic-like spin wave manipulation by triangular shaped metallized areas on top of a 200 nm YIG film. The rf-excitation frequency was 2.8 GHz at a fixed bias external magnetic field of 36 mT. There is a concave shaped wavefront propagating behind the Au triangle which transfers into a convex shaped wavefront (red dashed rectangle). This effect is well known in optics for the formation of an image point or the Fraunhofer-diffraction pattern of the aperture of an optical lens. The convex wavefronts behind the Pt an Cu triangles resemble the Fresnel-diffraction pattern of a single slit experiment.

diffraction-like pattern by simply changing the bias magnetic field direction. It can be seen that the area of lower spin wave intensity can be shifted by an angle away from the DE-like propagation direction. This is another evidence that the observed phenomena neither depends on eddy-current-induced damping nor spin-pumping-induced damping, as we would otherwise observe an attenuated spin wave behind the NM structure in the direction of the spin wave propagation alone. In contrast, our results demonstrate a contribution to the wave-vector pointing along the y-direction (k_y). Even if the bias magnetic field is slightly misaligned with respect to the CPW direction, the direction of the wave-vector, excited by the CPW, is given by the orientation of the CPW. Only wave-vectors which are perpendicular to the CPW will be excited. Imperfections or particle's on top of the magnetic film can act as excitation sources of spin waves, which do not depend on the orientation of the CPW anymore. The tip of the triangles seems to be such a source of spin wave excitation as it can be seen that the slight change in the direction of the bias magnetic field, away from a perfect DE-like geometry, leads to

a wave-vector contribution in the y-direction, illustrated in Fig. 5.11 (e).

We presented the effect of different NM-bilayers as well as NM-single layers on the spin wave propagation within a 200 nm thick YIG film. Eddy-current-induced damping, as well as spin-pumping-induced damping, was considered for the experimentally observed spin wave attenuation by the NM on top of the YIG film. Comparing the experimentally observed NM-induced damping for 105 nm thick NM structures with a calculated eddy-current-induced damping contribution, showed that they do not coincide with each other. Spin-pumping-induced damping was investigated experimentally as well as theoretically. The calculated spin-pumping contribution to the damping of the DE-like spin waves for both, Au and Pt, was on the same order of magnitude as the intrinsic Gilbert damping for thin YIG. We experimentally excluded the effect of spin-pumping, as well as the magnetic proximity effect (MPE) induced damping, by separating the NM with a 5 nm SiO_2 layer from the YIG. We observed a strong difference in the damping behavior for 105 nm NM compared to 55 nm NMs. As spin-pumping, as well as the MPE, are interface effects, the damping induced by these effects should not change by varying the NM thickness in the order of tens of nm.

We have demonstrated a NM-induced non-reciprocity for the DE dispersion by direct imaging spin waves through NM with the help of TR-MOKE measurements. Changing the dispersion can lead to the hybridization of two spin wave modes and as a consequence to an enhancement of the spin wave damping. Furthermore, changing the dispersion will lead to a phase shift of spin waves concerning undisturbed spin waves. As a result, that phase shift causes destructive interference and in turn an attenuated spin wave amplitude.

By exploiting the influence of NMs on the propagation behavior of spin waves, we have first demonstrated an optic-like spin wave manipulation by single NM structures. Moreover, the direction of the diffraction pattern, arising from the apex of a triangular Au structure, could be controlled by simply changing the external magnetic field direction.

This work contributes to a deeper understanding of the interaction and manipulation
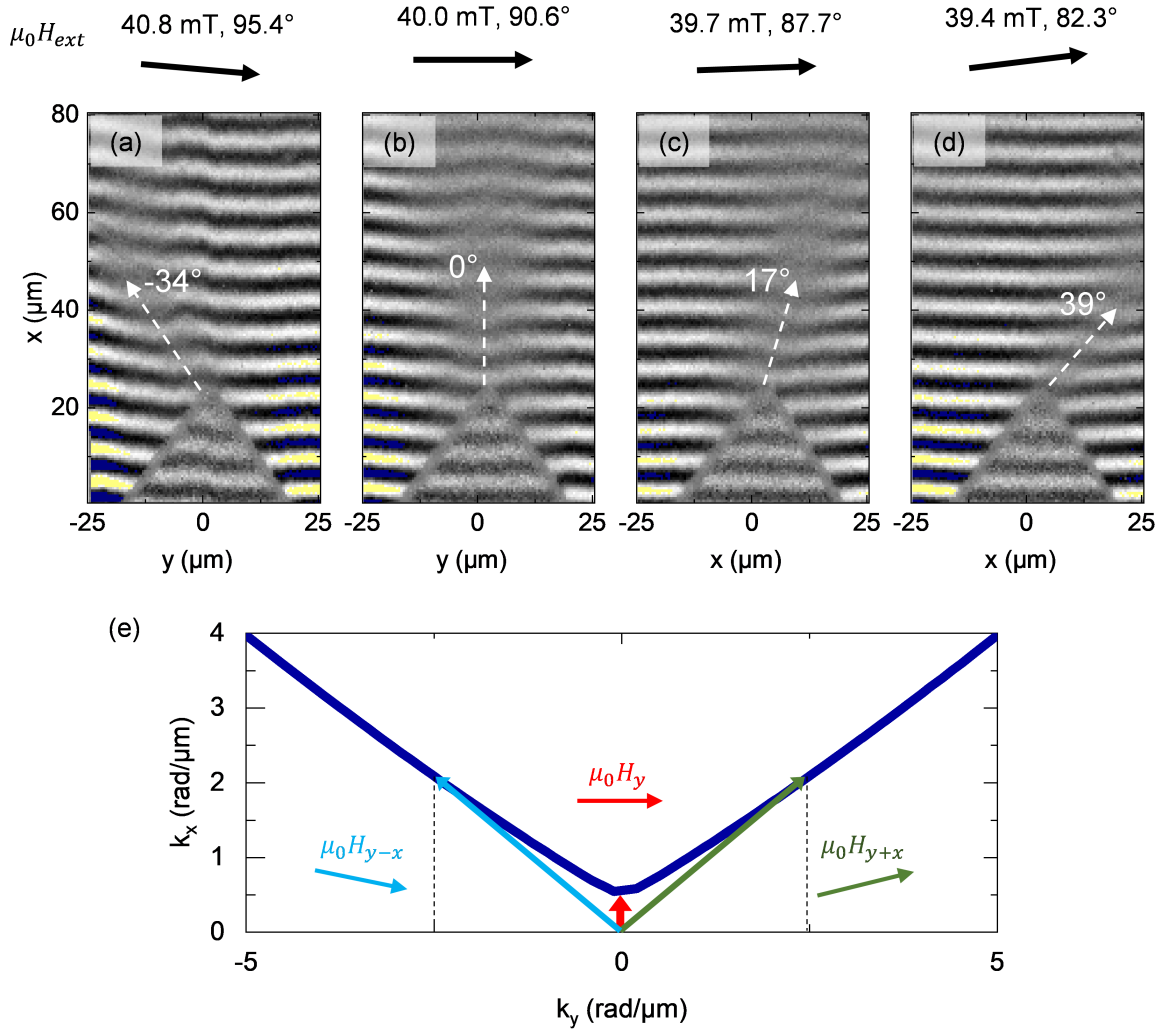
**Figure 5.11:** (a) - (d) demonstrates the ability to control the direction of the spin wave diffraction-like pattern by changing the in-plane angle of the bias magnetic field. A x-component of the bias magnetic field gives rise to a y-component of the wave-vector **k** (k_y), shown in (e).

of propagating spin waves in proximity to NMs which might be useful for the future development of magnonic devices.

Chapter 6

Non-Continuous Excitation of Magnetization Dynamics

Pulsed magnetization dynamics has become a topic of increasing interest in recent years [98, 152–158]. Using magnetization dynamics as an information carrier, as well as for switching the magnetizing direction in nano-pillars, requires not a continuous but a pulsed excitation of the magnetization dynamics. Magnetic vortex core reversal [152, 154, 155], spin-orbit torque induced switching [157], and spin-orbit torque driven magnetization dynamics [156] have demonstrated that a pulsed excitation of the magnetization dynamics is a powerful tool to manipulate the state of the magnetization. Moreover, it was demonstrated that the dispersion relation for a 100 nm thick YIG film can be measured by a single shot acquisition of spatially resolved magnetization dynamic [98]. Achieving the dispersion relation was done by time-resolved scanning transmission X-ray microscopy (TR-STXM) at a synchrotron facility.

It was already shown in the previous chapters that observing the dispersion relation can be a powerful tool for analyzing spin wave phenomena.

In this section, we will report the pulsed spin wave excitation in a Py thin film, using the table-top TR-MOKE technique. We will investigate the propagation behavior of different pulse shapes (e.g., Gaussian, chirp and sinc pulses). Furthermore, the spin

wave dispersion relation for the Py film is observed using a sinc pulse as well as a modified sinc pulse excitation with a table-top TR-MOKE system instead of a synchrotron-based TR-STXM.

6.1   rf-Pulse Excited Magnetization Dynamics

Figure 6.1 presents the pulse shapes used for exciting magnetization dynamics in the time and frequency domain. The pulse width, and with this the frequency components of the pulses, are limited by the arbitrary waveform generator (AWG) used for the experiments. In the framework of the presented thesis, we used a Tektronix AWG 7001A which provides a sample rate of 50 GS/s whereas it can provide rf-output signals up to 20 GHz. Figs. 6.1 (a) - (d) present the voltage course over time for pulse shapes used in this work with their corresponding frequency components shown in (f) - (h). The shorter the pulse becomes in time the more frequency components are included in the pulse itself. The parameters given in Figs. 6.1 (a) - (d) are parameters that can be adapted to the experiment. However, the limits for these parameters are given by the AWG as already mentioned above. Fig. 6.1 (a) presents a Gaussian shape voltage pulse described by

$$U_G = A \cdot \exp\left\{ \left(-\frac{t^2 - t_0}{2 \cdot b^2} \right) \right\},$$ (6.1)

with A the amplitude of the pulse, t_0 the center position in time, and b the control of the width of the bell shape. Fig. 6.1 (e) presents the corresponding frequency spectra which is described by a Gaussian function as well.

A chirped pulse shape is shown in Fig. 6.1 (b). The characteristic of a chirp function is the change in its frequency over time. A mathematical description of such a chirp function is given by

$$U = A \cdot \sin\left(\pi \left[f_a + t\frac{(f_e - f_a)}{\tau} \right] \cdot t \right),$$ (6.2)
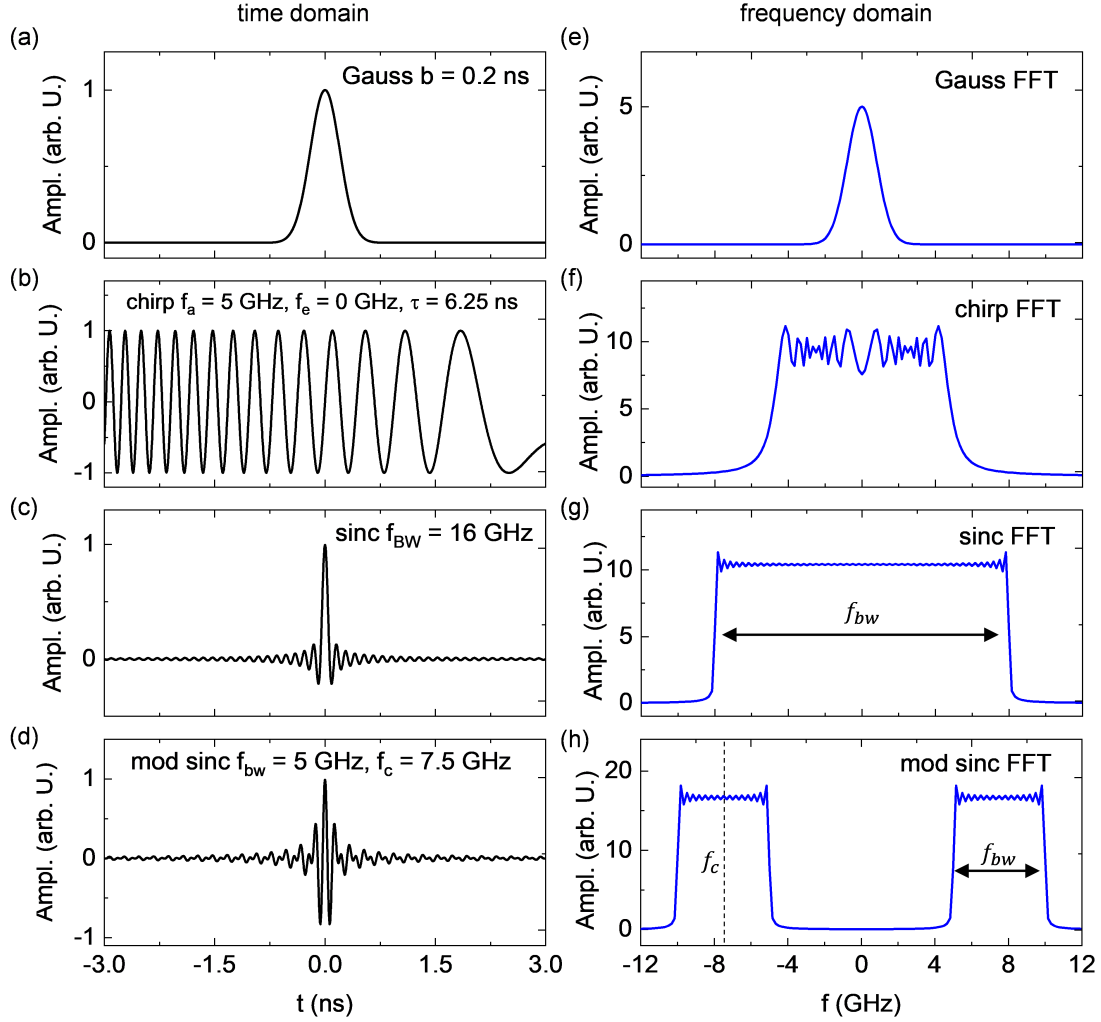
Figure 6.1: Illustration of the temporal traces for different voltage pulses (a) - (d) with their corresponding frequency spectra (e) - (h). The parameter b controls the width of the Gaussian pulse in (a). f_a and f_e correspond to the start and the end frequency for the chirp pulse shown in (b), respectively. τ characterizes the time to reach the end frequency f_e. The center frequency and the bandwidth for a sinc pulse (c) and a modified sinc pulse (d) are defined by f_c and f_{bw}, respectively.

with A the amplitude of the chirped oscillation, f_a the start frequency, f_e the end frequency and τ the time constant to approach the end frequency. The frequency spectra for a chirp pulse with $f_a = 5$ GHz, $f_e = 0$ GHz and $\tau = 6.25$ ns is shown in (f).

Fig. 6.1 (c) presents a sinc pulse function which can be described by

$$U = A \cdot \frac{\sin(\pi \cdot f_{bw} \cdot t)}{\pi \cdot f_{bw} \cdot t} = A \cdot \mathrm{sinc}(\pi \cdot f_{bw} \cdot t), \qquad (6.3)$$

with A the amplitude at the center position of the function. The frequency f_{bw} defines the bandwidth in the frequency domain which is presented in Fig. 6.1 (g). The characteristic of the sinc pulse-function is the rectangular-shaped frequency band. To be able to excite magnetization dynamics with an arbitrary rf-frequency range we define a modified sinc function as shown in Fig. 6.1 (d), which is mathematically described by

$$U = A \cdot \mathrm{sinc}(\pi \cdot f_{bw} \cdot t) \cdot \cos(2\pi \cdot f_c \cdot t). \qquad (6.4)$$

The modified sinc pulse function also contains a rectangular shape in the frequency domain but located around the center frequency f_c with a bandwidth f_{bw}. Fig. 6.1 (h) presents the frequency spectra for a modified sinc pulse with a center frequency $f_c = 7.5$ GHz and a bandwidth $f_{bw} = 5$ GHz.

Figures 6.2 (a) - (c) present the experimentally observed propagation away from the CPW as a function of time and space, measured by the TR-MOKE technique. One of the ground lines of the CPW is indicated by the yellow rectangles in Figs. 6.2 (a) - (c). The temporal trace of the pulses was shifted in time by shifting the output signal of the AWG in phase, with respect to an internal oscillator of the AWG. The AWG internal phase can be shifted by $\pm\ 10000°$ with respect to the AWG internal clock, which has a frequency of $f_{AWG} = 12.0$ GHz. This corresponds to a maximum shift in time of 4.63 ns which was used for the measurements presented in Fig. 6.2 (a) - (c). The Gaussian pulse function shown in (a) was created with the parameter $b = 10$ ps which results in a frequency bandwidth of about $\pm\ 20$ GHz. This is at the limit of the AWG's dynamic range and will give the shortest pulse, excited by a Gaussian pulse function, possible.
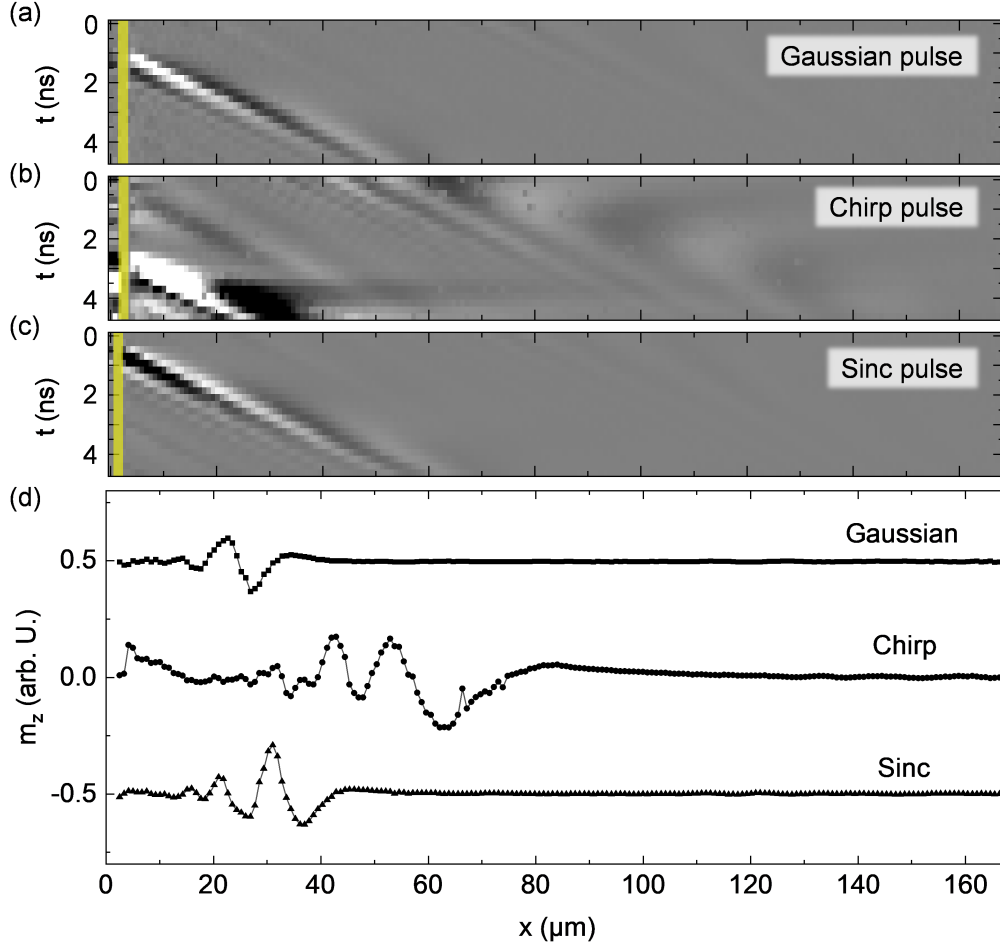
Figure 6.2: TR-MOKE measurement of propagating magnetization dynamics, excited by different rf-current pulse shapes as a function of time. (a) shows a Gaussian pulse excitation with a parameter $b = 0.01$ ns, (b) a chirped pulse excitation with a start frequency $f_a = 5$ GHz and an end frequency of $f_e = 0$ GHz with a time constant $\tau = 6.25$ ns. (c) presents a sinc pulse excitation with a bandwidth of $f_{bw} = 16$ GHz. A bias magnetic field of $\mu_0 H = 20$ mT was applied along the y-axis (DE-like excitation) for all measurements. (d) Pulse shape extracted from (a) - (c) at a given time of about 3 ns, 0 ns, and 3 ns, respectively. It can be seen that the pulse, excited by a Gaussian shape, becomes the shortest one in space as it contains the highest frequency components due to the short pulse width ($b = 10$ ps).

It can be seen that the pulse propagating away from the CPW is well-defined within the Py film. The data observed for a propagating chirped pulse excitation is shown in Fig. 6.2 (b). The chirped pulse-excitation seems to be conserved for the propagating pulse within the Py thin film. The contrast in (b) is over-saturated in the area of the second chirp pulse close to the CPW (between 0 µm to about 30 µm) for a better illustration of the first chirp pulse within the area starting from about 30 µm. To excite the magnetization dynamics with a box-like function in the frequency domain, we used a sinc pulse excitation. Fig. 6.2 (c) presents the TR-MOKE measurement for the sinc pulse propagating away from the CPW. A well-defined propagating pulse-like shape can be observed, similar to the Gaussian pulse excitation. The preceding pulse is still observable starting from about $x = 80$ µm at $t = 0$ ns. Comparing the three different pulse shapes in Fig. 6.2 (d) illustrates the difference between each other. The Gaussian shape seems to propagate with almost no trace compared to the sinc pulse function. However, the propagating Gaussian pulse does not show a pure Gaussian-like shape but more a double peak shape with a positive and negative amplitude. The chirp pulse, on the other hand, seems to keep its chirp character also when propagating within the Py thin film. A rather clear phase front is observable for both, the Gaussian pulse as well as for the sinc pulse. The latter one shows a trace behind the pulse which seems to be comparable to the sinc function used for the excitation of the pulse.

6.2 Propagation Characteristics of rf-Pulses

Analyzing the pulse profile for the Gaussian-like pulse in space demonstrates the difference between the phase velocity and the group velocity. The Gaussian pulse propagates with a phase velocity of $v_{\mathrm{ph}} = (9.22 \pm 0.28)$ km s^{-1} within the 60 nm thick Py layer. Figure 6.3 presents the x-line scans for different points in time, extracted from the data shown in Fig. 6.2 (a). To investigate the phase velocity of the propagating pulse, a Gaussian fit was applied to an area that shows a positive peak amplitude, indicated by the red solid lines in Fig. 6.3. The center of the Gaussian fit was used to extract the

position of the corresponding peak for the different points in time. The fitting process for the x-line plot at 4.40 ns presented in Fig. 6.3 did not converge anymore which is the reason why it was not considered for analyzing the phase velocity.

To obtain the group velocity for the Gaussian-like pulse, we analyzed the envelope of the x-line plots by finding the extreme values and performing a cubic spline-interpolation through these points (blue dashed line in Fig. 6.3). Defining a constant group velocity for the propagating Gaussian-like pulse was not possible. A constant group velocity can only be observed if the dispersion relation for the observed phenomena has a linear dependence of the wave-vector with respect to the frequency. This is, for example, true for light propagating in a dispersive medium but not for propagating spin waves. The calculated dispersion relation for a 60 nm Py film at a bias magnetic field of 20 mT is presented in Figure 6.4 (a). Taking the derivation of the dispersion relation leads to the group velocity $v_{gr} = d\omega/dk$, shown in Fig. 6.4 (b). Note that we have shown frequency (f) over the wave-vector $\mathbf{k}$ in (a) but calculated the group velocity $d\omega/dk$ concerning the angular frequency $\omega = 2\pi f$ for better comparability with the experiment. As a result of this, we observe the unit of the group velocity to be $(\mathrm{km\,s^{-1}})$ instead of $(\mathrm{km\,rad^{-1}\,s^{-1}})$. Fig. 6.4 (b) demonstrates that the group velocity is a non-linear function of the wave-vector $\mathbf{k}$, being the reason why we can not define a constant group velocity for a pulse, propagating through the Py film. By analyzing the envelope for the pulses we observe a non-linear broadening over time or distance as a consequence of the non-linear group velocity.

Analyzing the propagation characteristic for a chirp-like pulse within the 60 nm Py film is presented in Figure 6.5. The grey shaded area indicates the amplitude of the extracted x-line plots from Fig. 6.2, which was multiplied by a factor of 0.13 for better visibility of the other data. An up-chirped pulse is observed for the propagating pulse, which means the frequency of the pulse increases over time, i.e., decreases over space. Interestingly, we excited the magnetization dynamics with a down-chirped pulse, presented in Fig. 6.1 (b). A down-chirped pulse decreases its frequency over time, which means an increasing frequency in space, at a given time. Fig. 6.5 shows an opposite
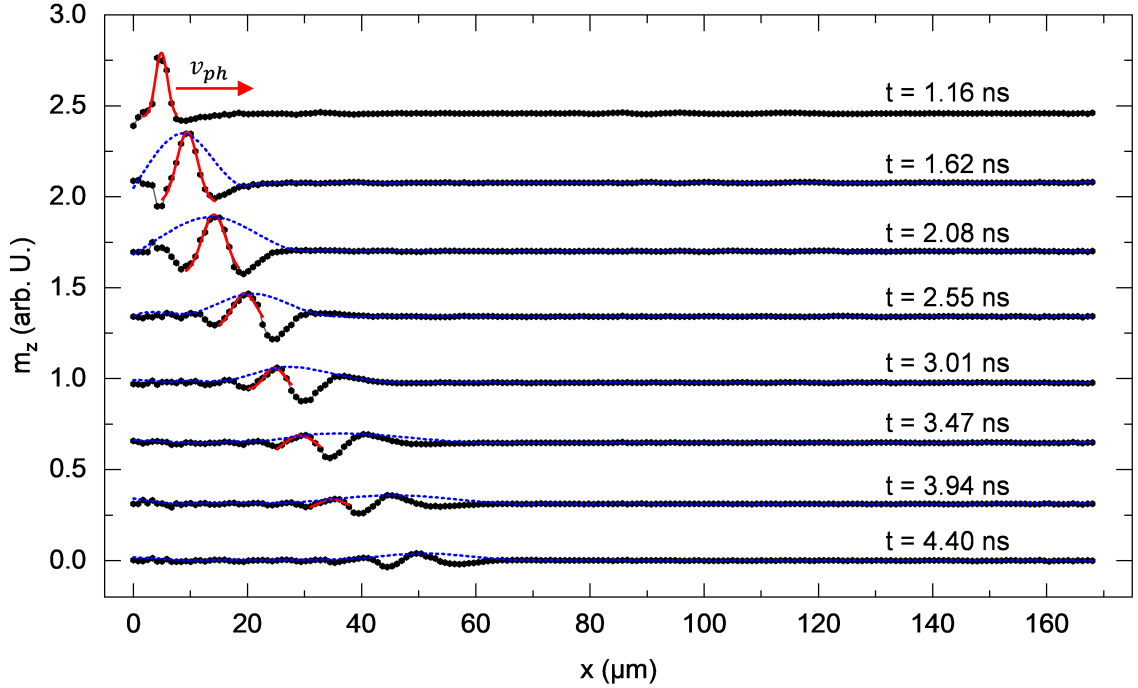
Figure 6.3: Extracted x-line plots for a Gaussian pulse excitation with a parameter $b = 0.01$ ns. A bias magnetic field of 20 mT was applied along the CPW (DE-like geometry). A phase velocity of $v_{\mathrm{ph}} = (9.22 \pm 0.28)$ km s^{-1} was observed by fitting a positive peak with a Gaussian function (red solid lines). The blue dashed lines represents the upper envelope for the Gaussian pulse. A pulse-broadening over time and space of about 55 % was observed between the $t = 1.62$ ns and $t = 4.40$ ns measurement. Data has been shifted vertically for clarity.

characteristic in our measurements. This can be explained by two reasons. The first one is the normal, but non-linear dispersion behavior for spin waves within the Py film, shown in Fig. 6.4. The dispersion relation shows a normal dispersion behavior, which means the group velocity decreases for increasing wave-vectors **k**, i.e., increasing spin wave frequency. A down-chirped pulse unavoidably becomes an up-chirped pulse over time following normal dispersion behavior, which is what we observe experimentally. We also have to point out that the magnetization dynamics within the 60 nm Py film at a bias magnetic field of 20 mT can not be excited by rf-frequencies below 4 GHz, also shown by the calculated dispersion relation in Fig. 6.4 (a). As a result of this, we
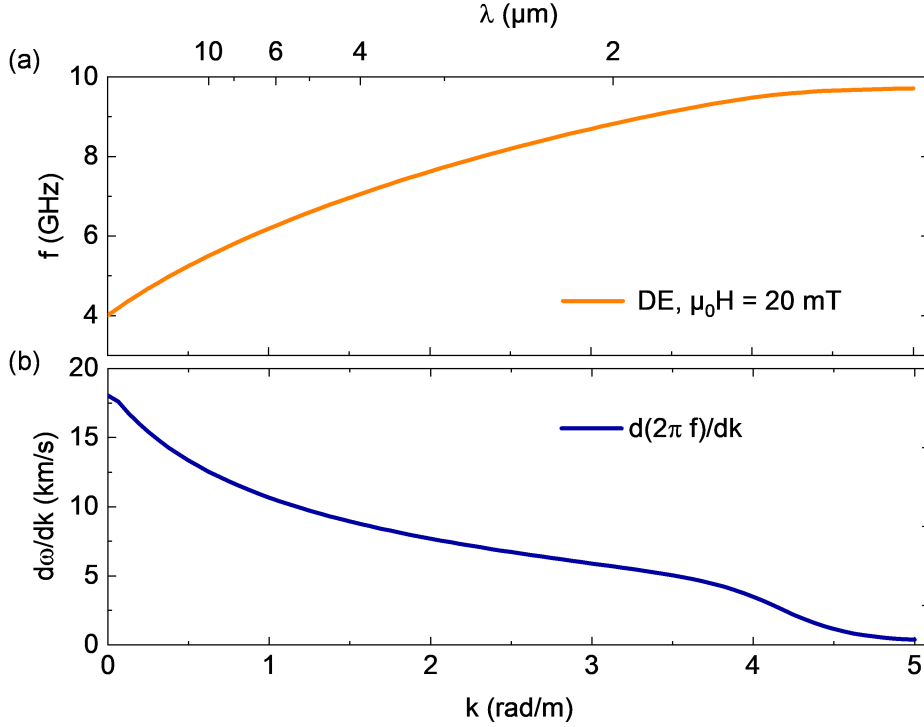
Figure 6.4: (a) Calculated dispersion relation for a 60 nm Py film and a bias magnetic field of 20 mT in DE-geometry. The dispersion relation for spin waves is not linear which results in a **k**-vector dependent phase velocity. (b) Derivation of the angular frequency ω ($2\pi f$) over the **k**-vector to observe the group velocity $v_{\mathrm{ph}} = d\omega/dk$. Note that we used the angular frequency ω instead of the frequency f to arrive at a unit of $(\mathrm{km\,s}^{-1})$ for the phase velocity.

expect only the first 1.25 ns of the chirp pulse, shown in Fig. 6.1 (b), to contribute to the excitation of the magnetizing dynamic in the Py film. A delay time of $t = 1.25$ ns is the time after which the chirp pulse decreases its frequency by 1 GHz, from 5 GHz to 4 GHz. Gilbert damping for the magnetization dynamics within the Py film broadens the line-width of the dispersion relation which allows frequencies slightly below 4 GHz to be excited as well, which was neglected in the calculation of the dispersion relation, due to the rather low damping of Py.

The propagation behavior for a sinc pulse function, which was already presented in Fig. 6.2 (c), is analyzed in more detail in Figure 6.6. We extracted a phase velocity
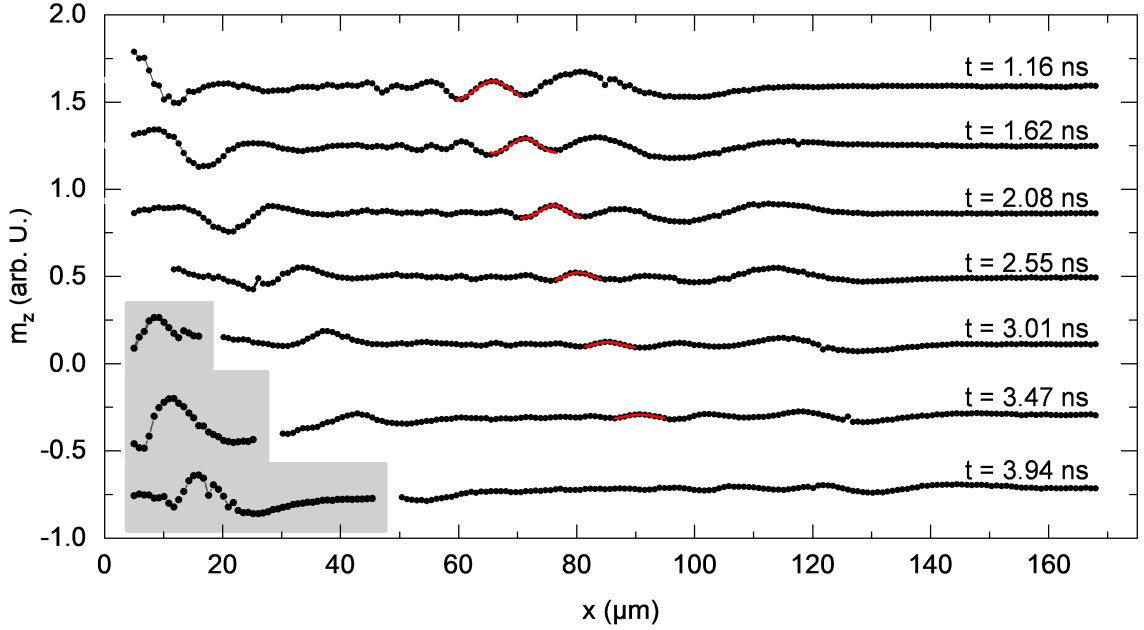
Figure 6.5: x-line plots for a propagating chirp pulse with a start frequency $f_a = 5$ GHz and an end frequency $f_e = 0$ GHz with a time constant $\tau = 6.25$ ns. The line-plots are extracted from the data shown in Fig. 6.2 (b). The grey indicated areas where multiplied by a factor of 0.13 for a better visibility. A phase velocity of (10.79 ± 0.23) km s^{-1} was observed by fitting a peak with constant phase by a Gaussian function (red solid lines). Data has been shifted vertically for clarity.

$v_{\mathrm{ph}} = (9.29 \pm 0.23)$ km s^{-1} by fitting a peak with a positive amplitude by an asymmetric peak function (red solid lines in Fig. 6.6). There was almost no broadening of the pulse-width observable by analyzing the width of the envelope [blue dashed line in Fig. 6.6]. As a consequence, this makes a sinc pulse function a promising candidate for experiments, which require well defined excitation in both, space and time. With this, we have shown the propagation characteristic for different rf-pulses within a 60 µm Py film. All the pulses have been excited in the DE-like geometry (bias magnetic field along the direction of the CPW).

To investigate the DE-like behavior for a sinc pulse with a frequency bandwidth $f_{\mathrm{bw}} = 16$ GHz, we measured the pulse propagation as a function of time on both sides of the CPW, shown in Figure 6.7 (a). Considering a DE-like propagation, we expect
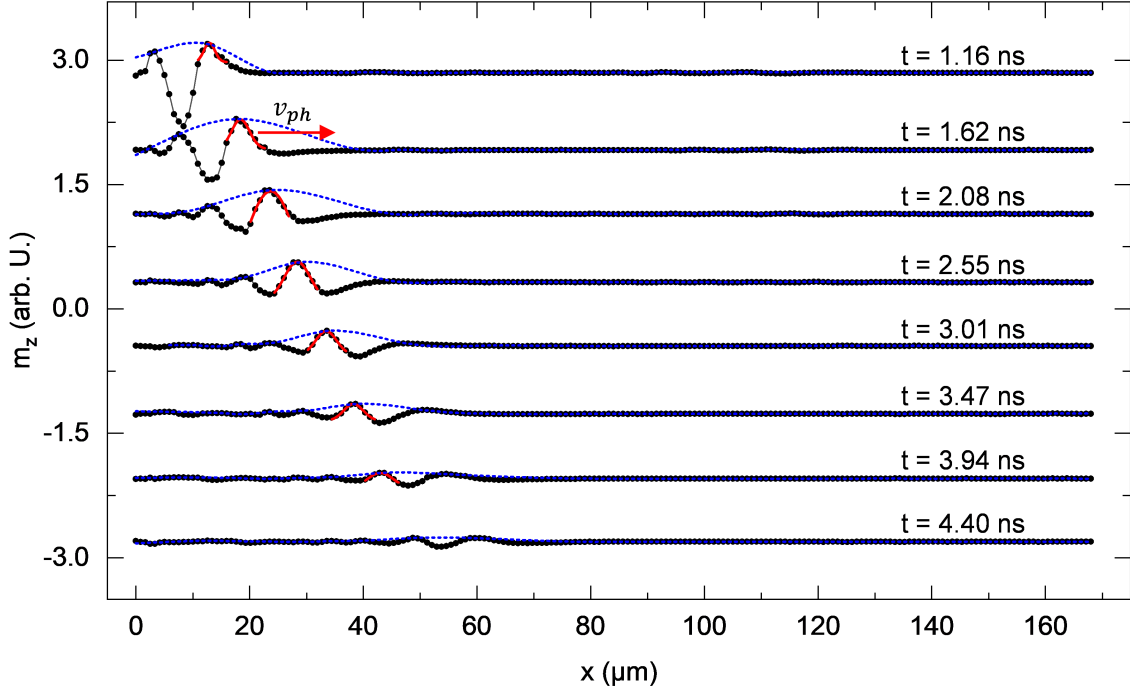
Figure 6.6: Extracted x-line plots for a sinc pulse excitation with a bandwidth $f_{bw} = 16$ GHz. A bias magnetic field of 20 mT was applied along the CPW (DE-like geometry). We observed a phase velocity of $v_{ph} = (9.29 \pm 0.23)$ km s^{-1} by fitting a positive peak with a Gaussian function (red solid lines). The blue dashed line represents the envelope for the propagating pulse. There was no pulse broadening observable for the observed time range. Data has been shifted vertically for clarity.

a difference in the amplitude of the pulse with respect to each side of the CPW. Fig. 6.7 (b) presents x-line plots for three different points in time, extracted from the data indicated by the white dashed lines in (a). The pulse amplitude is different concerning the two sides of the CPW. Consequently, this indicates a DE-like behavior, not only for continuous excited spin waves, but also for pulsed excitations of the magnetization dynamics.
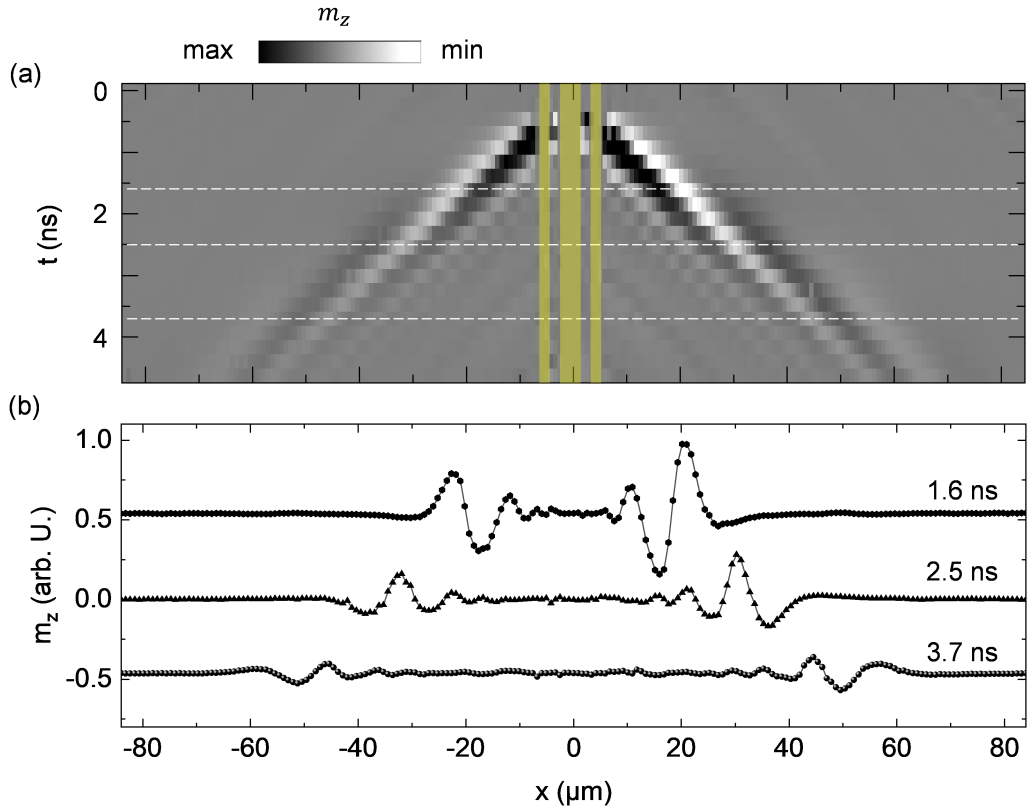
Figure 6.7: (a) Phase-resolved TR-MOKE measurement on both sides of the CPW (indicated by the yellow shape) for propagating magnetization dynamics over time. The magnetization dynamics were excited by a sinc pulse with a bandwidth of $f_{bw} = 16$ GHz and a bias magnetic field of $\mu_0 \mathbf{H_y} = 20$ mT (DE-like excitation). (b) Clarification of the DE-characteristic for a surface wave. The amplitude of the magnetization dynamics is different on either side of the CPW.

6.3   Damon-Eshbach Dispersion Acquisition by sinc pulse Excitation

To observe a DE-like dispersion relation, we need to be able to excite a rather broad, as well as an evenly distributed, amplitude in the frequency range of the corresponding rf-pulse. As already mentioned above, a sinc pulse function contains a rectangular-shaped frequency band and as a result we will use this function to observe the DE-like dispersion relation for the 60 nm Py film. The bandwidth f_{bw} of the sinc function was set

to be at the maximum of the AWG performance (20 GHz). Figure 6.8 (a) presents the spatial and temporal evolution of the sinc pulse, while a bias magnetic field of 4 mT was applied along the direction of the CPW (DE-like excitation). By applying a two-dimensional fast-Fourier-transformation (2D-FFT) to the experimental data, we observe both, the spatial as well as the temporal frequency components of the propagating sinc pulse. The frequency amplitude for the 2D-FFT is given in (b). Using the Python-based package TETRAX [77, 78] for calculating the dispersion relation for a 60 nm Py film at a bias magnetic field of 4 mT (blue dashed line in Fig. 6.8 (b)) demonstrates that the experimentally observed dispersion relation is in good agreement with the calculated dispersion relation. The minima observed in the FFT amplitude in Fig. 6.8 (b) can be explained by the excitation efficiency of the CPW, which was used to excite the magnetization dynamics within the Py film. This wave-vector selective excitation efficiency can be calculated by the FFT of the CPW's Oersted field distribution, shown in Fig. 6.8 (c). Considering the difference between a sinc function and a modified sinc function shows a suppression of the frequencies around zero for the modified sinc function, as shown in Fig. 6.1 (g) and (h). By using a modified sinc function, we can still take advantage of a rectangular-shaped frequency bandwidth but shifted to a center frequency away from the low frequencies. Figure 6.9 (a) presents a TR-MOKE measurement for a modified sinc pulse excitation with a bandwidth $f_{\text{bw}} = 5$ GHz centered at a frequency of $f_{\text{c}} = 7.5$ GHz at a bias magnetic field of 4 mT in the DE-geometry. By applying a 2D-FFT we observe again the frequency components in both, time and space. The result obtained by the 2D-FFT represents the dispersion relation for the 60 nm Py film, which is shown in Fig. 6.9 (b). Comparing the experimentally observed data (FFT ampl.), with the calculated dispersion relation (red dashed line), demonstrates that they are in good agreement with each other. Using a modified sinc function can indeed suppress a low-frequency excitation but allows an efficient excitation of a higher-frequency band. The excitation efficiency of the CPW, shown in Fig. 6.8 (c), is again observable in the 2D-FFT data, presented in Fig. 6.9 (b).

We have demonstrated the excitation of rf-pulses with different pulse shapes in a 60
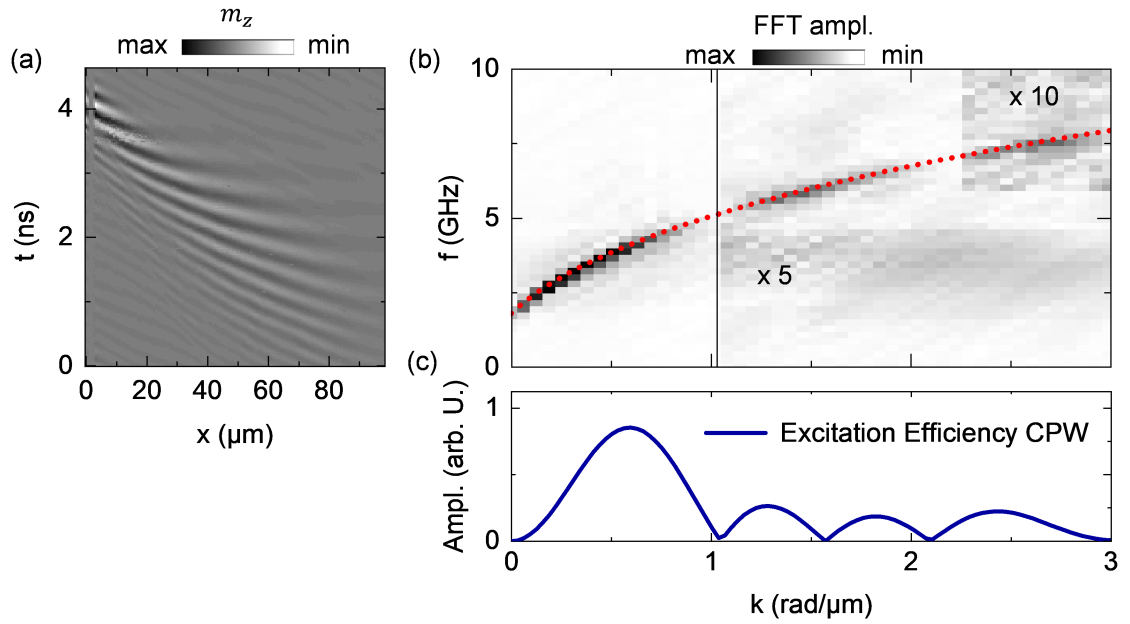
Figure 6.8: (a) Phase-resolved TR-MOKE measurement of a sinc pulse excitation over time. The bandwidth of the sinc pulse was $f_{bw} = 20$ GHz at a given bias magnetic field of $\mu_0 \mathbf{H} = 4$ mT. (b) Frequency over $\mathbf{k}$-vector extracted from the data shown in (a) after a two-dimensional FFT. The extracted data is in good agreement with the calculated dispersion relation (red dotted line). The minima observed in the FFT amplitude can be explained by the wave-vector selective excitation efficiency of the CPW, shown in (c).

nm Py film. The pulse propagation was measured as a function of time and space to analyze the pulse propagation characteristic for Gaussian, chirp and sinc pulse excited magnetization dynamics. A non-linear group velocity was observed due to the non-linear dispersion relation for DE-like magnetization dynamics. Extracting the phase velocity from the experimental data for the three pulse-shapes demonstrates that they are in the same order of magnitude, concerning each other. Furthermore, we demonstrated that the DE-like behavior is not only valid for continuous excited spin waves but also pulsed excited magnetization dynamics. This was done by analyzing the amplitude of a propagating sinc pulse on both sides of the CPW which was used to excite the pulsed magnetization dynamics. Moreover, we experimentally observed the DE-like dispersion
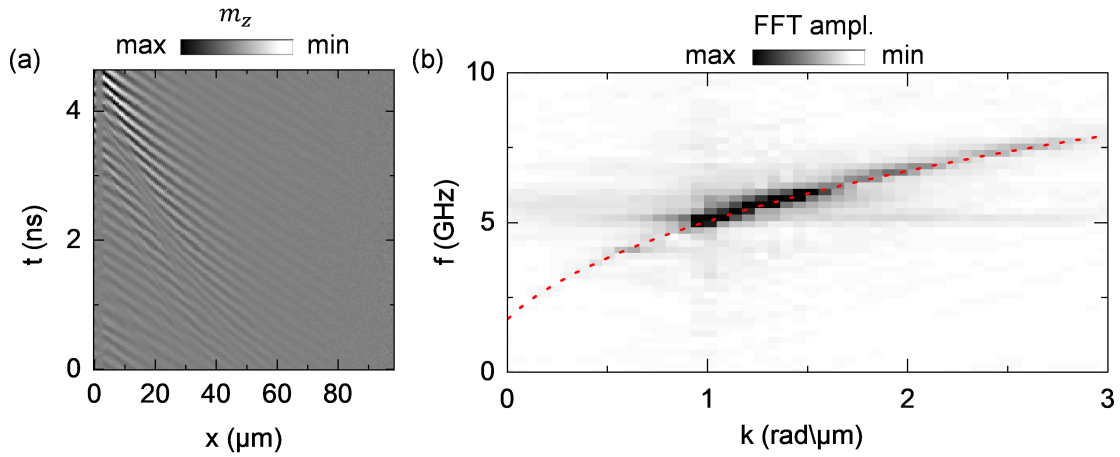
Figure 6.9: (a) Phase-resolved TR-MOKE measurement of a modified sinc pulse excitation over time. The bandwidth of the modified sinc pulse was $f_{\mathrm{bw}} = 5$ GHz centered at a center frequency of $f_{\mathrm{c}} = 7.5$ GHz at a given bias magnetic field of $\mu_0 \mathbf{H} = 4$ mT. (b) Frequency over **k**-vector extracted from the data shown in (a) after a two-dimensional FFT. The extracted data is in good agreement with the calculated dispersion relation (red dotted line). The lower frequencies are suppressed by using a modified sinc pulse.

relation by analyzing the propagation of a sinc pulse, as well as a modified sinc pulse, by using a table-top TR-MOKE system instead of using a TR-STXM, as presented in former work [98]. Comparing the experimental data with the calculated dispersion relation demonstrated that they are in good agreement with each other.

Chapter 7

Conclusion and Outlook

In the thesis presented here, we constructed two independent prototype TR-MOKE setups. A Mira laser system was used to provide femtosecond laser pulses to probe dynamic magnetization processes within the nanosecond time regime. The Mira laser was updated with a custom-made control system to precisely stabilize the length of the laser cavity. As a result, an accurate repetition rate of 80 MHz was achieved with the help of the proportional, integral, and differential (PID) regulated cavity control system. One of the TR-MOKE setups was designed with a custom-made cryostat to work at cryogenic temperatures. The outstanding features of this setup are that the piezo-slip-stick stage, as well as the objective lens, are placed within the cryostat. As a result, it was possible to comfortably attach a custom-made superconducting magnet to the setup which can provide an external magnetic field up to 2 T, normal to the sample surface. The second TR-MOKE setup is a prototype system that was designed to work at room temperature. A galvo-galvo-scanning system in combination with a telecentric lens system was used to scan a focused laser across the sample surface instead of using a piezo-controlled xy-positioning stage to move the sample with respect to the laser focus. We first demonstrated that such a galvo-galvo-scanning system in combination with a telecentric lens system can be used to probe magneto-optic sensitive quantities like the MOKE. As the sample is allowed to rest at a given position during the measurement of a two-dimensional MOKE image, experimentally required electrical or mechanical connec-

tions can be securely mounted to avoid any influence on the experiment. Investigating magnetic nanoparticles and nanowires is a topical area in medical research [159, 160]. The magnetization of fluid specimens, or magnetic particles within a solution, can potentially be investigated with the help of the galvo-galvo scanning system, as no motion of the sample relative to the laser is necessary to achieve the two-dimensional image, which would otherwise change the arrangement of the particles within the solution. A confocal option can easily be added to the galvo-galvo system presented in this thesis, to give rise to an added functionality of depth sensitivity, useful for liquid specimens. Moreover, the galvo-galvo system could be combined with a NV-center based magnetometer to potentially achieve both, a TR-MOKE signal as well as the fluorescence signal coming from the NV-center, at the very same time.

With the help of both TR-MOKE setups, we investigate the influence of an anti-dot diffraction grating on the propagation behavior for three spin wave geometries, i.e., Damon-Eshbach, Backward Volume, and Forward Volume spin waves. We found a transmission stop band at the diffraction grating for DE-spin waves due to the hybridization of the $n = 0$ and $n = 1$ PSSWs. As a result, the spin wave propagation can be controlled locally by a suitable choice of the external magnetic field. Magnonic logic gates, which are based on the binary system, i.e., zero (0) and one (1) states, can be supported by this finding. Moreover, we were able to enter a caustic-like spin wave regime with the ability to control the k-vector distribution and in turn, the direction of the spin wave beam. With this, we have demonstrated that we can control the position of a high intensity spin wave beam (logical one (1) state) with respect to areas with low or even no spin wave intensity (logical zero (0) state).

Potential magnonic devices will most likely contain metallic contacts for sending and reading the information, carried by spin waves. Normal metals in proximity to a ferrimagnetic YIG film have been investigated to gain a deeper understanding concerning the interaction of spin waves with NMs. We found that NM structures with a thickness of about 100 nm can be used to attenuate the spin wave amplitude within a 200 nm thick YIG film. Moreover, by investigating a variety of NMs with different thicknesses,

we found that not only is the spin wave amplitude affected by the NM, but also the wave-vector and in turn the phase of the spin wave. A non-reciprocity for magnetostatic surface waves was found by observing the dispersion of propagating spin waves directly through the NMs. We found that the size of the anticrossing gap in the vicinity of the hybridization of the $n = 0$ and $n = 1$ PSSW can be increased due to the proximity of the NM on top of the YIG film. Using this effect leads to the ability to adjust the magnetic field range in which the hybridization occurs and with this, to tune the transmission stop band presented by the antidot grating simply by depositing NM on top of the area between two antidots. Moreover, by using the effect of the increased hybridization gap, we were able to achieve a local stop of the spin wave propagation only at the metallized areas, while the spin wave was still able to propagate within the pure YIG. As a result, a binary system, already demonstrated with the antidot grating, can be achieved by simply depositing a NM structure on top of a YIG film. In addition to the increased hybridization gap, we demonstrated an optic-like manipulation of the spin waves by using triangular-shaped NM structures. By slightly changing the direction of the external magnetic field with respect to the triangular-shaped NM structures, we achieved control over the direction of the spin wave diffraction pattern, and with this the low intensity spin wave area.

In Chapter 6, we presented the propagation behavior of a pulsed excitation of the magnetization dynamics within a 60 nm Py film. We have analyzed the pulse width as well as the group velocity of a Gaussian, chirp, and sinc pulse excitation. As a result, we found the Gaussian pulse to give the most confined pulse shape in both, space and time. The group velocity for all three pulse shapes was found to be on the same order of magnitude of about $10\,\mathrm{km\,s^{-1}}$. Moreover, we found the conversion from a down-chirped pulse into an up-chirped pulse within the Py film due to the normal behavior of the dispersion. A standard approach to characterize the dynamic behavior of magnetic materials is to measure the dispersion relation. We presented a method to obtain the dispersion relation of a magnetic material using a simple, tabletop TR-MOKE system, instead of the more complex, and certainly more expensive method of

TR-STXM only available at large-scale synchrotron facilities. The DE dispersion was achieved by probing the propagation of a sinc pulse, containing a frequency bandwidth of 20 GHz, in both, space and time with a subsequent 2D-FFT. As a consequence, we obtained the frequency components in space and time for the propagating sinc pulse which resulted in the DE dispersion relation. Using pulsed magnetization for potential information carriers accompanies a selectivity of the accessible frequency bandwidth. We demonstrated the selectivity of the excitation frequency bandwidth by observing the dispersion using the same method as for the sinc pulse, but for a modified sinc pulse excitation with a frequency bandwidth of 5 GHz, centered at a center frequency of 7.5 GHz. The dispersion showed a clear suppression of frequencies below 5 GHz which demonstrated a significant frequency selectivity.

In conclusion, the focus of this thesis was an investigation of the local manipulation of the spin wave propagation by the help of two prototype TR-MOKE setups. Especially the local manipulation of the spin wave propagation, and as a result a binary behavior, is of central importance for engineering future magnonic devices.

Bibliography

[1] F. Bloch, "Zur theorie des ferromagnetismus," *Z. Phys.*, vol. 61, no. 3, pp. 206–219, 1930.

[2] F. Bloch, *Zur theorie des austauschproblems und der remanenzerscheinung der ferromagnetika*, pp. 295–335. Berlin, Heidelberg: Springer Berlin Heidelberg, 1932.

[3] T. Holstein and H. Primakoff, "Field dependence of the intrinsic domain magnetization of a ferromagnet," *Phys. Rev.*, vol. 58, pp. 1098–1113, Dec 1940.

[4] F. J. Dyson, "General theory of spin-wave interactions," *Phys. Rev.*, vol. 102, pp. 1217–1230, Jun 1956.

[5] C. Herring and C. Kittel, "On the theory of spin waves in ferromagnetic media," *Phys. Rev.*, vol. 81, pp. 869–880, Mar 1951.

[6] C. Kittel, "Interaction of spin waves and ultrasonic waves in ferromagnetic crystals," *Phys. Rev.*, vol. 110, pp. 836–841, May 1958.

[7] J. H. E. Griffiths, "Anomalous high-frequency resistance of ferromagnetic metals," *Nature*, vol. 158, no. 4019, pp. 670–671, 1946.

[8] V. V. Kruglyak, S. O. Demokritov, and D. Grundler, "Magnonics," *Phys. D: Appl. Phys.*, vol. 43, p. 260301, jun 2010.

[9] A. Barman, G. Gubbiotti, S. Ladak, A. O. Adeyeye, M. Krawczyk, J. Gräfe, *et al.*, "The 2021 magnonics roadmap," *J. Condens. Matter Phys.*, vol. 33, p. 413001, aug 2021.

[10] L. Brillouin, *Wave Propagation in Periodic Structures: Electric Filters and Crystal Lattices 1st edn.* New York: Dover, 1948.

[11] J. D. Joannopoulos, S. G. Johnson, J. N. Winn, and R. D. Meade, *Photonic Crystals.* Princeton University Press, 2008.

[12] C. G. Sykes, J. D. Adam, and J. H. Collins, "Magnetostatic wave propagation in a periodic structure," *Appl. Phys. Lett.*, vol. 29, no. 6, pp. 388–391, 1976.

[13] J. P. Parekh and H. S. Tuan, "Magnetostatic surface wave reflectivity of a shallow groove on a yig film," *Appl. Phys. Lett.*, vol. 30, no. 12, pp. 667–669, 1977.

[14] J. O. Vasseur, L. Dobrzynski, B. Djafari-Rouhani, and H. Puszkarski, "Magnon band structure of periodic composites," *Phys. Rev. B*, vol. 54, pp. 1043–1049, Jul 1996.

[15] Y. V. Gulyaev and A. A. Nikitov, "Magnonic crystals and spin waves in periodic structures," *Doklady Physics*, vol. 46, no. 10, pp. 687–689, 2001.

[16] H. Puszkarski and M. Krawczyk, "Magnonic crystals — the magnetic counterpart of photonic crystals," in *Interfacial Effects and Novel Properties of Nanomaterials*, vol. 94 of *Solid State Phenomena*, pp. 125–134, Trans Tech Publications Ltd, 6 2003.

[17] V. Kruglyak and A. Kuchko, "Damping of spin waves in a real magnonic crystal," *J. Magn. Magn. Mater.*, vol. 272-276, pp. 302–303, 2004. Proceedings of the International Conference on Magnetism (ICM 2003).

[18] S. A. Wolf, D. D. Awschalom, R. A. Buhrman, J. M. Daughton, S. von Molnár, M. L. Roukes, A. Y. Chtchelkanova, and D. M. Treger, "Spintronics: A spin-based electronics vision for the future," *Science*, vol. 294, no. 5546, pp. 1488–1495, 2001.

[19] D. Grundler, "Spintronics," *Physics World*, vol. 15, p. 39, apr 2002.

[20] S. Neusser and D. Grundler, "Magnonics: Spin waves on the nanoscale," *Advanced Materials*, vol. 21, no. 28, pp. 2927–2932, 2009.

[21] V. E. Demidov, B. Hillebrands, S. O. Demokritov, M. Laufenberg, and P. P. Freitas, "Two-dimensional patterns of spin-wave radiation by rectangular spin-valve elements," *J. Appl. Phys.*, vol. 97, no. 10, p. 10A717, 2005.

[22] V. E. Demidov, S. O. Demokritov, D. Birt, B. O'Gorman, M. Tsoi, and X. Li, "Radiation of spin waves from the open end of a microscopic magnetic-film waveguide," *Phys. Rev. B*, vol. 80, p. 014429, Jul 2009.

[23] J. R. Eshbach, "Spin-wave propagation and the magnetoelastic interaction in yttrium iron garnet," *Phys. Rev. Lett.*, vol. 8, pp. 357–359, May 1962.

[24] M. Bailleul, D. Olligs, C. Fermon, and S. O. Demokritov, "Spin waves propagation and confinement in conducting films at the micrometer scale," *Europhys. Let.*, vol. 56, p. 741, dec 2001.

[25] A. A. Serga, S. O. Demokritov, B. Hillebrands, and A. N. Slavin, "Self-generation of two-dimensional spin-wave bullets," *Phys. Rev. Lett.*, vol. 92, p. 117203, Mar 2004.

[26] S. Tamaru, J. A. Bain, R. J. M. van de Veerdonk, T. M. Crawford, M. Covington, and M. H. Kryder, "Measurement of magnetostatic mode excitation and relaxation in permalloy films using scanning kerr imaging," *Phys. Rev. B*, vol. 70, p. 104416, Sep 2004.

[27] V. K. Dugaev, P. Bruno, B. Canals, and C. Lacroix, "Berry phase of magnons in textured ferromagnets," *Phys. Rev. B*, vol. 72, p. 024456, Jul 2005.

[28] S. Yang, Z. Song, and C. P. Sun, "Beam splitter for spin waves in quantum spin network," *Eur. Phys. J. B*, vol. 52, no. 3, pp. 377–381, 2006.

[29] S. Choi, K.-S. Lee, and S.-K. Kim, "Spin-wave interference," *Appl. Phys. Lett.*, vol. 89, no. 6, p. 062501, 2006.

[30] D. R. Birt, B. O'Gorman, M. Tsoi, X. Li, V. E. Demidov, and S. O. Demokritov, "Diffraction of spin waves from a submicrometer-size defect in a microwaveguide," *Appl. Phys. Lett.*, vol. 95, no. 12, p. 122510, 2009.

[31] K. Perzlmaier, G. Woltersdorf, and C. H. Back, "Observation of the propagation and interference of spin waves in ferromagnetic thin films," *Phys. Rev. B*, vol. 77, p. 054425, Feb 2008.

[32] F. Goedsche, "Reflection and refraction of spin waves," *Phys Status Solidi (b)*, vol. 39, no. 1, pp. K29–K33, 1970.

[33] J. Gouzerh, A. Stashkevich, N. Kovshikov, V. Matyushev, and J. Desvignes, "Reflection of magnetostatic waves from a laser-annealed grating in a garnet film," *Journal of Magnetism and Magnetic Materials*, vol. 101, no. 1, pp. 189–190, 1991.

[34] Y. I. Gorobets and S. A. Reshetnyak, "Reflection and refraction of spin waves in uniaxial magnets in the geometrical-optics approximation," *Techn. Phys.*, vol. 43, no. 2, pp. 188–191, 1998.

[35] S.-K. Kim, S. Choi, K.-S. Lee, D.-S. Han, D.-E. Jung, and Y.-S. Choi, "Negative refraction of dipole-exchange spin waves through a magnetic twin interface in restricted geometry," *Appl. Phys. Lett.*, vol. 92, no. 21, p. 212501, 2008.

[36] J. Stigloher, M. Decker, H. S. Körner, K. Tanabe, T. Moriyama, T. Taniguchi, H. Hata, M. Madami, G. Gubbiotti, K. Kobayashi, T. Ono, and C. H. Back, "Snell's law for spin waves," *Phys. Rev. Lett.*, vol. 117, p. 037204, Jul 2016.

[37] F. Morgenthaler, "Magnetostatic spin wave focusing and defocusing in cylindrically symmetric non-laplacian magnetic fields," *IEEE Trans. Magn.*, vol. 8, no. 3, pp. 550–551, 1972.

[38] M. Bauer, C. Mathieu, S. O. Demokritov, B. Hillebrands, P. A. Kolodin, S. Sure, *et al.*, "Direct observation of two-dimensional self-focusing of spin waves in magnetic films," *Phys. Rev. B*, vol. 56, pp. R8483–R8486, Oct 1997.

[39] R. Khomeriki, "Self-focusing magnetostatic beams in thin magnetic films," *Eur. Phys. J. B*, vol. 41, no. 2, pp. 219–222, 2004.

[40] V. E. Demidov, S. O. Demokritov, K. Rott, P. Krzysteczko, and G. Reiss, "Self-focusing of spin waves in permalloy microstripes," *Appl. Phys. Lett.*, vol. 91, no. 25, p. 252504, 2007.

[41] V. E. Demidov, S. O. Demokritov, K. Rott, P. Krzysteczko, and G. Reiss, "Mode interference and periodic self-focusing of spin waves in permalloy microstripes," *Phys. Rev. B*, vol. 77, p. 064406, Feb 2008.

[42] V. E. Demidov, J. Jersch, K. Rott, P. Krzysteczko, G. Reiss, and S. O. Demokritov, "Nonlinear propagation of spin waves in microscopic magnetic stripes," *Phys. Rev. Lett.*, vol. 102, p. 177207, Apr 2009.

[43] A. V. Chumak, V. Vasyuchka, A. Serga, and B. Hillebrands, "Magnon spintronics," *Nat. Phys.*, vol. 11, no. 6, pp. 453–461, 2015.

[44] K.-S. Lee and S.-K. Kim, "Conceptual design of spin wave logic gates based on a mach–zehnder-type spin wave interferometer for universal logic functions," *J. Appl. Phys.*, vol. 104, no. 5, p. 053909, 2008.

[45] H. Qin, R. B. Holländer, L. Flajšman, F. Hermann, R. Dreyer, G. Woltersdorf, and S. van Dijken, "Nanoscale magnonic fabry-pérot resonator for low-loss spin-wave manipulation," *Nat. Commun.*, vol. 12, no. 1, p. 2293, 2021.

[46] T. Schneider, A. A. Serga, B. Leven, B. Hillebrands, R. L. Stamps, and M. P. Kostylev, "Realization of spin-wave logic gates," *Appl. Phys. Lett.*, vol. 92, no. 2, p. 022505, 2008.

[47] Q. Wang, P. Pirro, R. Verba, A. Slavin, B. Hillebrands, and A. V. Chumak, "Reconfigurable nanoscale spin-wave directional coupler," *Sci. Adv.*, vol. 4, no. 1, p. e1701517, 2018.

[48] Q. Wang, A. Hamadeh, R. Verba, V. Lomakin, M. Mohseni, B. Hillebrands, A. V. Chumak, and P. Pirro, "A nonlinear magnonic nano-ring resonator," *npj Computational Materials*, vol. 6, p. 192, Dec. 2020.

[49] A. V. Sadovnikov, C. S. Davies, S. V. Grishin, V. V. Kruglyak, D. V. Romanenko, Y. P. Sharaevskii, and S. A. Nikitov, "Magnonic beam splitter: The building block of parallel magnonic circuitry," *Appl. Phys. Lett.*, vol. 106, no. 19, p. 192406, 2015.

[50] T. Taniguchi and C. H. Back, "Mode selective excitation of spin waves," *Appl. Phys. Lett.*, vol. 120, no. 3, p. 032402, 2022.

[51] A. V. Chumak, A. A. Serga, and B. Hillebrands, "Magnonic crystals for data processing," *Phys. D: Appl. Phys.*, vol. 50, p. 244001, may 2017.

[52] W. A. Yager and R. M. Bozorth, "Ferromagnetic resonance at microwave frequencies," *Phys. Rev.*, vol. 72, pp. 80–81, Jul 1947.

[53] C. Kittel, "On the theory of ferromagnetic resonance absorption," *Phys. Rev.*, vol. 73, pp. 155–161, Jan 1948.

[54] A. G. Gurevich, *Magnetization oscillations and waves.* CRC Press, 1996.

[55] G. S. Abo, Y.-K. Hong, J. Park, J. Lee, W. Lee, and B.-C. Choi, "Definition of magnetic exchange length," *IEEE Trans. Magn.*, vol. 49, no. 8, pp. 4937–4939, 2013.

[56] J. Stöhr and H. C. Siegmann, *Magnetism (Springer Series in Solid-State Sciences).* Springer, 2006.

[57] J. M. D. Coey, *Magnetism and magnetic materials.* Cambridge University Press, 2010.

[58] L. D. Landau, "18 - on the theory of the dispersion of magnetic permeability in ferromagnetic bodies," in *Collected Papers of L.D. Landau* (D. TER HAAR, ed.), pp. 101–114, Pergamon, 1965.

[59] C. Kittel, *Einführung in die Festkörperphysik.* Oldenbourg, 2002.

[60] K. J. Harte, "Theory of magnetization ripple in ferromagnetic films," *J. Appl. Phys.*, vol. 39, no. 3, pp. 1503–1524, 1968.

[61] B. A. Kalinikos and A. N. Slavin, "Theory of dipole-exchange spin wave spectrum for ferromagnetic films with mixed exchange boundary conditions," *Journal of Physics C: Solid State Physics*, vol. 19, pp. 7013–7033, dec 1986.

[62] P. Dai, H. Y. Hwang, J. Zhang, J. A. Fernandez-Baca, S.-W. Cheong, C. Kloc, Y. Tomioka, and Y. Tokura, "Magnon damping by magnon-phonon coupling in manganese perovskites," *Phys. Rev. B*, vol. 61, pp. 9553–9557, Apr 2000.

[63] S. Streib, N. Vidal-Silva, K. Shen, and G. E. W. Bauer, "Magnon-phonon interactions in magnetic insulators," *Phys. Rev. B*, vol. 99, p. 184442, May 2019.

[64] J. Zhang, M. Chen, J. Chen, K. Yamamoto, H. Wang, M. Hamdi, *et al.*, "Long decay length of magnon-polarons in BiFeO3/La0.67Sr0.33MnO3 heterostructures," *Nat. Commun.*, vol. 12, no. 1, p. 7258, 2021.

[65] K. Zakeri, J. Lindner, I. Barsukov, R. Meckenstock, M. Farle, U. von Hörsten, H. Wende, W. Keune, J. Rocker, S. S. Kalarickal, K. Lenz, W. Kuch, K. Baberschke, and Z. Frait, "Spin dynamics in ferromagnets: Gilbert damping and two-magnon scattering," *Phys. Rev. B*, vol. 76, p. 104416, Sep 2007.

[66] S. M. Rezende, A. Azevedo, M. A. Lucena, and F. M. de Aguiar, "Anomalous spin-wave damping in exchange-biased films," *Phys. Rev. B*, vol. 63, p. 214418, May 2001.

[67] A. Azevedo, A. B. Oliveira, F. M. de Aguiar, and S. M. Rezende, "Extrinsic contributions to spin-wave damping and renormalization in thin $ni_{50}fe_{50}$ films," *Phys. Rev. B*, vol. 62, pp. 5331–5333, Sep 2000.

[68] E. Kriezis, T. Tsiboukis, S. Panas, and J. Tegopoulos, "Eddy currents: theory and applications," *Proc. IEEE*, vol. 80, no. 10, pp. 1559–1589, 1992.

[69] I. Bertelli, B. G. Simon, T. Yu, J. Aarts, G. E. W. Bauer, Y. M. Blanter, and T. van der Sar, "Imaging spin-wave damping underneath metals using electron spins in diamond," *Advanced Quantum Technologies*, vol. 4, no. 12, p. 2100094, 2021.

[70] R. Urban, G. Woltersdorf, and B. Heinrich, "Gilbert damping in single and multilayer ultrathin films: Role of interfaces in nonlocal spin dynamics," *Phys. Rev. Lett.*, vol. 87, p. 217204, Nov 2001.

[71] S. Mizukami, Y. Ando, and T. Miyazaki, "Ferromagnetic resonance linewidth for NM/80NiFe/NM films (NM=Cu, Ta, Pd and Pt)," *J. Magn. Magn. Mater.*, vol. 226-230, pp. 1640–1642, 2001. Proceedings of the International Conference on Magnetism (ICM 2000).

[72] Y. Tserkovnyak, A. Brataas, and G. E. W. Bauer, "Spin pumping and magnetization dynamics in metallic multilayers," *Phys. Rev. B*, vol. 66, p. 224403, Dec 2002.

[73] Y. Tserkovnyak, A. Brataas, and G. E. W. Bauer, "Enhanced gilbert damping in thin ferromagnetic films," *Phys. Rev. Lett.*, vol. 88, p. 117601, Feb 2002.

[74] A. Kapelrud and A. Brataas, "Spin pumping and enhanced gilbert damping in thin magnetic insulator films," *Phys. Rev. Lett.*, vol. 111, p. 097602, Aug 2013.

[75] F. D. Czeschka, L. Dreher, M. S. Brandt, M. Weiler, M. Althammer, I.-M. Imort, G. Reiss, A. Thomas, W. Schoch, W. Limmer, H. Huebl, R. Gross, and S. T. B. Goennenwein, "Scaling behavior of the spin pumping effect in ferromagnet-platinum bilayers," *Phys. Rev. Lett.*, vol. 107, p. 046601, Jul 2011.

[76] Y. Henry, O. Gladii, and M. Bailleul, "Propagating spin-wave normal modes: A dynamic matrix approach using plane-wave demagnetizating tensors," 2016.

[77] L. Körber, G. Quasebarth, A. Otto, and A. Kákay, "Finite-element dynamic-matrix approach for spin-wave dispersions in magnonic waveguides with arbitrary cross section," *AIP Advances*, vol. 11, no. 9, p. 095006, 2021.

[78] L. Körber, G. Quasebarth, A. Hempel, F. Zahn, A. Otto, E. Westphal, R. Hertel, and A. Kakay, "Tetrax: Finite-element micromagnetic-modeling package," 2022.

[79] S. Seshadri, "Surface magnetostatic modes of a ferrite slab," *Proc. IEEE*, vol. 58, pp. 506–507, March 1970.

[80] T. Yukawa, J. ichi Yamada, K. Abe, and J. ichi Ikenoue, "Effects of metal on the dispersion relation of magnetostatic surface waves," *Japanese J. Appl. Phys.*, vol. 16, p. 2187, dec 1977.

[81] W. L. Bongianni, "Magnetostatic propagation in a dielectric layered structure," *J. Appl. Phys.*, vol. 43, no. 6, pp. 2541–2548, 1972.

[82] J. Maxwell, "On physical lines of force," *Philosophical Magazine*, vol. 90, no. sup1, pp. 11–23, 2010.

[83] D. J. Griffiths, *Introduction to Electrodynamics*. Cambridge University Press, 2017.

[84] E. Hecht, P. E. P. E. Inc., and K. Lippert, *Optik*. de Gruyter GmbH, Walter, 2018.

[85] J. Kerr, "Xliii. on rotation of the plane of polarization by reflection from the pole of a magnet," *Lond. Edinb. Dublin philos. mag. j. sci.*, vol. 3, no. 19, pp. 321–343, 1877.

[86] W. Rave, R. Schäfer, and A. Hubert, "Quantitative observation of magnetic domains with the magneto-optical kerr effect," *J. Magn. Magn. Mater.*, vol. 65, no. 1, pp. 7–14, 1987.

[87] R. Schäfer, *Handbook of Magnetism and Advanced Magnetic Materials*, ch. Investigation of Domains and Dynamics of Domain Walls by the Magneto-optical Kerr-effect. John Wiley & Sons, Ltd, 2007.

[88] R. Schäfer, "Magneto-optical domain studies in coupled magnetic multilayers," *J. Magn. Magn. Mater.*, vol. 148, no. 1, pp. 226–231, 1995.

[89] R. Schäfer, P. M. Oppeneer, A. V. Ognev, A. S. Samardak, and I. V. Soldatov, "Analyzer-free, intensity-based, wide-field magneto-optical microscopy," *Appl. Phys. Rev.*, vol. 8, no. 3, p. 031402, 2021.

[90] I. V. Soldatov and R. Schäfer, "Advanced moke magnetometry in wide-field kerr-microscopy," *J. Appl. Phys.*, vol. 122, no. 15, p. 153906, 2017.

[91] C. Mudivarthi, S.-M. Na, R. Schaefer, M. Laver, M. Wuttig, and A. B. Flatau, "Magnetic domain observations in fe–ga alloys," *J. Magn. Magn. Mater.*, vol. 322, no. 14, pp. 2023–2026, 2010.

[92] T. Sebastian, K. Schultheiss, B. Obry, B. Hillebrands, and H. Schultheiss, "Microfocused brillouin light scattering: imaging spin waves at the nanoscale," *Front. Phys.*, vol. 3, 2015.

[93] O. Büttner, M. Bauer, A. Rueff, S. Demokritov, B. Hillebrands, A. Slavin, M. Kostylev, and B. Kalinikos, "Space- and time-resolved brillouin light scattering from nonlinear spin-wave packets," *Ultrasonics*, vol. 38, no. 1, pp. 443–449, 2000.

[94] S. Demokritov, B. Hillebrands, and A. Slavin, "Brillouin light scattering studies of confined spin waves: linear and nonlinear confinement," *Phys. Rep.*, vol. 348, no. 6, pp. 441–489, 2001.

[95] M. Baumgartner, K. Garello, J. Mendil, C. O. Avci, E. Grimaldi, C. Murer, *et al.*, "Spatially and time-resolved magnetization dynamics driven by spin-orbit torques," *Nat. Nanotechnol.*, vol. 12, no. 10, pp. 980–986, 2017.

[96] Y. Acremann, J. P. Strachan, V. Chembrolu, S. D. Andrews, T. Tyliszczak, J. A. Katine, *et al.*, "Time-resolved imaging of spin transfer switching: Beyond the macrospin concept," *Phys. Rev. Lett.*, vol. 96, p. 217202, May 2006.

[97] M. Bolte, G. Meier, B. Krüger, A. Drews, R. Eiselt, L. Bocklage, S. Bohlens, T. Tyliszczak, A. Vansteenkiste, *et al.*, "Time-resolved x-ray microscopy of spin-torque-induced magnetic vortex gyration," *Phys. Rev. Lett.*, vol. 100, p. 176601, Apr 2008.

[98] N. Träger, F. Groß, J. Förster, K. Baumgaertl, H. Stoll, M. Weigand, G. Schütz, D. Grundler, and J. Gräfe, "Single shot acquisition of spatially resolved spin wave dispersion relations using x-ray microscopy," *Sci. Rep.*, vol. 10, oct 2020.

[99] H. Qin, R. B. Holländer, L. Flajšman, F. Hermann, R. Dreyer, G. Woltersdorf, and S. van Dijken, "Nanoscale magnonic fabry-pérot resonator for low-loss spin-wave manipulation," *Nat. Commun.*, vol. 12, no. 1, p. 2293, 2021.

[100] Y. Au, T. Davison, E. Ahmad, P. S. Keatley, R. J. Hicken, and V. V. Kruglyak, "Excitation of propagating spin waves with global uniform microwave fields," *Appl. Phys. Lett.*, vol. 98, no. 12, p. 122506, 2011.

[101] H. G. Bauer, J.-Y. Chauleau, G. Woltersdorf, and C. H. Back, "Coupling of spin-wave modes in wire structures," *Appl. Phys. Lett.*, vol. 104, no. 10, p. 102404, 2014.

[102] M. Farle, T. Silva, and G. Woltersdorf, *Magnetic Nanostructures*, ch. Spin Dynamics in the Time and Frequency Domain, pp. 37–83. Berlin, Heidelberg: Springer Berlin Heidelberg, Jan 2013.

[103] G. Schütz, W. Wagner, W. Wilhelm, P. Kienle, R. Zeller, R. Frahm, and G. Materlik, "Absorption of circularly polarized x rays in iron," *Phys. Rev. Lett.*, vol. 58, pp. 737–740, Feb 1987.

[104] W. Zong, "New solution for fast axial scanning in fluorescence microscopy," *Light: Science & Applications*, vol. 9, no. 1, p. 199, 2020.

[105] J. Lin, Z. Cheng, W. Gan, and M. Cui, "Jitter suppression for resonant galvo based high-throughput laser scanning systems," *Opt. Express*, vol. 28, pp. 26414–26420, Aug 2020.

[106] R. Dreyer, N. Liebing, E. Edwards, and G. Woltersdorf, "Local spin-wave dispersion and damping in thin yttrium-iron-garnet films," *Appl. Phys. Lett.*, 2018-03-14 00:03:00 2018.

[107] J. R. Eshbach and R. W. Damon, "Surface magnetostatic modes and surface spin waves," *Phys. Rev.*, vol. 118, pp. 1208–1210, Jun 1960.

[108] R. Damon and J. Eshbach, "Magnetostatic modes of a ferromagnet slab," *Journal of Physics and Chemistry of Solids*, vol. 19, no. 3, pp. 308–320, 1961.

[109] C. Riedel, T. Taniguchi, L. Körber, A. Kakay, and C. H. Back, "Hybridization-induced spin-wave transmission stop band within a 1d diffraction grating," *Adv. Phys. Res.*, 2023.

[110] A. Papp, W. Porod, and G. Csaba, "Nanoscale neural network using non-linear spin-wave interference," *Nat. Commun.*, vol. 12, no. 1, p. 6422, 2021.

[111] O. Büttner, M. Bauer, S. O. Demokritov, B. Hillebrands, Y. S. Kivshar, V. Grimalsky, Y. Rapoport, and A. N. Slavin, "Linear and nonlinear diffraction of dipolar spin waves in yttrium iron garnet films observed by space- and time-resolved brillouin light scattering," *Phys. Rev. B*, vol. 61, pp. 11576–11587, May 2000.

[112] T. Schneider, A. A. Serga, A. V. Chumak, C. W. Sandweg, S. Trudel, S. Wolff, M. P. Kostylev, V. S. Tiberkevich, A. N. Slavin, and B. Hillebrands, "Non-diffractive subwavelength wave beams in a medium with externally controlled anisotropy," *Phys. Rev. Lett.*, vol. 104, p. 197203, May 2010.

[113] R. Gieniusz, P. Gruszecki, M. Krawczyk, U. Guzowska, A. Stognij, and A. Maziewski, "The switching of strong spin wave beams in patterned garnet films," *Sci. Rep.*, vol. 7, no. 1, p. 8771, 2017.

[114] M. A. Morozova, S. V. Grishin, A. V. Sadovnikov, D. V. Romanenko, Y. P. Sharaevskii, and S. A. Nikitov, "Band gap control in a line-defect magnonic crystal waveguide," *Appl. Phys. Lett.*, vol. 107, no. 24, p. 242402, 2015.

[115] Y. Shiota, S. Funada, R. Hisatomi, T. Moriyama, and T. Ono, "Imaging of caustic-like spin wave beams using optical heterodyne detection," *Appl. Phys. Lett.*, vol. 116, no. 19, p. 192411, 2020.

[116] R. W. Damon and J. R. Eshbach, "Magnetostatic modes of a ferromagnetic slab," *J. Appl. Phys.*, vol. 31, no. 5, pp. S104–S105, 1960.

[117] S. Mansfeld, J. Topp, K. Martens, J. N. Toedt, W. Hansen, D. Heitmann, and S. Mendach, "Spin wave diffraction and perfect imaging of a grating," *Phys. Rev. Lett.*, vol. 108, p. 047204, Jan 2012.

[118] R. Gieniusz, V. D. Bessonov, U. Guzowska, A. I. Stognii, and A. Maziewski, "An antidot array as an edge for total non-reflection of spin waves in yttrium iron garnet films," *Appl. Phys. Lett.*, vol. 104, no. 8, p. 082412, 2014.

[119] M. Golebiewski, P. Gruszecki, M. Krawczyk, and A. E. Serebryannikov, "Spin-wave talbot effect in a thin ferromagnetic film," *Phys. Rev. B*, vol. 102, p. 134402, Oct 2020.

[120] A. Vansteenkiste, J. Leliaert, M. Dvornik, M. Helsen, F. Garcia-Sanchez, and B. Van Waeyenberge, "The design and verification of mumax3," *AIP Advances*, vol. 4, no. 10, p. 107133, 2014.

[121] J.-V. Kim, R. L. Stamps, and R. E. Camley, "Spin wave power flow and caustics in ultrathin ferromagnets with the dzyaloshinskii-moriya interaction," *Phys. Rev. Lett.*, vol. 117, p. 197204, Nov 2016.

[122] M. Grassi, M. Geilen, D. Louis, M. Mohseni, T. Brächer, M. Hehn, D. Stoeffler, M. Bailleul, P. Pirro, and Y. Henry, "Slow-wave-based nanomagnonic diode," *Phys. Rev. Applied*, vol. 14, p. 024047, Aug 2020.

[123] L. Körber, R. Verba, J. A. Otálora, V. Kravchuk, J. Lindner, J. Fassbender, and A. Kákay, "Curvilinear spin-wave dynamics beyond the thin-shell approximation: Magnetic nanotubes as a case study," *Phys. Rev. B*, vol. 106, p. 014405, Jul 2022.

[124] L. Novotny, "Strong coupling, energy splitting, and level crossings: A classical perspective," *Am. J. Phys.*, vol. 78, no. 11, pp. 1199–1202, 2010.

[125] R. Dreyer, N. Liebing, E. R. J. Edwards, A. Müller, and G. Woltersdorf, "Spin-wave localization and guiding by magnon band structure engineering in yttrium iron garnet," *Phys. Rev. Mater.*, vol. 5, p. 064411, Jun 2021.

[126] J. Hamrle, J. Pištora, B. Hillebrands, B. Lenk, and M. Münzenberg, "Analytical expression of the magneto-optical kerr effect and brillouin light scattering intensity arising from dynamic magnetization," *J. Phys. D*, vol. 43, p. 325004, jul 2010.

[127] J. J. Hauser, "Magnetic proximity effect," *Phys. Rev.*, vol. 187, pp. 580–583, Nov 1969.

[128] R. E. De Wames and T. Wolfram, "Characteristics of magnetostatic surface waves for a metalized ferrite slab," *J. Appl. Phys.*, vol. 41, no. 13, pp. 5243–5246, 1970.

[129] S. Seshadri, "Surface magnetostatic modes of a ferrite slab," *Proc. IEEE*, vol. 58, pp. 506–507, March 1970.

[130] B. Heinrich, C. Burrowes, E. Montoya, B. Kardasz, E. Girt, Y.-Y. Song, Y. Sun, and M. Wu, "Spin pumping at the magnetic insulator (YIG)/normal metal (Au) interfaces," *Phys. Rev. Lett.*, vol. 107, p. 066604, Aug 2011.

[131] S. L. Vysotskii, E. N. Beginin, S. A. Nikitov, E. S. Pavlov, and Y. A. Filimonov, "Effect of ferrite magnonic crystal metallization on bragg resonances of magnetostatic surface waves," *Technical Physics Letters*, vol. 37, no. 11, pp. 1024–1026, 2011.

[132] Y. Sun, H. Chang, M. Kabatek, Y.-Y. Song, Z. Wang, M. Jantz, W. Schneider, M. Wu, E. Montoya, B. Kardasz, B. Heinrich, S. G. E. te Velthuis, H. Schultheiss,

and A. Hoffmann, "Damping in yttrium iron garnet nanoscale films capped by platinum," *Phys. Rev. Lett.*, vol. 111, p. 106601, Sep 2013.

[133] Z. Qiu, K. Ando, K. Uchida, Y. Kajiwara, R. Takahashi, H. Nakayama, T. An, Y. Fujikawa, and E. Saitoh, "Spin mixing conductance at a well-controlled platinum/yttrium iron garnet interface," *Appl. Phys. Lett.*, vol. 103, no. 9, p. 092404, 2013.

[134] M. Mruczkiewicz and M. Krawczyk, "Nonreciprocal dispersion of spin waves in ferromagnetic thin films covered with a finite-conductivity metal," *J. Appl. Phys.*, vol. 115, no. 11, p. 113909, 2014.

[135] N. Kanazawa, T. Goto, and M. Inoue, "Spin wave localization in one-dimensional magnonic microcavity comprising yttrium iron garnet," *J. Appl. Phys.*, vol. 116, no. 8, p. 083903, 2014.

[136] N. Kanazawa, T. Goto, J. W. Hoong, A. Buyandalai, H. Takagi, and M. Inoue, "Metal thickness dependence on spin wave propagation in magnonic crystal using yttrium iron garnet," *J. Appl. Phys.*, vol. 117, no. 17, p. 17E510, 2015.

[137] V. D. Bessonov, M. Mruczkiewicz, R. Gieniusz, U. Guzowska, A. Maziewski, A. I. Stognij, and M. Krawczyk, "Magnonic band gaps in yig-based one-dimensional magnonic crystals: An array of grooves versus an array of metallic stripes," *Phys. Rev. B*, vol. 91, p. 104421, Mar 2015.

[138] N. Kanazawa, T. Goto, K. Sekiguchi, A. B. Granovsky, C. A. Ross, H. Takagi, Y. Nakamura, and M. Inoue, "Demonstration of a robust magnonic spin wave interferometer," *Sci. Rep.*, vol. 6, no. 1, p. 30268, 2016.

[139] K. Shimada, T. Goto, N. Kanazawa, H. Takagi, Y. Nakamura, H. Uchida, and M. Inoue, "Extremely flat transmission band of forward volume spin wave using gold and yttrium iron garnet," *J. Phys. D*, vol. 50, p. 275001, jun 2017.

[140] J. Trossman, J. Lim, W. Bang, J. B. Ketterson, C. C. Tsai, and S. J. Lee, "Effects of an adjacent metal surface on spin wave propagation," *AIP Advances*, vol. 8, no. 5, p. 056024, 2018.

[141] T. Goto, K. Shimada, Y. Nakamura, H. Uchida, and M. Inoue, "One-dimensional magnonic crystal with Cu stripes for forward volume spin waves," *Phys. Rev. Applied*, vol. 11, p. 014033, Jan 2019.

[142] S. A. Bunyaev, R. O. Serha, H. Y. Musiienko-Shmarova, A. J. Kreil, P. Frey, D. A. Bozhko, V. I. Vasyuchka, R. V. Verba, M. Kostylev, B. Hillebrands, G. N. Kakazei, and A. A. Serga, "Spin-wave relaxation by eddy currents in $y_3fe_5o_{12}$/Pt bilayers and a way to suppress it," *Phys. Rev. Applied*, vol. 14, p. 024094, Aug 2020.

[143] G. A. Ovsyannikov, K. Y. Constantinian, K. L. Stankevich, T. A. Shaikhulov, and A. A. Klimov, "Spin current and spin waves at a platinum/yttrium iron garnet interface: impact of microwave power and temperature," *J. Phys. D*, vol. 54, p. 365002, jun 2021.

[144] M. A. Morozova, S. V. Grishin, A. V. Sadovnikov, D. V. Romanenko, Y. P. Sharaevskii, and S. A. Nikitov, "Band gap control in a line-defect magnonic crystal waveguide," *Appl. Phys. Lett.*, vol. 107, no. 24, p. 242402, 2015.

[145] M. Haertinger, C. H. Back, J. Lotze, M. Weiler, S. Geprägs, H. Huebl, S. T. B. Goennenwein, and G. Woltersdorf, "Spin pumping in yig/pt bilayers as a function of layer thickness," *Phys. Rev. B*, vol. 92, p. 054437, Aug 2015.

[146] C. W. Sandweg, Y. Kajiwara, K. Ando, E. Saitoh, and B. Hillebrands, "Enhancement of the spin pumping efficiency by spin wave mode selection," *Appl. Phys. Lett.*, vol. 97, no. 25, p. 252504, 2010.

[147] V. Castel, N. Vlietstra, J. Ben Youssef, and B. J. van Wees, "Platinum thickness dependence of the inverse spin-hall voltage from spin pumping in a hybrid yttrium iron garnet/platinum system," *Appl. Phys. Lett.*, vol. 101, no. 13, p. 132414, 2012.

[148] P. B. Johnson and R. W. Christy, "Optical constants of the noble metals," *Phys. Rev. B*, vol. 6, pp. 4370–4379, Dec 1972.

[149] W. S. M. Werner, K. Glantschnig, and C. Ambrosch-Draxl, "Optical constants and inelastic electron-scattering data for 17 elemental metals," *J. Phys. Chem. Ref.*, vol. 38, no. 4, pp. 1013–1092, 2009.

[150] A. Prabhakar, *Spin Waves Theory and Applications*. Springer-Verlag US, 2009.

[151] R. W. Pohl, *Optik und Atomphysik*. Springer, 1954.

[152] M. Curcic, B. V. Waeyenberge, A. Vansteenkiste, M. Weigand, V. Sackmann, H. Stoll, *et al.*, "Polarization selective magnetic vortex dynamics and core reversal in rotating magnetic fields," *Phys. Rev. Lett.*, vol. 101, p. 197204, nov 2008.

[153] M. Curcic, H. Stoll, M. Weigand, V. Sackmann, P. Juellig, M. Kammerer, *et al.*, "Magnetic vortex core reversal by rotating magnetic fields generated on micrometer length scales," *Phys. Status Solidi(b)*, vol. 248, pp. 2317–2322, jul 2011.

[154] M. Kammerer, M. Weigand, M. Curcic, M. Noske, M. Sproll, A. Vansteenkiste, B. V. Waeyenberge, H. Stoll, G. Woltersdorf, C. H. Back, and G. Schuetz, "Magnetic vortex core reversal by excitation of spin waves," *Nat. Commun.*, vol. 2, apr 2011.

[155] M. Noske, A. Gangwar, H. Stoll, M. Kammerer, M. Sproll, G. Dieterle, M. Weigand, M. Fähnle, G. Woltersdorf, C. H. Back, and G. Schütz, "Unidirectional sub-100-ps magnetic vortex core reversal," *Phys. Rev. B*, vol. 90, p. 104415, sep 2014.

[156] M. Baumgartner, K. Garello, J. Mendil, C. O. Avci, E. Grimaldi, C. Murer, *et al.*, "Spatially and time-resolved magnetization dynamics driven by spin–orbit torques," *Nat. Nanotechnol.*, vol. 12, pp. 980–986, aug 2017.

[157] J. M. Lee, J. H. Kwon, R. Ramaswamy, J. Yoon, J. Son, X. Qiu, R. Mishra, S. Srivastava, K. Cai, and H. Yang, "Oscillatory spin-orbit torque switching induced by field-like torques," *Commun. Phys.*, vol. 1, feb 2018.

[158] G. J. Kwiatkowski, M. H. Badarneh, D. V. Berkov, and P. F. Bessarab, "Optimal control of magnetization reversal in a monodomain particle by means of applied magnetic field," *Phys. Rev. Lett.*, vol. 126, p. 177206, apr 2021.

[159] M. R. Zamani Kouhpanji and B. J. H. Stadler, "A guideline for effectively synthesizing and characterizing magnetic nanoparticles for advancing nanobiotechnology: A review," *Sensors*, vol. 20, no. 9, 2020.

[160] C. Bran, E. Berganza, J. A. Fernandez-Roldan, E. M. Palmero, J. Meier, *et al.*, "Magnetization ratchet in cylindrical nanowires," *ACS Nano*, vol. 12, no. 6, pp. 5932–5939, 2018. PMID: 29812903.

Acknowledgement

I would like to thank my supervisor Prof. Dr. Christian Back for his strong support in the framework of this thesis and for giving me the opportunity to remember what I've learned during my previous apprenticeship.

Moreover, I would like to thank Prof. Dr. Martin Zacharias in his role as the examination chair, as well as Prof. Ph.D. Jonathan Finley as the second examiner of this thesis.

I would like to thank Dr. Takuya Taniguchi for teaching me relevant lab skills as well as for every conversation we've had in the last three years.

Furthermore, I would like to thank Dr. Grace Causer and Franz Vilsmeier for proofreading this thesis as well as for useful hints and fruitful discussions.

Thank you!